

https://dspace.org/

High recovery membrane treatment of mine impacted waters utilizing calcite and gypsum precipitation within a process recycle loop

Franzsen, Sebastian

2019

https://hdl.handle.net/10539/28418

Downloaded from a DSpace repository. https://dspace.org/

HIGH RECOVERY MEMBRANE TREATMENT OF MINE IMPACTED WATERS UTILIZING CALCITE AND GYPSUM PRECIPITATION WITHIN A PROCESS RECYCLE LOOP



UNIVERSITY OF THE
WITWATERSRAND,
JOHANNESBURG

Sebastian Franzsen

A dissertation submitted to the Faculty of Engineering and the Built Environment, University of the Witwatersrand, Johannesburg, in fulfilment of the requirements for the degree of Master of Science in Engineering.

Johannesburg 2019

Declaration

I declare that this dissertation is my own unaided work. It is being submitted for the degree of Master of Science in Engineering to the University of the Witwatersrand, Johannesburg. It has not been submitted before for any degree or examination to any other University.



Sebastian Franzsen

19th day of May 2019

ABSTRACT

Reverse osmosis (RO) and nanofiltration (NF) membrane technologies are extensively applied to the treatment of mine impacted water. However, the volumetric recovery that is attainable by membrane treatment processes is limited by the precipitation of sparingly soluble minerals on the membrane surface and the elevation of osmotic pressure as the volumetric recovery ratio increases. Research studies have shown that intermediate chemical demineralisation (ICD) of primary RO (PRO) concentrate followed by secondary RO (SRO) desalination, (PRO-ICD-SRO), can substantially improve the volumetric recovery of brackish feed waters. The application of secondary NF (SNF) or PRO-ICD-SNF is thought to be particularly attractive in total or near total SNF concentrate recycle processes due to the reduction in osmotic pressure of the recirculation liquor attributed to the higher monovalent salt passage of NF membranes. The transport mechanisms in NF membranes include convection and electro migration in addition to the solution-diffusion mechanism that dominates in RO membranes. Currently, no integrated process simulation solution is available to track the evolution of bulk phase aqueous species in total recycle PRO-ICD-SRO or PRO-ICD-SNF processes as a function of key process parameters such as sludge solids and moisture content, secondary RO or NF rejection characteristics, pH targets, gypsum and calcite precipitation performance and concentrate purge from SRO or SNF concentrate recycle. The aim of this research was to model a total or near total recycle variation of a brackish water PRO-ICD-SNF process in which the bulk liquor total dissolved solids (TDS) would cycle up to a steady state point which is adjustable to the degree of volumetric recovery and sludge waste minimisation sought. The cycling up and subsequent approach to steady state of the recirculation liquor TDS were experimentally observed for the selected PRO-ICD-SNF process. A model of the process was developed in Microsoft's Visual Basic for Applications that utilised the aqueous geochemical modelling capabilities of USGS's PHREEQC. The model showed good agreement between the predicted and experimentally observed aqueous species concentrations and reagent consumptions. A NF submodel based on the Donnan steric pore model with dielectric exclusion (DSPM & DE) was developed to improve the performance prediction of SNF systems SNF systems are sensitive to the evolution of the recirculation liquor chemistry, the hydraulics and membrane properties of SNF system designs and the process configuration and design of

the precipitation reactor systems. A recommendation for future work is to incorporate a rate-based reactor sub model in the ICD-SNF model with the DSPM & DE sub model for the NF. The combination of rigorous ICD and SNF sub models could substantially extend the applicability of the model.

PUBLICATIONS AND PRESENTATIONS

Franzsen, S., R. Bonner, J. Naidu, G. Simate and C. Sheridan. "Estimation of nanofiltration solute rejection in reverse osmosis concentrate treatment processes." ICARD 2018

ACKNOWLEDGEMENTS

I gratefully acknowledge Miwatek for their financial support and project opportunity through which this work was made possible. Further, I gratefully acknowledge Professors Craig Sheridan and Geoffrey Simate for their technical contributions, support and review of this work.

TABLE OF CONTENTS

1 Introduction 1

1.1 Problem statement 3

1.2 Research objectives 3

1.3 Dissertation structure 4

2 Literature review 5

2.1 Rock drainage terminology 5

2.2 Environmental consequence of rock drainage 6

2.3 Health effects of human exposure to rock drainage 8

2.4 Technologies for the treatment of rock drainage 8

2.4.1 Active treatment systems 9

2.4.2 Passive treatment systems 10

2.4.3 In-situ treatment systems 11

2.5 Reverse osmosis and Nanofiltration 11

2.5.1 Spiral would reverse osmosis element 12

2.5.2 Scaling and fouling of membrane elements 13

2.5.3 Concentration polarisation 15

2.5.4 The use of antiscalant to suppress fouling by precipitation 18

2.5.5 Membrane separation theory 19

2.6 PRO concentrate and neutralised ARD 22

2.7 Multistage RO with intermediate chemical demineralisation 23

2.8 Modelling aqueous geochemistry at high ionic strength 25

2.9 PHREEQC version 3 28

2.10 Chemical precipitation 30

2.10.1 Nucleation 30

2.10.2 Crystal growth 31
2.10.3 Calcium sulphate dihydrate (Gypsum) precipitation 33
2.10.4 Calcite precipitation 35
3 Pilot study of ICD-SNF 37
3.1 Experimental setup 38
3.2 Data collection: analytical chemistry and process variables 40
3.3 Experimental results 41
3.4 Membrane Performance 44
3.5 Analytical Results 46
4 Process model development and calibration 50
4.1 Equilibrium process model 50
4.2 Process model calibration and results 55
4.3 Discussion of process model calibration 59
4.4 Conclusion 61
5 Estimation of NF solute rejection in RO concentrate treatment 62
5.1 Abstract 62
5.2 Introduction 63
5.3 Methods 65
5.3.1 Solute mass transfer in the boundary layer 66
5.3.2 Partitioning at feed-membrane and membrane-permeate interfaces 67
5.3.3 Solute mass transfer in the active layer 68
5.3.4 Solution algorithm for NF model 69
5.4 Results and Discussion 72
5.5 Conclusions 83
6 Conclusions and Recommendations 85
6.1 Pilot objective 85

6.2 Process model objective 85
6.3 Improved NF sub model objective 87
7 References 89
8 Appendices 94

List of Tables

Table 2-1 Guideline ionic strength applicability of activity coefficient models 27
Table 3-1 Experimental stages and corresponding process operating parameters 43
Table 3-2 Analytical results at 297 hours into operation..... 47
Table 3-3 Evolution of dissolved aqueous species in SNF feed and permeate 48
Table 3-4 Saturation ratios of solids phases calculated from experimental data..... 49
Table 4-1 Operating parameters for model calibration 56
Table 4-2 Performance parameters for model calibration 57
Table 4-3 Comparison of experimental data and process model results 58
Table 4-4 Comparison of analytical results and model predictions at cycled up conditions 58
Table 5-1 Model input parameters for calibration case 71
Table 5-2 Results of the parameter regression 71
Table 5-3 Results from fitting operational data from RO-NF-CD full scale process and RO-CD-NF-RCY pilot process 73
Table 5-4 Comparison of ion rejections determined by the model and the analytical results from SGS 73
Table 5-5 Cation-anion distributions for the $CaSO_4$ and Na_2SO_4 dominated solutions. 74

Table of Figures

Figure 2-1: Range of pH and mine drainage characteristics. From (Nordstrom, Blowes et al. 2015) 6

Figure 2-2 Fabrication detail of a spiral wound element. From Suez Degrémont handbook (Degrémont SA. 2007) 13

Figure 2-3 SEM-EDS images of $CaCO_3$ formation on a RO membrane. From (Antony, Low et al. 2011) 15

Figure 2-4 SEM-EDS images of $BaSO_4$ scale formation on a RO membrane. From (Antony, Low et al. 2011) 15

Figure 2-5 Schematic of concentration polarisation. From Crittenden et al (Crittenden, Harza et al. 2012) 16

Figure 2-6 Concentration polarisation factors as a function of feed channel velocity and permeate flux. From Crittenden et al (Crittenden, Harza et al. 2012). 19

Figure 2-7 Differential slice of a spiral wound element. From Crittenden et al. (Crittenden, Harza et al. 2012) 21

Figure 2-8 Water quality summary of ARD treatment plant influent and effluent. From MEND Report 3.44.1 (Martin, Loomer et al. 2013) 23

Figure 2-9 The mean activity coefficient of HCl in an HCl-H_2O system and KCl-H_2O system and the mean activity coefficient of KCl in a KCl-H_2O system. From Harvie, et al. (1984) 29

Figure 2-10 Concentration driving forces for crystal growth. From (Coulson, Richardson et al. 1991) 31

Figure 2-11 Typical prisms of gypsum formed between 20 and 60°C. From (Klepetsanis and Koutsoukos 1991) 34

Figure 3-1: Selected ICD-SNF variation for pilot and process model objectives 37

Figure 3-2 Accumulation of dissolved aqueous species, measured using aqueous phase EC, in the recirculation liquor 42

Figure 3-3 Rate of change of recirculation liquor EC vs cycled up recirculation liquor EC 44

Figure 3-5 SEM images of gypsum scaling with celestite inclusions on SNF elements 45

Figure 4-1 Simulation algorithm for process model with PHREEQC COM v3 interface and pitzer.dat 54

Figure 4-2 Pilot scale experimental setup of PRO concentrate feed to ICD-SNF with process model results calibrated at 297 hours in operation 56

Figure 4-3 Sodium and sulphate discharge mass distribution as percentages 60

Figure 5-1: Schematic diagram of the solute concentration profile for each node j 67

Figure 5-2 Simulation algorithm for alternative DSPM & DE NF model 72

Figure 5-3 The effect of pore radius and effective active layer thickness on the Ca, Mg and SO_4 rejection performance of the MDS NF 8040 elements in the RO-NF-CD process 76

Figure 5-4 The effect of pore radius and effective active layer thickness on the HCO_3, Cl and SiO_2 rejection performance of the MDS NF 8040 elements in the RO-NF-CD process 77

Figure 5-5 The effect of membrane pore dielectric constant and feed-membrane Donnan potentials on the Ca, Mg and SO_4 rejection performance of the MDS NF 8040 elements in the RO-NF-CD process 79

Figure 5-6 The effect of membrane pore dielectric constant and feed-membrane Donnan potentials on the Ca, Mg and SO_4 rejection performance of the MDS NF 8040 elements in the RO-NF-CD process 80

Figure 5-7 Comparison of rejection performance of the MDS NF 4040T (RO-CD-NF-RCY process) and MDS NF 8040 (RO-NF-CD process) elements for the Na_2SO_4 and $CaSO_4$ dominated solutions 82

NOMENCLATURE

a	Activity of ionic specie
A	Pure water permeability constant
B	Solute permeability coefficient
C^*	Equilibrium concentration
C	Solute concentration
d_H	Hydraulic diameter
D_L	Diffusion coefficient of solute in water
D_p	Diffusion coefficient in pore
e	Electronic charge; $1.60218.10^{-19}$ C
f_{CF}	Fraction of output liquid phase reporting to membrane waste (cross flow)
f_{SM}	Fraction of output liquid phase reporting to sludge moisture
F	Faraday constant; 96487 C/mol
G	Linear crystal growth rate
I	Ionic strength
J_w	Volumetric flux of water
J_s	Solute flux rate
k_{CP}	Concentration polarisation mass transfer coefficient
k_B	Boltzmann constant; $1.38066.10^{-23}$ J/K
k_d	Diffusion mass transfer coefficient
k_r	Growth rate parameter
k_s	Solute mass transfer coefficient
k_w	Water mass transfer coefficient
K	Equilibrium constant based on species activity; dimensionless
K_c	Equilibrium constant (concentration); hindrance factor for convection
K_d	Hindrance factor for diffusion
K_j	Parameter for relation of TDS to EC in stream j
L	Water mass flow rate of output stream or crystal size
m	Mass of solids phase
M_i	Molecular weight of aqueous specie i
M_k	Molecular weight of solids phase k
M_r	Molecular weight of reagent r
M_s	Moles of solute transferred or molar mass of solids phase
N_r	Molar flow rate of reagent r
nC	Number of aqueous species components or number of controllers
nF_0	Number of feed streams
nP	Number of equilibrium phase solids
nR	Number of reagents
P	Pressure
PV_j	Process variable (Current value) j corresponding to SP_j

Q	Volumetric flowrate
r	Rejection of aqueous specie
r_p	Pore radius
r_s	Stokes radius
R	Volumetric recovery of membrane process
Re	Reynolds number
R_g	Gas constant; 8.314 J/(mol.K)
T	Temperature of bulk liquid
Sc	Schmidt number
S	Molar flow rate of solids
SI	Saturation index
SP_j	Setpoint of parameter j in solver
w	Effective width of the feed channel
X	Precipitation extent
Z	Number of replaceable hydrogen atoms

Indices

0	Feed stream
b	Bulk liquid
F	Feed
FC	Feed channel
i	Aqueous specie index or order of integration
j	Stream index, controller index or node on element length axis
k	Solid equilibrium phase index or iteration number
m	Membrane
p	Permeate
r	Reagent index
s	Solids phase
z	Discrete interval on length axis of membrane element or valence
t	Time

Symbols

ΔW_i	Born solvation energy barrier
$\Delta\varphi_D$	Donnan Potential
β	Dimensionless concentration polarisation factor
γ	Activity coefficient
ε	Error function
ε_0	Permittivity of free space; $8.85419.10^{-12}$ $C^2/(J.m)$
ε_b	Bulk dielectric constant
ε_p	Membrane pore dielectric constant
θ	Steric partitioning coefficient
κ	Electrical conductivity or factor for hydraulic impact of feed spacers
λ	Ratio of ion stokes radius to membrane pore radius
μ	Feed water dynamic viscosity
π	Osmotic pressure
ρ	Liquid phase density
ρ_c	Density of solids phase
υ	Velocity in the feed channel
ϕ_s	Surface shape factor
ϕ_v	Volume shape factor
ψ	Number crystal size distribution
$\varnothing$	Ratio of water flux and solute mass transfer coefficient
$\in$	Correction factor for suction effect due to higher permeation rates in NF

ACRONYMS

ALD	Anoxic limestone drain
ARD	Acid rock drainage
AMD	Acid mine drainage
APS	Accelerated precipitation softening
CD	Chemical demineralisation
CESP	Chemically enhanced seeded precipitation
COM	Component object model
DE	Dielectric exclusion
DSPM	Donnan steric pore model
EC	Electrical conductivity
EDS	Energy dispersive X-ray spectroscopy
ENP	Extended Nernst Planc
GARD	Global acid rock drainage
IAP	Ion activity product
ICD	Intermediate chemical demineralisation
ICP	Intermediate chemical precipitation
K_{sp}	Solubility product constant
MBT	Miwatek Brine Treatment
MET	Miwatek Ettringite Treatment
MIW	Mine impacted water
MET	Miwatek Ettringite Treatment
MS	Microsoft
NARD	Natural acid rock drainage
NF	Nanofiltration
NMD	Neutral mine drainage
NRTL	Non-random two liquid
PV	Process variable
RCY	Recycle
RO	Reverse Osmosis
PCD	Primary chemical demineralisation
PRO	Primary Reverse Osmosis

SD	Saline drainage
SEM	Scanning electron microscopy
SIT	Specific ion interaction
SNF	Secondary Nanofiltration
SRO	Secondary Reverse Osmosis
SR	Saturation ratio
SUF	Secondary ultrafiltration
TDS	Total dissolved solids
UF	Ultrafiltration
UNIFAC	UNIQUAC Functional-group activity coefficients
UNIQUAC	Universal quasichemical
USGS	United States Geological Survey
VBA	Visual Basic for Applications
WHO	World Health Organization
ZLD	Zero liquid discharge

1 INTRODUCTION

Reverse osmosis (RO) and nanofiltration (NF) account for 55% of the total worldwide water produced from desalination activities and 87% of water reclaimed from brackish water resources (Antony, Low et al. 2011). Both RO and NF processes separate the feed water into permeate and concentrate which vary in flow rate and quality depending on the volumetric recovery, water quality and design criteria of the process (Antony, Low et al. 2011, Randall and Nathoo 2015). The permeate stream is typically suitable for human consumption or environmental discharge after disinfection, conditioning and in some cases secondary treatment. However, the flow rate and composition of concentrate is particularly critical to inland applications where disposal into the ocean is impractical (Rahardianto, McCool et al. 2010, Subramani and Jacangelo 2014).

The composition of a membrane concentrate originating from a brackish water source, e.g., mine impacted water, is like that of the effluent of a typical lime neutralisation process in the treatment of acid rock drainage (ARD) – concentrations of constituents associated with sparingly soluble minerals of hydroxides, oxyhydroxides and oxygenates are low and primary scale forming species such as calcite and gypsum are constrained by antiscalant performance or approach to chemical equilibrium respectively.

Concentrate disposal (or neutralised ARD effluent) options include surface water discharge, deep well injection, land application, and evaporation in ponds or thermal processes with subsequent solids disposal. However, concentrate disposal using the stated options is very costly. Previous studies have shown that the minimisation of concentrate results in lower disposal costs and is thus the driver in the development of zero liquid discharge (ZLD) or near ZLD (95 – 98% feed water recovery) processes (Subramani and Jacangelo 2014, Randall and Nathoo 2015).

However, the fouling of membrane elements through the precipitation of sparingly soluble minerals is a major challenge in achieving a high volumetric recovery and thus limits the degree of concentrate minimisation. This is because scale-forming precursors, of which the dominant ions include Ca^{2+}, SO_4^{2-} and CO_3^{2-}, are concentrated above the solubility limit of sparingly soluble minerals such as calcium sulphate, calcium carbonate and barium sulphate (Gabelich, Williams et al. 2007). For example, calcite, the most

stable polymorph of calcium carbonate at typical operating conditions, is an alkaline scale that is readily controlled, predicted and removed from membrane surfaces. Conversely, gypsum or calcium sulphate dihydrate which is the crystallographic form of calcium sulphate present at ambient conditions is difficult to remove from membrane surfaces, and its saturation ratio (SR) is typically the limiting constraint in volumetric recovery (Antony, Low et al. 2011).

Research and operational studies have shown that dosing the feedwater with scale inhibitors suppress the formation of scale and allows membrane systems to be operated above the saturation concentration of scale forming species. Generally accepted SRs – defined as $SR_x = IAP_x/K_{sp,x}$, (where IAP = ion activity product Ksp = solubility product constant) (Parkhurst and Apello 1999) – limits are 135 – 150 for calcite and 2.5 – 4.0 for gypsum (Ferguson, Ferguson et al. 2011). Although scale inhibitors are used to suppress scale formation and improve volumetric recovery, they substantially increase the operating costs, contribute to fouling if used in excessive doses and fall short of near ZLD performance in the absence of secondary membrane stages with pre-treatment (Rahardianto, Gao et al. 2007).

Research studies have also shown that intermediate chemical demineralisation (ICD) of primary RO (PRO) concentrate followed by secondary RO (SRO) desalination, (PRO-ICD-SRO), can substantially improve the volumetric recovery of brackish feed waters (Gabelich, Williams et al. 2007, Rahardianto, Gao et al. 2007). For example, the ICD treatment aimed at reducing $CaSO_4$ scaling propensity through the precipitation of $CaCO_3$ has been successfully demonstrated by several laboratory and pilot scale studies (Rahardianto, McCool et al. 2010, McCool, Rahardianto et al. 2013).

One variation of ICD is chemically enhanced seeded precipitation (CESP) in which lime induced $CaCO_3$ precipitation precedes a seeded $CaSO_4$ precipitation step and partial concentrate recycle from the SRO desalination unit (PRO-CESP-SRO) (Rahardianto, McCool et al. 2010, McCool, Rahardianto et al. 2013). In PRO-CESP-SRO, the $CaCO_3$ precipitation step is shown to reduce the residual antiscalants concentration and, consequently, reduce gypsum seed poisoning. The CESP demineralisation of PRO concentrate reduced the gypsum SR from 1.7 to 1.1 which was shown to be adequate for SRO desalination (McCool, Rahardianto et al. 2013). Others further investigated process

alternatives for antiscalant disruption with subsequent enhanced ICD leading to improved SRO recovery (Greenlee, Testa et al. 2011).

Of particular importance for PRO-ICD-SRO processes, in which brackish feed waters are concentrated to high ionic strength with a uniquely low concentration of monovalent anions attributed to the rejection characteristics of commercially available NF membrane elements, is the Pitzer model (Harvie, Møller et al. 1984). The Pitzer model can accurately predict thermodynamic properties at high ionic strength for solutions with compositions substantially different from that of seawater. It has been shown that activity coefficients calculated by the Pitzer model (pitzer.dat) supplied with PHREEQC provide an accurate match to measured data with higher ionic strength solutions (Appelo 2015). Moreover, the complete geochemical simulation capabilities of PHREEQC are accessible to a number of software environments through the IPHREEQC modules released by the United States Geological Survey (USGS) (Charlton and Parkhurst 2011).

In this study, the PHREEQC capabilities were accessed from Microsoft's Visual Basic for Applications (VBA) through the component object model (COM) interface for the *process model objective* and similarly through Python for the *improved NF sub-model objective.*

1.1 Problem statement

ICD-SNF processes show promise in the high recovery treatment of brackish water PRO concentrates or neutralised ARD effluent, and PHREEQC with the pitzer.dat database can accurately predict the thermodynamic properties of high ionic strength streams. However, no integrated process simulation solution is available to predict the steady state concentration of bulk phase aqueous species in a total recycle ICD-SNF process as a function of key process parameters such as sludge solids and moisture content, secondary RO rejection characteristics, pH targets, gypsum and calcite precipitation performance and concentrate purge from SRO concentrate recycle.

1.2 Research objectives

The aim of this research was to model a total or near total recycle variation of ICD-SNF in which the bulk liquor total dissolved solids (TDS) would cycle up to a steady state,

high ionic strength point – the Miwatek Brine Treatment (MBT) process. The industrial importance of the research centres on non-thermal waste minimisation of PRO concentrate or neutralised ARD effluent. The selected ICD-SNF variation can be applied to both the treatment of neutralised ARD and PRO concentrate from brackish or neutral mine drainage (NMD) waters.

Three specific objectives were identified to address the problem statement, namely (1) the pilot objective, (2) the process model objective and (3) the improved NF sub model objective:

1. The first objective was to pilot the ICD-SNF variation on PRO concentrate – the *pilot objective*;
2. The second objective was to develop a process model to predict the cycled-up TDS of the recirculation liquor as a function of input and output masses – the *process model objective*;
3. The third objective was to improve the NF sub model by incorporating physical transport processes associated with NF membrane systems at high ionic strength – the *improved NF sub model objective*;

1.3 Dissertation structure

The dissertation comprises six chapters. Chapter 1 is the introduction that provides the background that leads into the problem statement and the research objectives. Chapter 2 is the literature survey that supports the problem statement, *process model objective* and *pilot objective*. The literature survey that support the *improved NF sub model objective* is found in Chapter 5. The indulgence of the reader is requested as the dissertation comprises a combination of conventional chapters and a publication. Chapter 3 describes the materials and methods of the pilot operation and presents the experimental results, analytical data and observations. Chapter 4 describes the development of the process model, the solver algorithm that interfaces with the PHREEQC COM module and the calibration of the process model using the data from Chapter 3. Chapter 5 is a journal article that presents the development and results of the DSPM & DE based high ionic strength NF sub model. The dissertation concludes in Chapter 6 with a summary of the findings and recommendations.

2 LITERATURE REVIEW

2.1 Rock drainage terminology

The term acid rock drainage (ARD) is widely used for acid drainage produced from rock, whether it be from mining activities or not. Examples of ARD includes natural acid rock drainage (NARD), acid mine drainage (AMD), acid drainage from construction and excavation activities where sulfide-rich rock is present(Nordstrom, Blowes et al. 2015).

The Global Acid Rock Drainage Guide (GARD Guide) addresses specifically ARD, neutral mine drainage (NMD) and saline drainage (SD) into which contaminants are released from solid to liquid phase transfer by the oxidation of sulfide bearing minerals. The discrete characterisation of the water quality resulting from ARD, NMD or SD is not appropriate due to the simultaneous occurrence of aqueous properties and conditions. The use of the term acid mine drainage (AMD) as a general descriptor is discouraged as it implies that acid drainage originates solely from mining activities. Acid mine drainage as a descriptive term is considered too narrow as acid drainage can be the result of a variety of natural sources and anthropogenic activities (INAP 2009).

The characteristics of ARD includes an acidic pH with sulphate being the dominant ion. Most ARD samples fall below pH 6 with samples below an indicative pH of 2 is as a result of concentration by evaporation. The characteristics of NMD includes an indicative pH range between 6 and 9 and contains dissolved constituents that originates from sulphide oxidation, primarily sulphate. Neutral mine drainage occurs where the acid consumption related to carbonic content is sufficient to maintain a neutral pH condition. NMD can also occur during early stages of the weathering of mine wastes that have an acid generating capacity in excess of the carbonate based neutralisation capacity. In these conditions, NMD will continue until the rate of acid generation exceeds the rate of acid consumption. The use of the SD term and reference to salinity is applied in rock drainage as a general reference to the amount of dissolved constituents. The classification of water by salinity has (1) freshwater at < 1000 mg/l, (2) Brackish water at 1000 – 10000 mg/l, (3) Saline water at 10000 – 35000 mg/l and (4) Brine at > 35000 mg/l. Mine water with pH values in excess of 9 has been found, although uncommon, and is referred to a basic

mine drainage (Nordstrom, Blowes et al. 2015). The pH range and mine drainage characteristics are summarised in Figure 2-1.

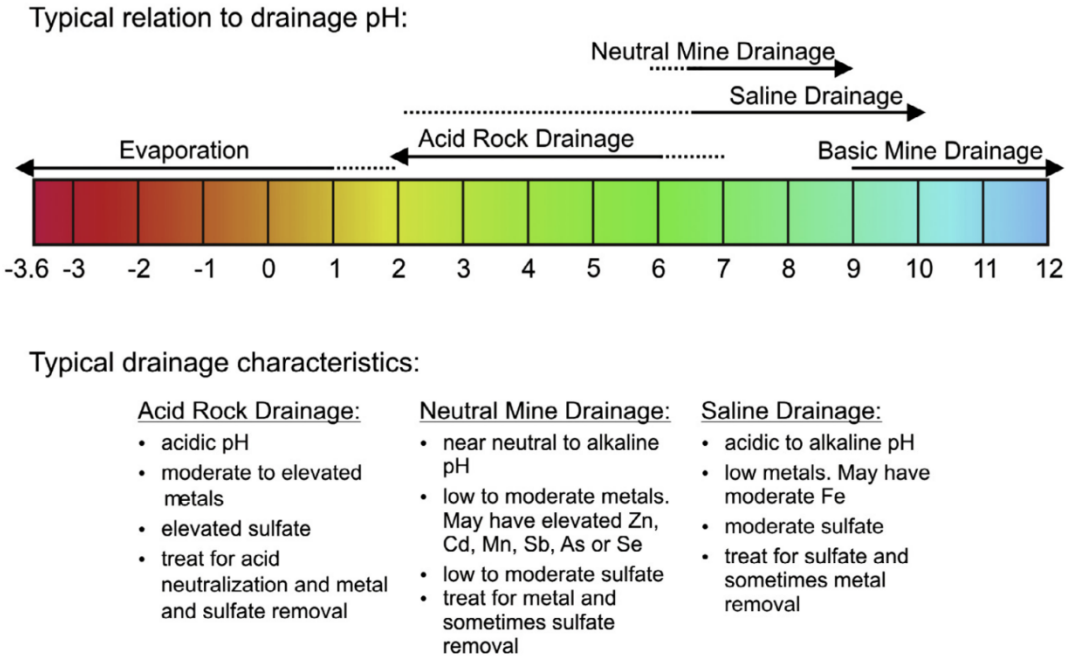

Figure 2-1: Range of pH and mine drainage characteristics. From (Nordstrom, Blowes et al. 2015)

2.2 Environmental consequence of rock drainage

Nordstrom reviewed the research done by the United States Geological Survey (USGS) on the mobilisation of trace elements from mineralised areas into surface waters. The mobility of contaminants from mining impacted areas depends on (1) what mineral sources are present, (2) whether the minerals are present in sufficient quantities, (3) the rates of dissolution, precipitation and sorption relative to water transport and (4) the hydrology that defines the main flow paths. Nordstrom states that generation of rock drainage and its subsequent mixing with surface waters depends on petrology and mineralogy, structural geology, geomorphology, surface water hydrology, hydrogeology, climatology, microbiology, chemistry and the mining and mineral processing history. Remediation or treatment targets should thus be in line with the natural background

conditions rather than a water quality standard that may not take into account a highly mineralised background condition.

The sorption and precipitation behaviour of constituents originating from rock drainage depends on the chemical behaviour, aqueous speciation and pH, temperature and contact time with mineral surfaces (Nordstrom 2011). Examples of such behaviour includes

i. Low metal precipitation occurs at pH < 3.5 and metal ratios indicative of the main minerals group are maintained;
ii. Exceptions to (i) includes Fe, SiO_2 and redox sensitive oxyanions of As, Sb, Se, Mo, Cr and V;
iii. Once dissolved, metal and metalloid concentrations are strongly affected by redox conditions and pH;
iv. Iron is rapidly oxidised by bacteria and archaea and Fe(III) hydrolyses and precipitates within a low pH range of 1-3;
v. Some insoluble sulphate minerals precipitate, e.g. anglesite, barite, jarosite, alunite and basaluminite. Sulphate behaves conservatively as the magnitude of sulphate reduction attributed to precipitation is insignificant; and
vi. Aluminium hydrolyses near a pH of 5 and removal by precipitation is expected in the pH range 4-5.5.

The USGS research identifies the rates of pyrite weathering from 5.5 mmol/h for unmined pyritised rock undergoing natural weathering to 17100 mol/h for extreme portal discharge of massive sulphide mineral deposits. The formation of colloids and organic complexes contribute to the operational definition of dissolved species and is of particular concern for Fe as its geochemistry includes numerous colloids that passes through sampling filters. Similarly, Al behaves better in the pH range of 4-5.5 however at pH greater than 7.5, the occurrence of Al complexed with organic carbon complicates the geochemical interpretation (Nordstrom 2011).

In South Africa, there are over 8000 derelict and ownerless mines. The acid rock drainage from these mines has led to health impacts on humans, disruption of societies and destruction of biodiversity. The cost of these impacts added to the rehabilitation of water bodies is incalculable (Durand 2012).

The urbanisation of the Witwatersrand has resulted in people living and working amongst slimes dams, rock dumps and ARD polluted water. These people are exposed to the pollutants through inhalation, ingestion and skin contact. People from the informal settlement at Tudor Shaft were relocated only after National Nuclear Regulator confirmed that the wetland on which the shacks were built was radioactive. Over 270 slimes dams in the Witwatersrand and Far West Rand areas occupy approximately 400 km^2 and will continue to pollute the environment as long as they take to erode away (Durand 2012).

2.3 Health effects of human exposure to rock drainage

The beneficiation of ore deposits in which mineral commodities are concentrated, generates waste streams that includes rock piles, tailings, smelter slag, particulate emissions, spent processing liquors and mine impacted waters. Plumlee and Morman (2011) summarised the mineralogical and geochemical characteristics of mine wastes and the links to potential adverse health effects through occupational and environmental exposures. Knowledge on the toxicity and the mineralogical and geochemical controls on toxicity, are available for mercury, arsenic and in particular lead. Similar linkages for the other metals that are found in mine wastes (e.g. cadmium, nickel, cobalt and manganese) are less studied. The summary concludes from the poor understanding of the integrated effects of multiple metals, minerals and or radionuclide toxicants, a need for inter-disciplinary collaboration between health and earth scientists. Such collaboration is sought to address the nature of exposure to mine wastes, the behaviour of mine waste particles in the body and the mine waste characteristics of toxicological concern (Plumlee and Morman 2011).

2.4 Technologies for the treatment of rock drainage

The philosophy that prevention is better than cure could be extended to prevention of mine drainage is preferable to the treatment of mine drainage. The techniques that are available to prevent or minimise the generation of mine drainage and subsequent migration is not always practical however. Source control techniques includes flooding and sealing of underground mines, underwater storage of mine tailings, land based storage in sealed waste heaps, blending of mineral wastes, total solidification of tailings, application of anionic surfactants and microencapsulation (Johnson and Hallberg 2005).

The reasons for the treatment of mine drainage may include (INAP 2009)

i. Recovery and reuse of water within the water reticulation system of a mining operation;
ii. Protection of human health where direct or indirect exposure is possible;
iii. Environmental protection of surface and ground water resources through the removal of pollutants;
iv. Recovery of potential commercial products however it is unlikely that this would be the only driver for the installation of a treatment facility;
v. Compliance with regulatory requirements for the discharge of mine water to a public stream or aquifer;
vi. Recovery of water to a quality suitable for use by neighbouring communities and industry, especially in water stressed areas where mine drainage can be seen as a resource; and
vii. Sustainable mining requires the minimisation of impacts on the environment during life of mine and post closure.

The treatment options for rock drainage can be broadly categorised into active, passive and in-situ treatment options.

2.4.1 Active treatment systems

Active treatment systems, as the term implies, requires active control and management and is thus more applicable during the exploration and operational phases of mining activities. Closure and post closure applications are typically associated with large volumetric flows. The disposal of liquid and solid waste is required and constitutes a major fraction of the operational cost. The operational and maintenance costs as well as the capital investment are expected to be considerably more than for passive and in-situ treatment. Active treatment can be applied to all flowrates and any aqueous constituent can be treated (INAP 2009).

The preeminent example of active treatment is the addition of chemical neutralisation agents such as limestone, un-hydrated lime (quicklime, unslaked lime), slaked lime

(hydrated lime), caustic, sodium carbonate and magnesium oxide or hydroxide. The intent of neutralisation and high pH reaction systems is to increase the rate of oxidation of, in particular, ferrous iron and to effect the precipitation of numerous metals as hydroxide and carbonate solids phases. The use of staged pH steps within the operating pH range and the use of specific coagulants to exploit surface complexation allows for the removal of selected components, e.g. arsenic and molybdenum (Johnson and Hallberg 2005).

2.4.2 Passive treatment systems

Passive treatment systems are especially attractive for the closure and post closure phases of mining activities. The use of natural energy sources (gravity flow, solar energy and bio-chemical energy) is attributed to the interest in passive treatment systems. In addition, the operational involvement is limited, the capital investment is significantly lower than for active treatment systems and the operating cost is very low. Passive treatment systems are however subject to limits of applicability as lower flow rates with lower acidity and metals content can be treated. The treated water quality is highly variable and poorer than for active treatment systems. The accumulated pollutants in wetland sludge represents a long term liability (INAP 2009). The absence of a brine stream should not be confused with no liquid waste in the case where the treated water does not comply with the relevant water quality specification. Abiotic and biological passive treatment technologies are available. An example of the former is anoxic limestone drains and of the latter aerobic wetlands, anaerobic wetlands or compost reactors, permeable reactive barriers and packed bed iron oxidation bioreactors (Johnson and Hallberg 2005).

Anoxic limestone drains (ALDs) are considered a passive treatment technology and is generally coupled with one or more other passive treatment technologies, e.g. aerobic and anaerobic wetlands. An ALD is a lined cavity that is packed with limestone gravel and is impervious to air or ground water ingress. The process intent is to maintain iron in its reduced form so as to avoid the precipitation of ferric hydroxide and subsequent armouring of the limestone particles. The application of ALDs to mine waters with high ferric iron and aluminium content results in relatively short term (within 6 months) failures due to the iron and aluminium based armouring that occurs. If aerated mine waters are to be treated, passage through an anoxic pond is necessary to reduce the dissolved oxygen content (Johnson and Hallberg 2005). Dolomite is a cost effective alternative to

limestone in the application of ALDs to high sulphate and low pH ARD as the formation of gypsum armour on limestone particles can occur. Huminicki et al. showed that uncoated dolomite reacts faster than gypsum coated calcite after one month of gypsum growth (Huminicki and Rimstidt 2008).

2.4.3 In-situ treatment systems

In-situ treatment systems requires active and ongoing operational support and, as for active treatment systems, are thus more applicable to the exploration and operational phases of mining activities. The capital investment is expected to be the lower than that of active and passive systems. The operational cost may be high due to the process inefficiencies related to the mixing and utilisation of reagents. The sludge that is produced in-situ may represent a long term liability similar to the sludge that accumulates in wetlands. The quality of the treated water is expected to be variable, however in-situ treatment systems can be applied to a large volumetric flow range for predominantly the treatment of acidity and metals removal (INAP 2009).

2.5 Reverse osmosis and Nanofiltration

Reverse osmosis (RO) and nanofiltration (NF) account for 55% of the total worldwide water produced from desalination activities and 87% of water reclaimed from brackish water resources (Antony, Low et al. 2011). Both RO and NF processes separate the feed water into permeate and concentrate which vary in flow rate and quality depending on the volumetric recovery of the process (Antony, Low et al. 2011, Randall and Nathoo 2015). The permeate stream is typically suitable for human consumption or environmental discharge after disinfection, conditioning and in some cases secondary treatment. However, the flow rate and composition of concentrate is particularly critical to inland applications where disposal into the ocean is impractical (Rahardianto, McCool et al. 2010, Subramani and Jacangelo 2014).

Concentrate disposal options include surface water discharge, deep well injection, land application, and evaporation in ponds or thermal processes with subsequent solids disposal. However, concentrate disposal using the stated options is very costly. The minimisation of concentrate results in lower disposal costs and is thus the driver in the

development of zero liquid discharge (ZLD) or near ZLD (95 – 98% feed water recovery) processes (Subramani and Jacangelo 2014, Randall and Nathoo 2015).

2.5.1 Spiral would reverse osmosis element

RO membrane elements are of either the spiral wound or the hollow fine fibre configuration. Spiral wound elements are briefly introduced here as they were used in the pilot study.

Figure 2-2 illustrates the following description of the fabrication detail of a spiral wound element. Two sheets of membrane material on either side of a permeate collector forms an envelope with the weld along three sides of the membranes. The active layer of the membrane material faces outwards and the permeate collector transports the permeate to the perforated central tube where the open side of the envelope is attached. Multiple envelops are separated with a feed spacer which establishes the feed-concentrate channel through which the feed enters and a concentrate exits. The envelopes are rolled around the perforated central tube to form a spiral wound RO element. (Crittenden, Harza et al. 2012)

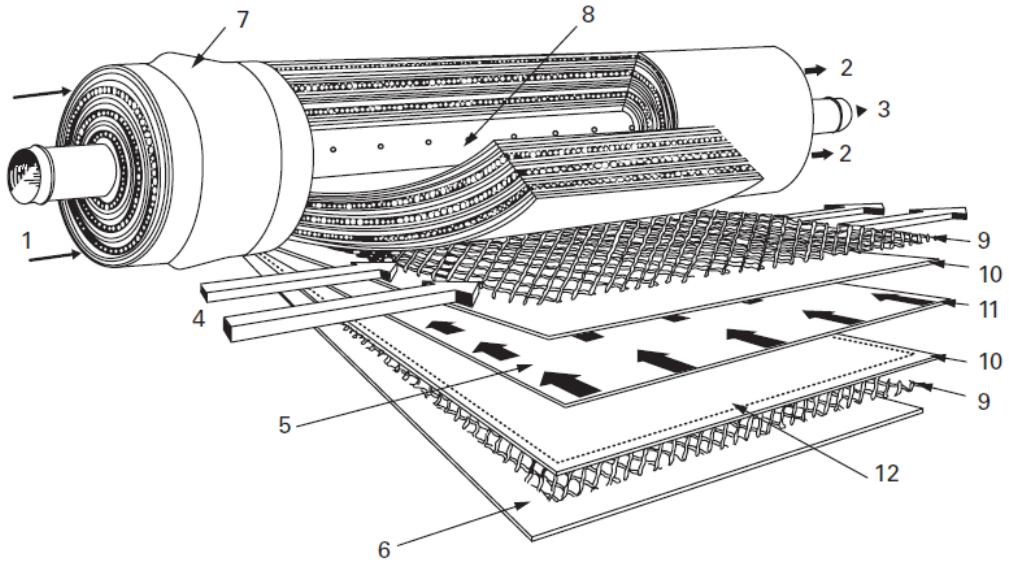

Figure 2-2 Fabrication detail of a spiral wound element. From Suez Degrémont handbook (Degrémont SA. 2007)

2.5.2 Scaling and fouling of membrane elements

The fouling of membrane elements through the precipitation of sparingly soluble minerals is a major challenge in achieving a high volumetric recovery and thus limits the degree of concentrate minimisation. This is because scale-forming precursors, of which the dominant ions include Ca^{2+}, SO_4^{2-} and CO_3^{2-}, are concentrated above the solubility limit of sparingly soluble minerals such as calcium sulphate, calcium carbonate and barium sulphate (Gabelich, Williams et al. 2007).

The nucleation and crystal growth kinetics and not just the aforementioned supersaturation of the sparingly soluble minerals should be considered. Scale formation in membrane systems follows two crystallisation pathways, namely surface crystallisation and bulk crystallisation. Surface crystallisation occurs as the scale deposit grows laterally on the membrane surface thereby causing flux decline and membrane blockage. Bulk crystallisation occurs from the homogenous nucleation and growth in the bulk liquid

phase from where it fouls the membrane through deposition. In Figure 2-3 and Figure 2-4, the SEM-EDS images of $CaCO_3$ and $BaSO_4$ detection on membrane surfaces are illustrated respectively (Antony, Low et al. 2011).

Uchymiak et al. developed an experimental setup to directly observe crystal growth on a RO membrane in real time with an optical microscope. The digitised images were analysed to determine the time evolution of (1) the membrane surface area that is scaled, (2) the surface number density (SND) of gypsum crystals and (3) the size of the gypsum crystals. The rate of formation of gypsum surface crystals increased the most for higher gypsum saturation indices. The upper limit of crystal surface density was also higher for higher saturation indices. The nucleation rate decreased with increasing surface coverage and the dominant growth mechanism shifted from nucleation to diffusion controlled growth of existing crystals. It was observed that the crystallisation induction time decreased with increasing gypsum saturation index and that more favourable surface nucleation sites were populated first, leading to increased time of appearance for newer crystals. The study suggested that the growth rate of surface crystals can be reasonably characterised by a diffusion growth model based on a crystal fluid mass transfer coefficient calculated from a crystal Sherwood number correlation (Uchymiak, Lyster et al. 2008).

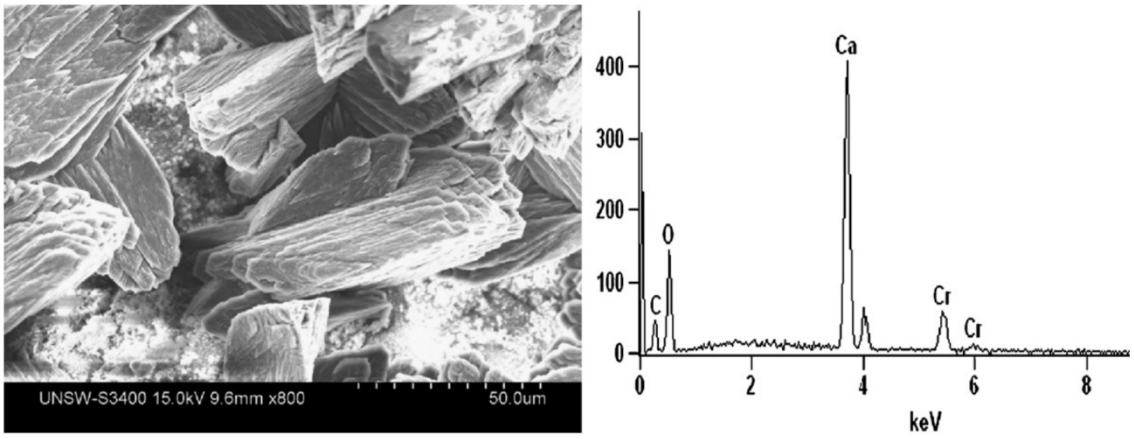

Figure 2-4 SEM-EDS images of $CaCO_3$ formation on a RO membrane. From (Antony, Low et al. 2011)

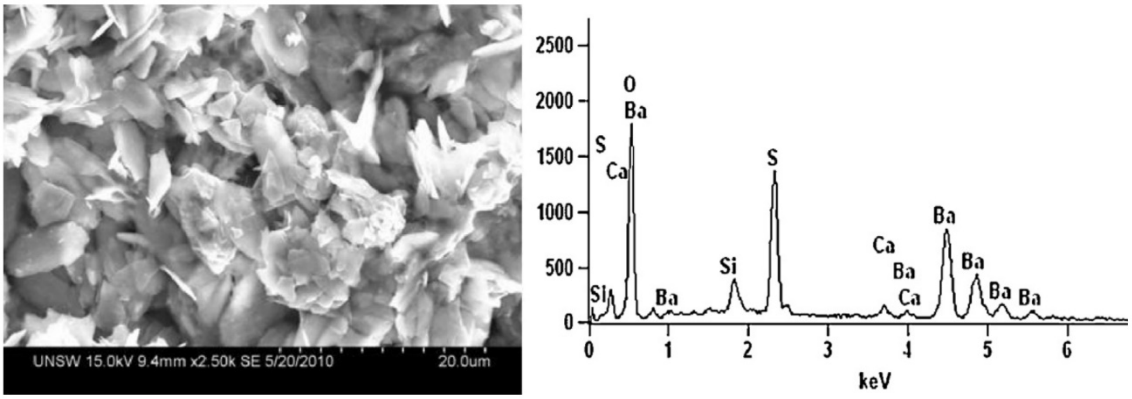

Figure 2-3 SEM-EDS images of $BaSO_4$ scale formation on a RO membrane. From (Antony, Low et al. 2011)

2.5.3 Concentration polarisation

Concentration polarisation refers to the higher concentration of solutes at the membrane surface as compared to the solute concentration in the bulk liquid in the feed channel. The rejection characteristics for solvents and solutes are different and thus a boundary layer of higher concentrations is formed at the membrane surface. Concentration polarisation is a negative phenomenon due to the following impacts on membrane separation (Crittenden, Harza et al. 2012)

i. Higher osmotic pressure gradient due to higher concentration of solutes at the membrane surface leads to lower water flux

ii. Higher concentration gradient leads to higher solute transport across the membrane, combined with lower water flux leads to lower solute rejection
iii. Higher solutes concentration leads to higher saturation ratios and thus the potential for nucleation and growth of scale forming species

The mechanism of concentration polarisation is depicted in Figure 2-5. The bulk liquor transport is parallel to the membrane whilst the water and solute flux through the membrane is illustrated as a one-dimensional transfer perpendicular to the membrane. Initially, the concentration of solutes accumulates at the membrane surface which then subsequently reaches a steady state concentration that is higher than the bulk liquid solute concentration. At the steady state, the flux of solute towards the membrane is balance by flux of solute towards the bulk liquor and through the membrane. Integrating the mass balance equation across the thickness of the boundary layer with boundary conditions for (1) solute concentration at the membrane and (2) at the bulk liquor, yields Equation (2-1) (Crittenden, Harza et al. 2012).

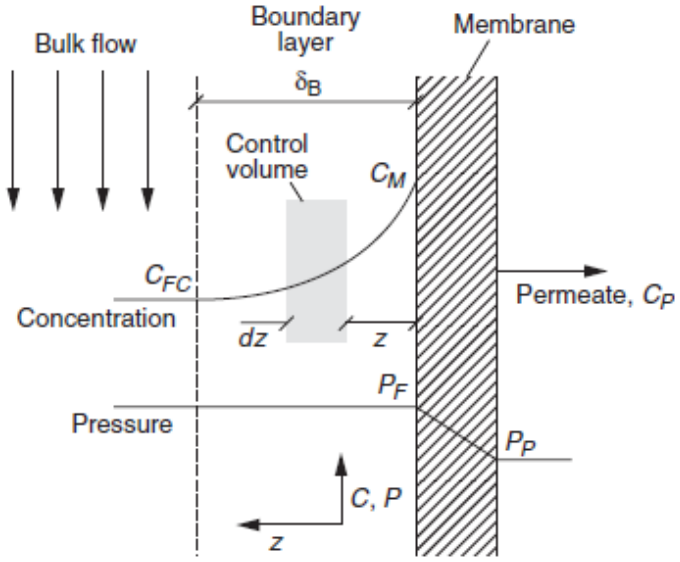

Figure 2-5 Schematic of concentration polarisation. From Crittenden et al (Crittenden, Harza et al. 2012).

$$\frac{C_M - C_P}{C_{FC} - C_P} = e^{Jw/K_{CP}} \quad (2\text{-}1)$$

where

k_{CP}	=	concentration polarisation mass transfer coefficient [m.s^{-1}]
C_M	=	solute concentration at membrane surface [mole.L^{-1}]
C_P	=	solute concentration in permeate [mole.L^{-1}]
C_{FC}	=	solute concentration in feed channel [mole.L^{-1}]
J_W	=	volumetric flux of water [L.m^{-2}.h^{-1}]

The Gilliland correlation, Equation (2-2), for turbulent flow in pipes can be used to calculate the concentration polarisation mass transfer coefficient k_{CP}. It is a mass transfer correlation of the typical form $Sh = \alpha_1(Re)^{\alpha_2}(Sc)^{\alpha_3}$ where *Sh*, *Re* and *Sc* are the dimensionless Sherwood, Reynolds and Schmidt numbers respectively. The Gilliland correlation and the definition of the dimensionless numbers are given by Equations (2-2), (2-3) and (2-4) (Crittenden, Harza et al. 2012).

$$k_{CP} = 0.023\frac{D_L}{d_H}(Re)^{0.83}(Sc)^{0.33} \quad (2\text{-}2)$$

$$Re = \frac{\rho v d_H}{D_L} \quad (2\text{-}3)$$

$$Sc = \frac{\mu}{\rho D_L} \quad (2\text{-}4)$$

where

D_L	=	Diffusion coefficient of solute in water [m^2.s^{-1}]
v	=	velocity in feed channel [m.s^{-1}]
ρ	=	feed water density [kg.m^{-3}]
μ	=	feed water dynamic viscosity [kg.m^{-1}.s^{-1}]
d_H	=	hydraulic diameter [m]

The dimensionless concentration polarisation factor is defined as the ratio of the solute concentration at the membrane and in the feed-concentrate channel – Equation (2-5). Figure 2-6 illustrates the concentration polarisation factor as a function of feed channel velocity and permeate flux

$$\beta = \frac{C_M}{C_{FC}} \tag{2-5}$$

Where

β = dimensionless concentration polarisation factor

Combining Equation (2-1) with Equation (2-5) yields Equation (2-6) for β which is independent of concentration and related to the rejection *r* (Crittenden, Harza et al. 2012). In Equation (2-6), the rejection r refers to the rejection of total dissolved solutes (TDS). It can be generalised to the rejection of solute specie r_i.

$$\frac{\beta - (1 - r)}{r} = e^{Jw/K_{CP}} \tag{2-6}$$

2.5.4 The use of antiscalant to suppress fouling by precipitation

Research and operational studies have shown that dosing of scale inhibitors suppress the formation of scales and allow membrane systems to be operated above the saturation concentration of scale forming species. Generally accepted SRs – defined as $SR_x = IAP_x/K_{sp,x}$, (where IAP = ion activity product Ksp = solubility product constant) (Parkhurst and Apello 1999) – limits are 135 – 150 for calcite, 60 for barite and 2.5 – 4.0 for gypsum (Ferguson, Ferguson et al. 2011, Subramani and Jacangelo 2014).

Although scale inhibitors are used to suppress scale formation and improve volumetric recovery, they substantially increase the operating costs, contribute to fouling if used in excessive doses and fall short of near ZLD performance in the absence of secondary membrane stages with pre-treatment (Rahardianto, Gao et al. 2007).

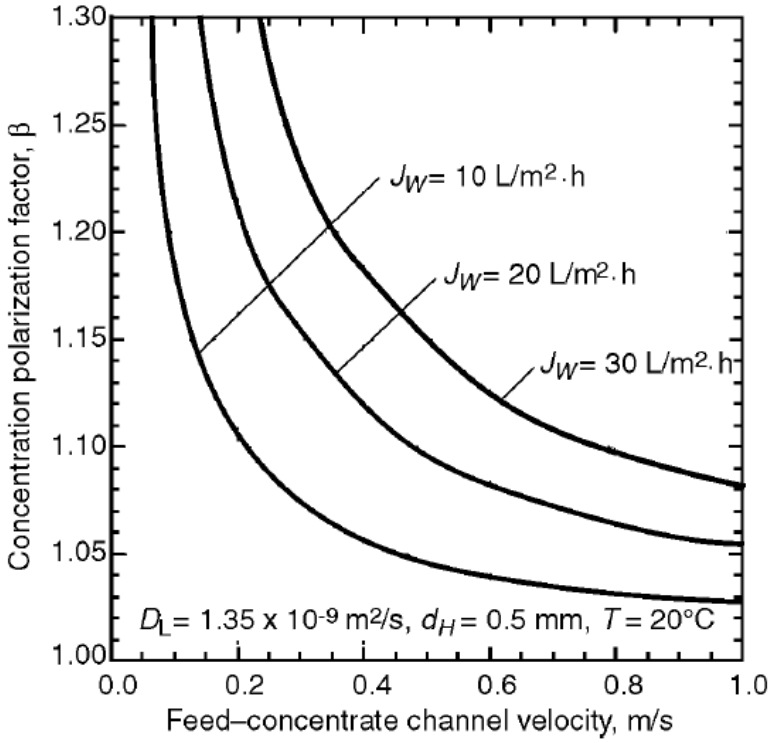

Figure 2-6 Concentration polarisation factors as a function of feed channel velocity and permeate flux. From Crittenden et al (Crittenden, Harza et al. 2012).

2.5.5 Membrane separation theory

Amongst various membrane models, two membrane separation models that accurately relate binary and multicomponent separation in RO are the solution diffusion model and the irreversible thermodynamics model. The solution diffusion model may be considered a simple non-porous model or homogenous model in which the transport mechanism is the assumption that each solvent and solute are dissolved separately onto the membrane and are then diffused through the membrane at individual flux rates. The interaction between solute, solvent and membrane are included and the phenomenological relations explains the basis for the flux rates. The quality of the membrane permeate is thus related to the mobility of the dissolved solute and the rate of its diffusion (Al-Obaidi, Kara-Zaitri et al. 2017)

The water and solute transport equations of the solution diffusion model in its simplest form and applied to the differential slice illustrated in Figure 2-7, are given by

Equation (2-7) and (2-8) respectively (Crittenden, Harza et al. 2012, Al-Obaidi, Kara-Zaitri et al. 2017)

$$J_w = A(\Delta P - \Delta\pi) = k_w\left[\left(P_{FC,Z} - P_{P,Z}\right) - \left(\pi_{M,Z} - \pi_{P,Z}\right)\right] \quad (2\text{-}7)$$

$$J_s = B(C_{FC} - C_P) = k_s\left(C_{M,Z} - C_{P,Z}\right) \quad (2\text{-}8)$$

where k_w = Water mass transfer coefficient [L.m^{-2}.h^{-1} bar^{-1}]

k_s = Solute mass transfer coefficient [L.h^{-1}]

$C_{M,Z}$ = salt concentration at the membrane surface [mol.m^{-3}]

$C_{P,Z}$ = salt concentration in the permeate [mol.m^{-3}]

$P_{FC,Z}$ = pressure in feed channel [bar]

$P_{P,Z}$ = pressure in permeate [bar]

$\pi_{P,Z}$ = osmotic pressure in permeate [bar]

$\pi_{M,Z}$ = osmotic pressure at the membrane surface [bar]

The *A* and *B* values in Equations (2-7) and (2-8) are the pure water permeability constant and solute permeability coefficient of the membrane respectively. The permeability constant A depends on the structure of the membrane and the solute permeability coefficient depends on the salt concentration and the membrane structure. (Al-Obaidi, Kara-Zaitri et al. 2017) . The values cannot be generalised and can be obtained from pilot data if not available from the membrane fabricators. (Crittenden, Harza et al. 2012).

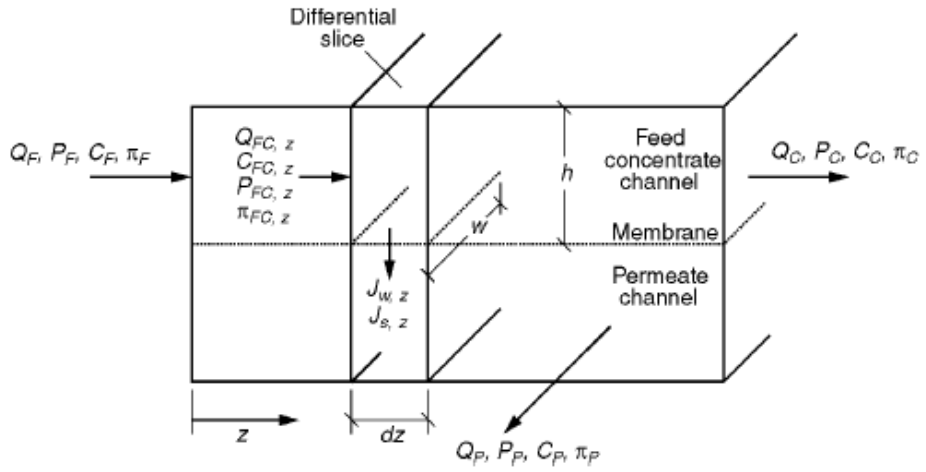

Figure 2-7 Differential slice of a spiral wound element. From Crittenden et al. (Crittenden, Harza et al. 2012)

The water and solute transfer to permeate per differential slice is determined from the product of the flux and the area of the differential slice. The cumulative transfer of water to permeate is determined by integrating the permeate flow between the feed end and z along the length of the element, Equation (2-9). The cumulative solute transfer is determined similarly, Equation (2-10).

$$Q_{P,Z} = \int_0^Z J_{w,Z} w dz \tag{2-9}$$

$$M_{S,Z} = \int_0^Z J_{s,Z} w dz \tag{2-10}$$

where

w = effective width of the feed channel [m]

$M_{S,Z}$ = moles of solute transferred [mol.s^{-1}]

2.6 PRO concentrate and neutralised ARD

Figure 2-8 lists the concentrations of macro constituents in the influent and effluent streams of ARD neutralisation plants (Martin, Loomer et al. 2013). On inspection of the major cations and anions, the inference can be made that the effluent of an ARD neutralisation plant is very similar to that of the concentrate from a brackish water PRO or NMD PRO plant. The assumption follows that the further treatment of neutralised ARD and PRO concentrate requires similar unit operations and process considerations.

The selected ICD-SNF in this research could thus be applied to effluent from an ARD neutralisation system or primary chemical demineralisation (PCD) and the concentrate of a PRO system. The resulting PCD-ICD-SNF or PRO-ICD-SNF processes will have commonality in the ICD-SNF.

Equity Silver Mine				*Geco Mine*				*Britannia Mine*				*Brunswick Mine*			
Influent		*Effluent*		**Influent**		**Effluent**		**Influent**		**Effluent**		**Influent**		**Effluent**	
pH	2.6	pH	7.0	pH	3.0	pH	8.1	pH	4.1	pH	7.5	pH	6.8	pH	8.5
SO_4	9,877	SO_4	2,823	SO_4	4,587	SO_4	3,410	SO_4	1,320	SO_4	1,310	SO_4	3,513	SO_4	3,553
Fe	924	Ca	616	Fe	1,082	Ca	868	Ca	411	Ca	502	Na	1,840	Na	1,830
Mg	919	Mg	378	Ca	336	Mg	190	Mg	63.7	Mg	52.8	Ca	118	Ca	213
Al	776	Na	30.0	Mg	176	K	51.8	Al	19.0	Na	18.1	Mg	110	Mg	102
Ca	327	Cl	25.0	K	47.7	Na	33.8	Zn	17.9	Cl	14.0	Cl	102	Cl	99.8
Cl	250	Mn	2.53	Na	29.9			Cu	17.5			Zn	72.9	K	21.0
Mn	137			Zn	12.4			Mn	4.20			Fe	32.0	Mn	6.36
Zn	123			Al	10.6							Mn	25.1		
Cu	58.9														
Fe	58.0														

Chisel North Mine				*Samatosum Mine*				*Sullivan Mine*			
Influent		**Effluent**		**Influent**		**Effluent**		**Influent**		**Effluent**	
pH	4.8	pH	7.4	pH	2.9	pH	8.8	pH	3.2	pH	8.6
Cl	1,537	Cl	1,523	SO_4	4,100	SO_4	2,900	SO_4	4,110	SO_4	3,708
SO_4	1,377	SO_4	1,353	Mg	405	Ca	793	Mg	641	Ca	761
Ca	654	Ca	757	Fe	370	Mg	339	Ca	326	Mg	455
Na	413	Na	411	Ca	343			Fe	257	Na	34.2
Mg	188	Mg	183	Zn	64.1			Zn	52.7	K	25.0
Zn	69.9			Al	11.8			Mn	45.2		
Fe	45.3			Mn	11.4			Na	36.1		
Mn	4.96			Cu	3.88			K	26.1		
								Al	20.3		

Figure 2-8 Water quality summary of ARD treatment plant influent and effluent. From MEND Report 3.44.1 (Martin, Loomer et al. 2013)

2.7 Multistage RO with intermediate chemical demineralisation

Research studies have also shown that ICD of PRO concentrate followed by SRO desalination, (PRO-ICD-SRO), can substantially improve the volumetric recovery of brackish feed waters (Gabelich, Williams et al. 2007, Rahardianto, Gao et al. 2007). For example, the ICD treatment aimed at reducing $CaSO_4$ scaling propensity through the precipitation of $CaCO_3$ has been successfully demonstrated by a number of laboratory and pilot scale studies (Rahardianto, McCool et al. 2010, McCool, Rahardianto et al. 2013).

Rahardianto et al. evaluated accelerated precipitation softening (APS) followed by microfiltration and pH adjustment to condition the concentrate stream from a PRO for additional recovery in a SRO. APS involves the addition of alkalinity to increase the pH and calcite crystal seeding of the PRO concentrate. The study methodology included laboratory RO demonstrations with corresponding membrane scaling diagnostics and mineral solubility analysis. The study concluded that a high overall volumetric recovery (> 98%) is possible with the PRO-APS-SRO sequence. The reduction in concentration of calcium, barium and strontium were >90%, >95% >78% respectively with magnesium and silica reduction in the 10 – 20% range. Significantly however, is that the study concluded that APS kinetics were favourable in the presence of antiscalant carryover. The study demonstrated that high recovery demineralisation using membrane separation is feasible using a PRO-APS-SRO process configuration (Rahardianto, Gao et al. 2007).

Gabelich et al. evaluated a two-stage reverse osmosis concept with intermediate chemical precipitation (ICP) for the desalination of Colorado River water at high overall volumetric recovery. The pilot study initially focused on the process parameters to efficiently reduce the saturation indices of sparingly soluble minerals within the PRO concentrate. Subsequently, a SRO was evaluated on the pre-treated PRO concentrate to increase the overall volumetric recovery from ~ 85% to ~ 95% for the PRO-ICP-SRO process concept. The pH at which the intermediate reactor operates was found to be a key determining factor. At a discharge pH > 10, the precipitation reactor reduced the concentrations of Ca^{2+}, Ba^{2+}, Sr^{2+} and silica at levels more than 94%, 97%, 88% and 67% respectively. The study further concluded that the sustainable operation of the PRO-ICP-SRO concept would require robust control of the precipitation reactor pH and have appropriate selection and implementation of antiscalants for primarily the control of silicates and gypsum. Operating the ICP reactor within the pH range 10.5 to 11.5 is theoretically required to reduce the saturation index of silica and thus the potential of silica scale formation (Gabelich, Williams et al. 2007).

One variation of ICD is chemically enhanced seeded precipitation (CESP) in which lime induced $CaCO_3$ precipitation precedes a seeded $CaSO_4$ precipitation step and partial concentrate recycle from the SRO desalination unit (PRO-CESP-SRO) (Rahardianto, McCool et al. 2010, McCool, Rahardianto et al. 2013). In PRO-CESP-SRO, the $CaCO_3$ precipitation step is shown to reduce the residual antiscalants concentration and,

consequently, reduce gypsum seed poisoning. In a study by McCool et al., the CESP demineralisation of PRO concentrate reduced the gypsum SR from 1.7 to 1.1 which was shown to be adequate for SRO desalination (McCool, Rahardianto et al. 2013). Greenlee et al. further investigated process alternatives for antiscalant disruption with subsequent enhanced ICD leading to improved SRO recovery (Greenlee, Testa et al. 2011).

2.8 Modelling aqueous geochemistry at high ionic strength

Ions behave independently of each other in ideal dilute solutions. As the concentration of ions increases, the activity of the ions decreases because of the interaction between the ions. The activity and activity coefficient for a chemical in water is expressed in Equation (2-11)

$$a_i = \gamma_i C_i \tag{2-11}$$

where

a_i = activity of ionic species [mole.L^{-1}]
γ_i = activity coefficient of ionic specie i
C_i = concentration of ionic species [mole.L^{-1}]

For routine calculations the activity coefficient is usually assumed to be unity, or the activity is not considered. However, when a specie in water is an electrolyte or when the ionic strength is beyond that of a dilute solution, the activity of the specie must be considered (Crittenden, Harza et al. 2012). The ionic strength can be calculated using Equation (2-12) (Stumm, Sigg et al. 1992, Crittenden, Harza et al. 2012).

$$I = \frac{1}{2}\sum_i C_i Z_i^2 \tag{2-12}$$

where I = Ionic Strength of solution, [mole.L^{-1}]
C_i = concentration of species i [mole.L^{-1}]
Z_i = number of replaceable hydrogen atoms

The equilibrium constant is the numerical value of the concentration of products over the concentration of reactants where all concentrations are raised to the power of the corresponding stoichiometric coefficient. For the reaction aA + bB ↔ cC + dD, the equilibrium constant is shown in Equation (2-13) (Crittenden, Harza et al. 2012)

$$\frac{[C]^c[D]^d}{[A]^a[B]^b} = K_c \tag{2-13}$$

where K_c = Equilibrium constant based on species concentration

In Equation (2-13) the equilibrium relationship is based on the species concentration and does not consider the activities of the aqueous constituents. Equation (2-14) presents the equilibrium relationship based on activity coefficients (Crittenden, Harza et al. 2012).

$$\frac{\gamma_c[C]^c\gamma_d[D]^d}{\gamma_a[A]^a\gamma_b[B]^b} = K \tag{2-14}$$

where K = Equilibrium constant based on species activity

It follows that the calculation of activity coefficients is essential in determining the solubility of compounds in different waters. For complex ionic systems the need for powerful predictive models are required to predict equilibrium conditions. Amongst the different activity coefficient models, all of which have different capabilities and drawbacks, Debye-Hückel, Davis, TJ, Robinson-Stokes, Guggenheim, SIT, Pitzer, e-NRTL, e-UNIFAC, e-UNIQUAC are some of the famous examples (Doubra, Kamran-Pirzaman et al. 2017).

The Pitzer model is based on empirical equations among different systems and between specific ions. It considers the range of theoretical rules which includes the effect of the

solvent. The Pitzer model has temperature and pressure dependence capability and may be applied to different types of solutions. This makes the Pitzer model popular in industrial applications (Doubra, Kamran-Pirzaman et al. 2017).

Table 2-1 provides a guide to the applicability of some activity coefficient models as a function of ionic strength of solutions. The distinction between chloride and non-chloride dominated waters are made because the experimental methods typically involve the use of chloride salts to contribute different cations to the experimental solution. Seawater is an example of a sodium chloride dominated water with an ionic strength of 0.7 M.

The type of solution, composition, temperature and pressure envelope are typically more important parameters that constrains the capability of powerful activity coefficient models. It is thus not as simple as specifying an ionic strength range within which some of these models are applicable in.

Harvie and Weare (1980) developed an equilibrium model based on the Pitzer (1973) equations for the calculation of solid liquid equilibrium in the Na-K-Mg-Ca-Cl-SO_4-H_20 system at 25^0C. The model is suggested to be accurate to high ionic strengths (20 molar). Harvie et al. extended the model to include the carbonate system and acid-base equilibria. The extended model can accurately predict mineral solubilities in the Na-K-Mg-Ca-H-Cl-SO_4-OH-HCO_3-CO_3-CO_2-H_20 system at 25^0C to high ionic strength and variable CO_2 pressure (Harvie, Moller et al. 1984).

Table 2-1 Guideline ionic strength applicability of activity coefficient models

Activity coefficient model	Applicability	Reference / Comments
Debye-Hückel limiting law	I < 0.005 M	(Crittenden, Harza et al. 2012)
Davies equation (modification of Debye-Hückel equation)	I < 0.1 M	1.5% error at I ~ 0.1M 5 – 10% error at I ~ 0.5M (Crittenden, Harza et al. 2012)
PHREEQC	I < 0.5 M	Breaks down 0.1 < I < 2. Suitable for chloride dominated water. I > 0.5M questionable results (United States Geological Survey 1999)
PHRQPITZ	I < 2M or higher	Pitzer specific interaction approach. Frequently used at 2M or higher (United States Geological Survey 1999)

Of particular importance for ICD-SNF processes, in which brackish feed waters can be concentrated to a high ionic strength with a uniquely low concentration of monovalent anions attributed to the rejection characteristics of commercially available NF membrane elements, is the Pitzer model by Harvie et al. (Harvie, Møller et al. 1984) . The Pitzer model can accurately predict thermodynamic properties at high ionic strength for solutions with compositions substantially different from that of seawater. It is shown that activity coefficients calculated by the Pitzer model (pitzer.dat) supplied with PHREEQC provide an accurate match to measured data with higher ionic strength solutions (Appelo 2015). Moreover, the complete geochemical simulation capabilities of PHREEQC are accessible to a number of software environments, e.g. Microsoft VBA and Python (Charlton and Parkhurst 2011).

The virial expansion approach can accurately represent the compositional dependence of thermodynamic properties in most multicomponent electrolyte solutions to high ionic strengths. The accurate prediction of the CO_2 activity allows for improved analysis of mineral stabilities in carbonate systems by equilibrium and activity coefficient product calculations (Harvie, Moller et al. 1984).

Activity coefficients above the dilute range depends on the relative concentrations of the major solutes present in solution. In Figure 2-9, the upper and middle curves represents the mean activity coefficient of HCl in a HCl-H_2O system and HCl in a KCl-H_2O system respectively. With the assumption that HCl, KCl and NaCl are all highly dissociated in an aqueous solution, an activity coefficient model for HCl that depends only on ionic strength cannot predict the behaviour illustrated in Figure 2-9 (Harvie, Moller et al. 1984).

2.9 PHREEQC version 3

PHREEQC version 3 is a computer program that was developed by the US Geological Survey to perform a wide range of geochemical calculations that are based on equilibrium chemistry of aqueous solutions. The aqueous models that are implemented in version 3 includes (1) the two-ion association model by Lawrence Livermore National Laboratory and WATEQ4F, (2) a Pitzer specific-ion-interaction model and (3) the Specific ion Interaction Theory (SIT) aqueous model (Parkhurst and Apello 1999).

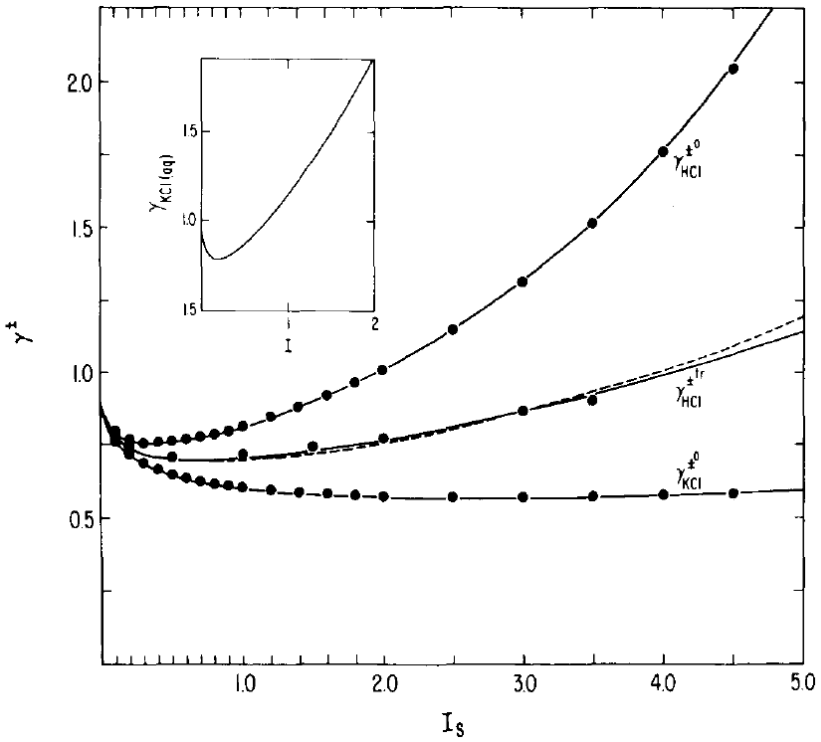

Figure 2-9 The mean activity coefficient of HCl in an HCl-H_2O system and KCl-H_2O system and the mean activity coefficient of KCl in a KCl-H_2O system. From Harvie, et al. (1984)

The calculations for which PHREEQC has capabilities and can utilise the aforementioned aqueous models includes (Charlton and Parkhurst 2011)

i. Aqueous speciation and saturation indices
ii. Batch reactions and one-dimensional transport
iii. Reversible and irreversible reactions
iv. Surface complexation
v. Ion exchange
vi. Kinetically controlled reactions
vii. Inverse modelling (finds sets of mineral and gas mole transfers to account for compositional differences)

2.10 Chemical precipitation

Precipitation, also called reactive crystallisation, takes place under high supersaturation. The induction time for precipitation is also typically in the milliseconds range where in crystallisation it can be minutes or more. Recognising this distinction is important in selecting the required methods for the analysis of precipitation (Aoun, Plasari et al. 1999).

2.10.1 Nucleation

Homogeneous nucleation occurs spontaneously and is the formation of a new crystalline solids phase from a pure solution exceeding its solubility product. This new phase will not be formed within a specified amount of time and only once an activation energy constraint has been achieved. A critical supersaturation must be exceeded before homogeneous nucleation can occur (Stumm, Sigg et al. 1992)

Heterogeneous nucleation occurs in the presence of suspended particles of a foreign substance. Heterogeneous nucleation may occur at a lower saturation ratio as the interfacial energy between two well matched solids is smaller than the interfacial energy between the crystal and the solution (Stumm, Sigg et al. 1992). Heterogeneous nucleation probably begins with the adsorption of crystallising species on the surface of solid particles thereby forming crystalline bodies that are larger than the critical nucleus size. (Coulson, Richardson et al. 1991)

A further distinction is primary nucleation that occurs in the absence of crystals and secondary nucleation that occurs in the presence of crystals. Crystals are typically already present at the conditions of industrial crystallisers and therefore secondary nucleation has a profound influence (Coulson, Richardson et al. 1991).

The induction period is the delay between the attainment of a supersaturated state and the detection of newly created crystals in solution. The induction period is a complex parameter that includes both nucleation and growth components. The measurements of induction periods, although notoriously unreliable, provides pertinent information on other phenomena in crystallisation, e.g. the effect of impurities (Coulson, Richardson et al. 1991).

2.10.2 Crystal growth

Like nucleation, crystal growth rates are usually expressed in terms of supersaturation by an empirical relationship. The crystal growth rate is decisively influenced by two physical stages – a diffusional step and an integration step. In the diffusional step the solute is transported through the solution boundary layer adjacent to the crystal and adsorbed at the crystal surface. In the integration step, the adsorbed solute ions or molecules are integrated into the crystal lattice (Coulson, Richardson et al. 1991).

The two stages are shown in Figure 2-10. After some derivation to eliminate the interfacial concentration, c_i, the mass deposition rate dm/dt is expressed in terms of the overall concentration driving force ($C - C^*$), diffusion mass transfer coefficient k_d, integration mass transfer coefficient k_r and order of integration i in Equation (2-15) (Coulson, Richardson et al. 1991).

$$(C - C^*) = \left(\frac{1}{k_d}\right)\frac{dm}{dt} + \left(\frac{1}{k_r}\right)\left(\frac{dm}{dt}\right)^{1/i} \tag{2-15}$$

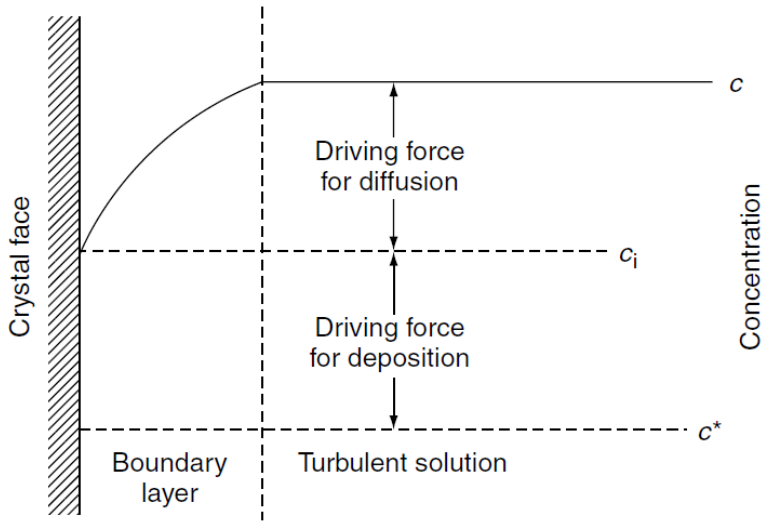

Figure 2-10 Concentration driving forces for crystal growth.
From (Coulson, Richardson et al. 1991)

Aoun et al. developed a method to derive the nucleation and crystal growth rates from the simultaneous measurement of supersaturation and crystal size distribution during a batch

spontaneous precipitation. They derived Equation (2-16) and (2-17) as the main equations for an iterative non-linear optimization of crystal growth rate for given values of k_r and r. Equation (2-16) is the precipitation extent X at time t

$$X(t) - X(t_0) = \frac{3\phi_v \rho_c}{M_s C_s(t \to \infty)} \int_{t_0}^{t} \int_{0}^{\infty} L^2 \, \psi(L,t) G(L,t) dL dt \tag{2-16}$$

where

$\psi(L,t)$	=	number crystal size distribution at time t
$G(L,t)$	=	linear crystal growth rate [m.s^{-1}]
ϕ_v	=	volumetric shape factor
ρ_c	=	density of solids phase [kg.m^{-3}]
C_s	=	Concentration of solid phase [mol.m^{-3}]
L	=	crystal size [m]
M_s	=	Molar mass of solids phase [kg.mol^{-1}]

Aoun et al. further combined the classical relationship that emanates from the assumption of no mass accumulation at the interface, with a simple power law expression for the crystal growth rate. This combination resulted in the overall growth rate expression given by Equation (2-17) (Aoun, Plasari et al. 1999).

$$\left[\frac{G(L,t)}{k_r}\right]^{1/r} + \frac{3\rho_c \phi_v G(L,t)}{M_s k_d \phi_s} = C(t) - C^* \tag{2-17}$$

where

k_r	=	growth rate parameter [m.s^{-1}(mol.m^{-3})$^{-r}$]
r	=	crystal growth kinetic order
k_d	=	mass transfer coefficient [m.s^{-1}]
ϕ_s	=	surface shape factor
$C(t)$	=	Concentration of solution [mol.m^{-3}]
C^*	=	Equilibrium concentration [mol.m^{-3}]

The method used by Aoun et al. to identify the crystal growth parameters was to solve Equation (2-17) for assumed values of k_r and r and using $C(t)$ from the experimental de supersaturation curve to yield the crystal growth rate $G(L,t)$. They evaluated k_d using the Armenante and Kirwan mass transfer correlation, expressed in Equation (2-18). The precipitation extent, Equation (2-16), was then evaluated for the postulated $G(L,t)$ and the experimental $G(L,t)$. An iterative process was used to minimise the error between the postulated and experimental growth rate thus yielding k_r and r (Aoun, Plasari et al. 1999).

$$\frac{k_d L}{D} = 2 + 0.52\left(\frac{L^{4/3}P^{1/3}}{v}\right)^{0.52}\left(\frac{v}{D}\right)^{0.33} \tag{2-18}$$

The Armenante and Kirwan mass transfer correlation, Equation (2-18), is especially suited to particles smaller than 30 μm.

2.10.3 Calcium sulphate dihydrate (Gypsum) precipitation

The three phases of calcium sulphate typically encountered naturally or in scales are calcium sulphate dihydrate ($CaSO_4.2H_2O$), calcium sulphate hemihydrate ($CaSO_4.½H_2O$) and anhydrous calcium sulphate ($CaSO_4$). The formation of each is dependent on temperature and pressure. In Figure 2-11, the typical prisms of gypsum are shown in a scanning electron micrograph (Klepetsanis and Koutsoukos 1991).

Calcium sulphate dihydrate, $CaSO_4.2H_2O$ is the most abundant naturally occurring sulphate where it plays a major role in geological and environmental processes. In the industry, gypsum finds it use in construction, agriculture, cosmetics and the food industry. In the process industries, calcium sulphate scale formation is a major issue that affects process uptime and efficiency. The gypsum crystal is a monoclinic system consisting of SO_4^{2-} tetrahedra bound by Ca^{2+} cations with water molecules arranged between the layers (Aquilano, Otálora et al. 2016).

It is possible to study the spontaneous precipitation of calcium sulphate dihydrate in the temperature range 20 to 60°C at conditions of sustained supersaturation using conductivity measurements. The solids phase forms in supersaturated aqueous solutions

by a polynuclear mechanism with a high activation energy which is typical of surface controlled processes (Klepetsanis and Koutsoukos 1991).

The gypsum precipitation and dissolution reaction is given in Equation (2-19) and the expression for the saturation ratio in Equation (2-20).

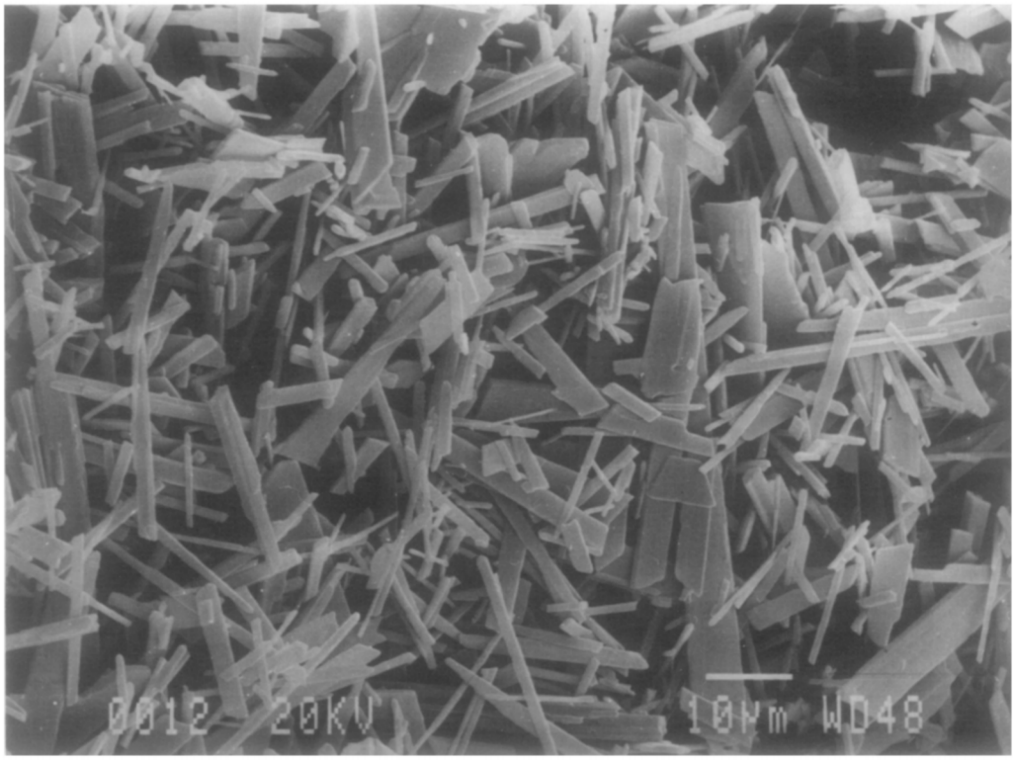

Figure 2-11 Typical prisms of gypsum formed between 20 and 60°C. From (Klepetsanis and Koutsoukos 1991)

$$Ca^{2+} + SO_4^{2-} + 2H_2O \leftrightarrow CaSO_4.2H_2O \tag{2-19}$$

$$SR = \frac{\{Ca^{2+}\}\{SO_4^{2-}\}}{K_{Gypsum}} \tag{2-20}$$

The presence of metal ions can inhibit the rate of gypsum precipitation. Hamdona and Hadad found the rate of inhibition to depend on the type and concentration of the metal ion as well as the degree of gypsum saturation. They did not find complete inhibition of the precipitation rate at any metal concentration (Hamdona and Al Hadad 2007).

Klepetsanis and Koutsoukos investigated the effect of organophosphorus additions to supersaturated gypsum solutions at 30°C and pH 7.0. Induction times were substantially increased and precipitation rates substantially decreased. For example, nitrilotrimethylene phosphonic acid and N,N,N',N'-ethylene diaminotetramethylene phosphonic acid reduced precipitation rates by 90% at concentrations below 1μM. The preceding induction times were also drastically increased. The morphology of the precipitated crystals suggested that the increased induction time and decreased precipitation rates could be attributed to the adsorption of the organophosphorus additives onto different gypsum crystal faces (Klepetsanis and Koutsoukos 1998).

Gypsum has a specific gravity of 2.312 to 2.322 and a hardness of 2 on Mohs scale (mindat.org).

2.10.4 Calcite precipitation

Calcite is the primary mineral in limestone and the most common carbonate mineral in carbonate rocks. It precipitates from supersaturated water by biochemical or direct precipitation processes and is the stable polymorph of $CaCO_3$ at room temperature and pressure. The structure is rhombohedral with strong anisotropy introduced by the planar and triangular CO_3^{2-} ions (Aquilano, Otálora et al. 2016).

Uncertainties in the prediction of activity coefficients of carbonate ions in highly concentrated brines, can impart substantial error to kinetic rate models that empirically describe the rate as a function of the approach to equilibrium or 1 – activity product divide by solubility product (1-IAP/Ksp) (Gledhill and Morse 2006)

The study is different from the aforementioned ICD-SRO processes (Gabelich, Williams et al. 2007, Rahardianto, Gao et al. 2007, Rahardianto, McCool et al. 2010, McCool, Rahardianto et al. 2013) in that (1) a lengthy cycling up phase leads into a steady state phase, (2) the order of calcite and gypsum precipitation reactors is reversed to confine gypsum to higher SR ratios for driving force and then to utilise calcite precipitation to reduce gypsum SR to a targeted range that supports the feed requirements to SNF, and (3) the process model incorporates all the streams to which aqueous and solids species can report to in order to estimate steady state point of ICD-SNF with near total recycle.

The cycling up and subsequent approach to steady state of the recirculation liquor TDS were experimentally observed. The pilot objective was successful in proving the concept of the selected ICD-SNF variation.

3 PILOT STUDY OF ICD-SNF

A continuous pilot for the treatment of primary RO (PRO) concentrate was conducted at a mine water treatment plant in Ghana. The process design philosophy was to target a high volumetric recovery to minimise the requirement for handling RO concentrate in the site wide water balance and to minimise the sludge waste volumes for onsite storage. An intermediate chemical demineralisation (ICD) with secondary nanofiltration (SNF) and near total SNF concentrate recycle process was selected to achieve the design philosophy. The selected ICD-SNF with recycle variation is depicted in Figure 3-1.

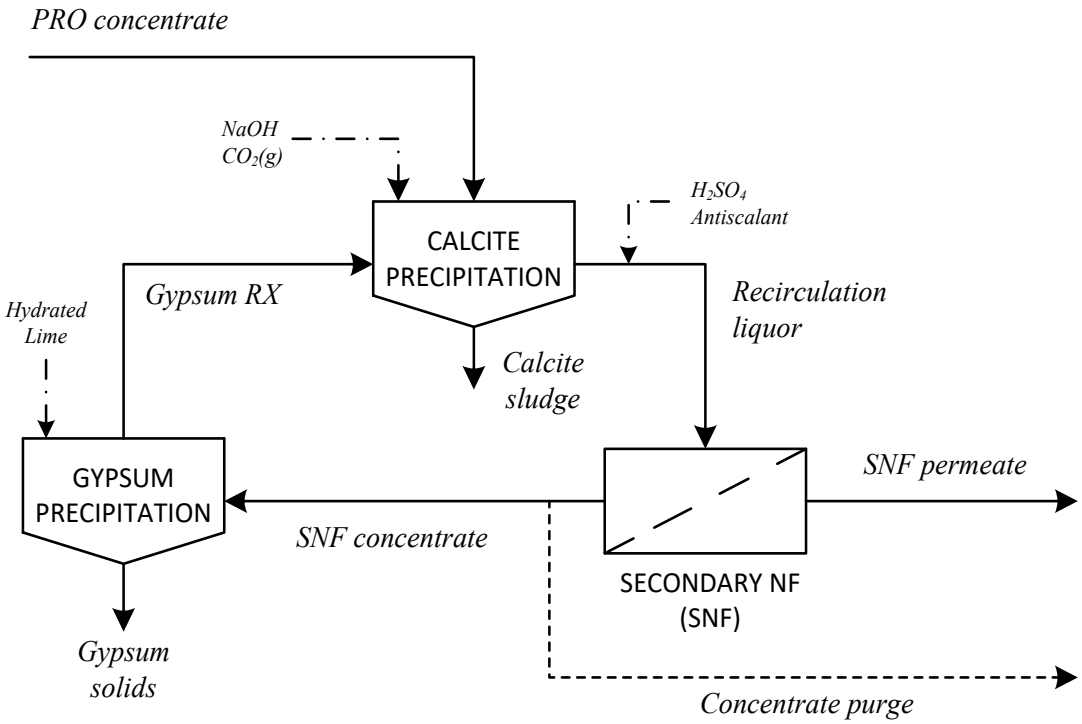

Figure 3-1: Selected ICD-SNF variation for pilot and process model objectives

In the selected ICD-SNF variation, lime induced gypsum precipitation preceded CO_2 induced calcite precipitation so that gypsum precipitation would be confined to higher SRs and thus a higher reaction driving force would be maintained. Subsequently, CO_2 induced calcite precipitation would further reduce the gypsum SR in preparation for a secondary NF (SNF) stage from which the resulting concentrate, with high gypsum SR, would be recycled to the gypsum precipitation reactor. The SNF was selected over SRO

as higher monovalent salt passage would be beneficial to the precipitation reactors and the membrane system. The benefit to precipitation reactors is attributed to minimising the solubility elevation of sparingly soluble minerals as the ionic strength increases and the benefit to membrane systems with respect to system pressure and corrosion in high chloride liquors.

The PRO-ICD-SNF process evaluated in this research is different from the ICD-SRO processes described in section 2.7 of the literature survey (Gabelich, Williams et al. 2007, Rahardianto, Gao et al. 2007, Rahardianto, McCool et al. 2010, McCool, Rahardianto et al. 2013) in that a lengthy cycling up phase leads into a steady state phase. The order of calcite and gypsum precipitation is also reversed to confine gypsum to higher SR ratios for driving force and then to utilise calcite precipitation to reduce gypsum SR to a targeted range that supports the feed requirements to SNF.

The ICD-SNF experiment was conducted for over 350 hours. The intent of the experiment was to prove the concept and to observe the evolution of dissolved species in the recirculated bulk liquor.

3.1 Experimental setup

The calcite precipitation reactor consisted of four agitated compartments housed in a square polypropylene shell with a total working volume of 2 m^3 and agitation rate of 60 rpm for each compartment. The feed to the first compartment included PRO concentrate, process recycle from gypsum precipitation and 15 wt. % caustic soda for controlling the final compartment pH at ~ 10.5. Technical grade CO_2 was injected through an inline high shear modified Abrimix unit in recirculation mode at a dosage rate manually adjusted between 0.5 and 1.5 kg/h to target a discharge calcium concentration of 400 $mg.L^{-1}$. The instantaneous CO_2 injection rate was measured by a gas phase rotameter that was maintained at the calibrated pressure with a pressure regulating valve. The average CO_2 consumption was confirmed gravimetrically by measuring the weight loss of the 40 kg CO_2 storage cylinders. The average CO_2 consumption was used to calibrate the rotameter data.

A high rate 5m^3 sludge contact clarifier and 1m^3 auxiliary polyethylene tank provided solid liquid separation of the calcite precipitation liquor. Calcite sludge was periodically

discharged from the clarifier into the auxiliary tank that allowed further natural dewatering. The recovered water was returned to a $2m^3$ polypropylene ultrafiltration (UF) feed tank. The maximum average solids content of the discharged calcite sludge increased to 18 wt. % during the steady cycling up stage of the experiment.

The clarified calcite precipitation liquor was ultra-filtered (Jalema Technologies UF-10 system) in a capillary UF module (Model HYDRAcap60, 46 m^2 nominal membrane area, Hydranuatics) operated at an average flux rate of 53 $L.m^{-2}.h^{-1}$. The pH of the UF feed was adjusted using 7% w/w sulfuric acid to pH 5.5 to avoid the pH range in which calcite scaling would occur and to enhance the transmission of monovalent anions associated with the hydronium ion to NF permeate. The UF was configured to have an inside to outside filtration direction with a cross flow that averaged 10% of the feed flow. The cross flow was returned to the first compartment of the calcite precipitation reactor. Non-chemical backwash sequences were performed at intervals of 30 min with a duration of 60 seconds. The backwash waste reported to the first compartment of the precipitation reactor similarly to the UF crossflow.

The NF feed was pre-treated with antiscalant (Genesys CAS) at a dosage rate of 10 ppm before it was fed to a Jalema Technologies NF system configured in a 2:1 array of 4 inch SS316L pressure vessels loaded with thin film composite NF elements (Model Membrane Development Specialists MDS 4040T NF, 7.34 m^2 active area). The average permeate flux and volumetric recovery of the NF system was 17.1 $L.m^{-2}.h^{-1}$ and 50% respectively. Permeation rates were balanced over the element string by imposing a 120 kPag back pressure on the lead array permeate manifold. The element feed channels were intermittently (30min intervals typically) flushed by cycling the concentrate flow control valve. The constant volumetric feed flow rate was maintained by the positive displacement Hydracell pump and the recovery was manually set by adjusting the position of a needle valve.

The gypsum precipitation reactor consisted of four agitated compartments housed in a mild steel shell with a total working volume of $2.3m^3$ and a agitation rates of 75 rpm for each compartment. An integral clarifier separated the gypsum sludge for seeding and transport to an integral screw conveyor for thickening. Separation aids were not introduced to enhance clarification and consequently the bulk liquor discharge from the

gypsum clarifier contained suspended solids at a concentration range between 300 and 1000 ppm.

The total liquid holdup of the experimental setup was approximately 14.9 m^3 and is proportional to the rate at which cycling up or accumulation of dissolved aqueous species in the recirculation liquor occurs. A gradual loss in liquid holdup would accelerate the cycling up whereas a gradual increase would buffer the cycling up process.

3.2 Data collection: analytical chemistry and process variables

Measurements generated by process instrumentation and handheld analysers were logged onto a local PLC (PRO EC, pH, flow rate) and onto log sheets (ICD and SNF EC, pH and flow rates) on an hourly basis. The pH and temperature of the calcite and gypsum precipitation compartments, the UF feed and the NF feed, permeate and concentrate streams were measured using a Mettler Toledo SevenGo Duo handheld instrument with a PRO-ISM-IP67 pH probe. The electrical conductivity of the NF feed, permeate and concentrate streams were measured using a Mettler Toledo SevenGo Duo handheld instrument with a 738-ISM conductivity probe. Inline pressure gauges measured the CO_2 injection pressure, UF differential pressure, NF feed, interstage and concentrate pressure. Hydrated lime addition rate was gravimetrically determined using a Radwag® WTB 2000 balance. Rotameters measured the volumetric flow rates of the NF feed, permeate and concentrate, the UF feed and permeate, and calcite precipitation reactor discharge.

The calcium hardness of the precipitation reactor discharge and NF feed was determined using the Palintest® PHOT .12 Calcicol method. The gypsum and calcite sludge moisture content were gravimetrically determined using a Radwag® WTB 2000 balance.

Three sets of samples were analysed for a range of parameters such as pH, total dissolved and suspended solids, concentrations of dissolved constituents, electrical conductivity, and alkalinity by an accredited laboratory. The aqueous samples were filtered with a 0.45 µm syringe filter at the collection point and subsequently refrigerated. The physicochemical analysis and corresponding American Public Health Association (APHA) protocols included pH (APHA SM 4500 H), total dissolved solids (APHA SM 2540 B and 2540 C), electrical conductivity (APHA SM 2510), turbidity (APHA SM 2130 B), and total alkalinity (APHA SM 2310 B and 2320 B). Metals in

aqueous samples were analysed using inductively coupled plasma mass spectrometry (ICP-MS). The Na, K, Ca and Mg ions were analysed according to APHA SM 3120 and US EPA 6010/200.7 and Fe, Mn and Sr ions were analysed according to US EPA 6020/200.8 and 200.2. The aqueous samples included the PRO concentrate, gypsum and calcite precipitation reactor liquor, SNF feed, SNF permeate and SNF concentrate streams.

X-ray diffraction was used to identify the solids phases in the calcite and gypsum sludges. The sludge samples were analysed using a PANalytical Empyrean diffractometer with PIXcel detector and fixed slits with Fe filtered Co-Kα radiation. The phases were identified using X'Pert Highscore plus software and the relative phase weight percentages were estimated using the Rietveld method.

3.3 Experimental results

A lengthy period of developing conditions, approximately 250 to 300 hours, led to a steady state that corresponds with the steadying out of the recirculation liquor EC. This cycling up was tracked through electrical conductivity measurements of the SNF feed (Figure 3-1 – Recirculation liquor). The PRO concentrate was fed to the calcite precipitation reactor at a rate of 0.98 m^3/h. The cycling up characteristics of the aqueous species in the recirculation liquor (Figure 3-2) were grouped into four stages that corresponded to the developing process conditions and experimental parameters (Table 3-1). Refer to Appendix B1 for the hourly logged data.

A recirculation process was initially established at a lower PRO concentrate strength and minimal dewatering of calcite and gypsum sludge streams to dampen the cycling up rate. The accelerated cycling up or accumulation stage was initiated by ramping up the strength of the PRO concentrate and increasing the dewatering and sludge moisture recovery efficiency of the sludge streams. The steady cycling up stage was initiated by decreasing the volumetric recovery of the SNF and thereby increasing the recirculation load. A steady state stage developed from the steady cycling up stage as the increase in electrical conductivity (EC) of the recirculation liquor appeared to cycle around an average of 18500 $\mu S.cm^{-1}$ (corresponding TDS 17760 $mg.L^{-1}$) and an ionic strength of 0.37 molar. The cycled up ionic strength of the NF concentrate was 0.75 molar.

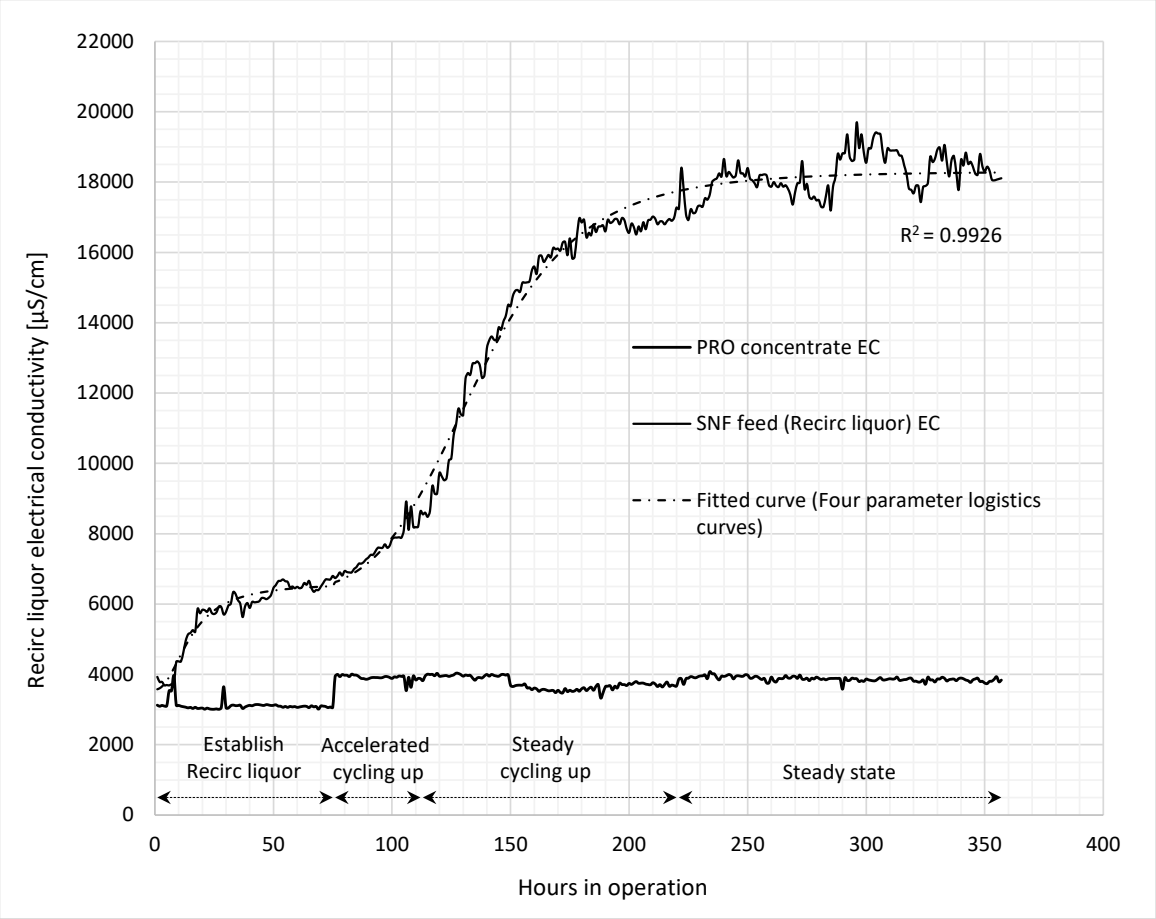

Figure 3-2 Accumulation of dissolved aqueous species, measured using aqueous phase EC, in the recirculation liquor

The cycling up of the recirculation liquor EC was fitted (Figure 3-2; Fitted curve; R^2 = 0.9926) using a four parameter logistic curve for hours 0 to 75 (Establish recirculation stage) and for hours 76 to 357 (Accelerated cycling up, steady cycling up and cyclic operation stages). The rate of change in recirculation liquor EC at discrete points (EC values) along the cycling up curve was evaluated to determine the approach to steady-state. The rate of change in recirculation EC shown for the fitted experimental data, approaches zero as the recirculation liquor EC approaches 18500 µS.cm^{-1} (Figure 3-3). The experimental results thus suggest that, for the operating parameters of Table 3-1, the

recirculation liquor EC will cycle up to approximately 18500 µS.cm^{-1} in the treatment of the PRO concentrate, with total recycle of SNF concentrate (zero concentrate purge). Refer to Appendix B1 for the hourly logged data.

Table 3-1 Experimental stages and corresponding process operating parameters

		Establish recirculation	Accelerated cycling up	Steady cycling up	Steady state operation
Hours in operation		0-75	76-112	113-220	221-357
Average PRO concentrate EC	µS.cm^{-1}	3113	3909	3746	3873
Calculated PRO concentrate TDS (K = 1.04)	mg.L^{-1}	3238	4065	3896	4028
Average NF recovery	vol. %	60	60	50	50
Calcite sludge solids	wt. %	2	4 - 8	12 - 18	18
Gypsum sludge solids	wt. %	20	25 - 30	30 - 41	41

The cyclic nature of the steady state stage, around a SNF feed EC of 18500 µS.cm^{-1}, is attributed to manual control of the CO_2 and caustic dosing to the caustic precipitation reactor and the periodic discharge of calcite sludge. Both dosing and sludge discharge activities induced cyclic response due to the increase in sodium loading and decrease with slow replenishment in total liquid inventory respectively.

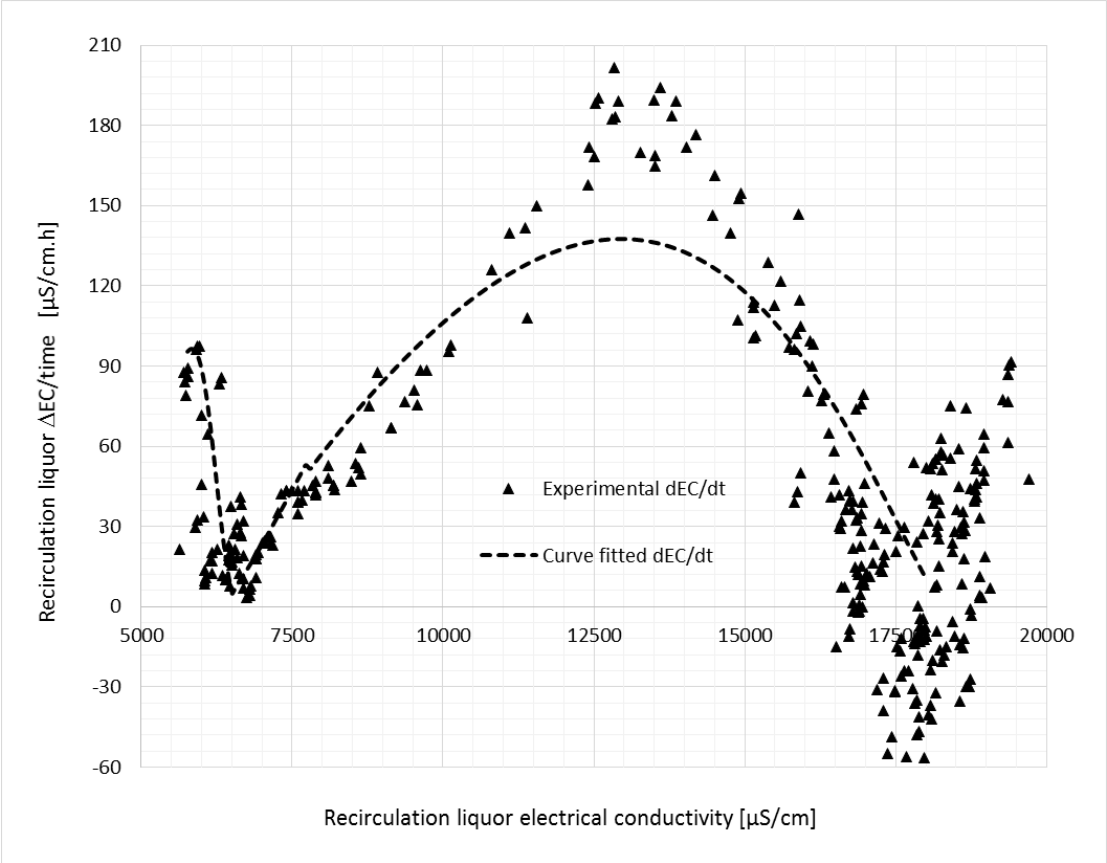

Figure 3-3 Rate of change of recirculation liquor EC vs cycled up recirculation liquor EC

3.4 Membrane Performance

Membrane performance evaluation was not part of the study due to (1) the total run time being less than a typical run-in time of 500 hours, (2) the relatively long duration of the cycling up phase before steady operation can be monitored with normalised permeate flux plots and (3) the necessary instrumentation and equipment was omitted as the primary focus was to demonstrate the proof of concept.

Some observations were however made and are summarised as follows:

i. Gypsum scaling with celestite inclusions did occur (Figure 3-4) and is attributed to cyclic performance of the calcite reactor with subsequent high gypsum SR in the SNF;

ii. The NF element string was too long and due to the high permeability of the MDS NF 4040 elements the cross-flow velocities in the tail elements would have been insufficient;

iii. Although the gypsum SR was well within the antiscalant control envelope, the operating pH of the SNF was too low and would have resulted in protonation of the antiscalant and thus ineffective scale inhibition;

iv. A 12.5% heated NaCl solution was effective as a clean in place (CIP) protocol to restore element performance.

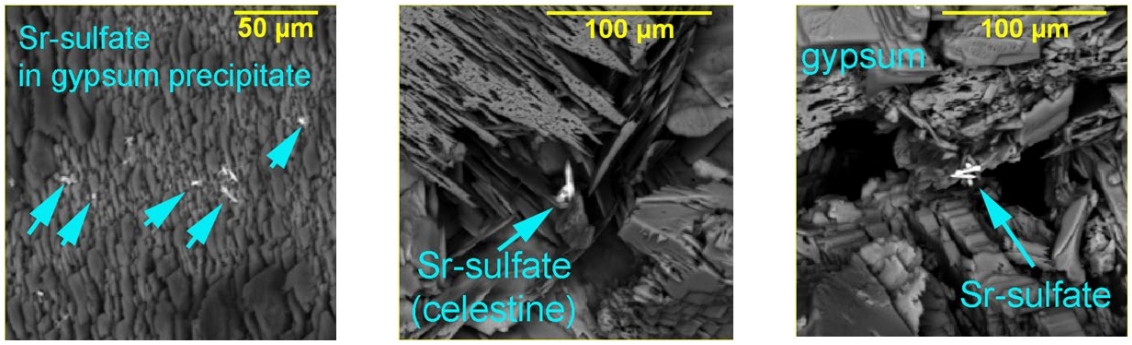

Figure 3-4 SEM images of gypsum scaling with celestite inclusions on SNF elements

3.5 Analytical Results

Samples of the major process streams were collected at 158, 203 and 297 hours in operation and sent for chemical analysis at SGS Tema, an accredited external laboratory. The TDS to EC ratios of the PRO concentrate were 1.10, 0.98 and 1.05 at the sampling hours. Similarly, the TDS to EC ratios of the SNF feed were 0.95, 0.97 and 0.95. The PRO concentrate TDS values in Table 3-1 were calculated from the average PRO concentrate TDS to EC ratio (1.04).

Refer to the following appendices for the analytical results provided by SGS Tema. Refer to section 3.2 for the analytical protocols that were used

i. Appendix A1: ICD-SNF Feed / Primary RO Concentrate
ii. Appendix A2: SNF Feed / Recirculation liquor
iii. Appendix A3: SNF Concentrate
iv. Appendix A4: SNF Permeate
v. Appendix A5: Gypsum reactor discharge
vi. Appendix A6: Calcite reactor discharge
vii. Appendix A7: Feed water to RO plant

The analytically determined compositions of the major process streams at the cycled-up state (samples analysed at 297 hours in operation) are listed in Table 3-2. The TDS and EC values reported by the external laboratory were lower than expected. The TDS was lower than the sum of the dissolved aqueous species and the EC was lower than the corresponding EC value reported in Figure 3-2. However, applying the TDS to EC ratios to the sum of the dissolved aqueous species in the SNF feed, yielded analytical EC values that were in line with the experimental EC values trended in Figure 3-2 at the corresponding hours in operation. It was therefore assumed that the TDS / EC ratio of the chemical analysis is adequate regardless of the under reported TDS and EC values.

The analytical chloride values were expected to be similar for all the samples as a characteristic of the MDS NF elements is near complete passage of monovalent anions and thus chloride would not cycle up in the ICD-SNF process. The analytically

determined chloride and nitrate-N values are under reported for the more concentrated samples. This can be attributed to negative rejection in the SNF which is possible due to the electromigration transport phenomena of NF elements and / or the under reporting of photometric analysis due to the solubility elevation with ionic strength. The latter is possible if an insufficient dilution ratio was used in the analysis of the samples.

Table 3-2 Analytical results at 297 hours into operation

		PRO concentrate	Calcite reactor	Gypsum reactor	SNF feed	SNF concentrate	SNF permeate
pH		5.6	11.4	12.5	4.8	4.6	5.3
TDS	$mg.l^{-1}$	4300	17950	29100	16750	32900	686
EC	$\mu S.cm^{-1}$	4110	17600	48000	17600	47800	980
Calcium	$mg.L^{-1}$	842	561	743	537	1050	< 1
Magnesium	$mg.L^{-1}$	156	1.8	< 0.5	26.9	50.7	< 0.5
Sodium	$mg.L^{-1}$	168	5990	10100	5530	9790	194
Potassium	$mg.L^{-1}$	23.3	244	462	238	494	7.2
Chloride	$mg.L^{-1}$	30.9	12.1	< 0.1	12.4	< 0.1	33.6
Sulphate	$mg.L^{-1}$	2830	15300	22300	13600	24700	146
Silica	$mg.L^{-1}$	112	1.1	7.7	13	14.0	11.7
Strontium	$mg.L^{-1}$	46	19	19	18	26.0	0.2
Nitrate-N	$mg.L^{-1}$	68.7	32.1	4.5	35.7	2.8	66.0

Table 3-3 shows the evolution of aqueous species in the SNF feed and the SNF permeate. Sodium and sulphate cycled up in the recirculation liquor. The salt passage of chloride and nitrate through the MDS NF elements were near complete and thus sodium and nitrate did not cycle up in the recirculation liquor. The concentrations of calcium, magnesium, silica and strontium were dependent on the extent of the precipitation reactions in the calcite and gypsum reactors. Calcium reported to the gypsum ($CaSO_4.2H_2O$) and calcite ($CaCO_3$) solid phases, magnesium reported to brucite ($Mg(OH)_2$) and enstatite ($MgSiO_3$)

solids phases, silica reported to the enstatite solids phase and strontium reported to the celestite ($SrSO_4$) solids phase.

The XRD analysis identified calcite and gypsum in the gypsum sludge at 1.04 and 99.0 weight % respectively. In the calcite sludge, calcite, gypsum, brucite and enstatite were identified at 92.87, 4.4, 1.06 and 1.66 weight % respectively. The XRD analysis was useful in identifying phases, however not considered sufficiently accurate for mass balance verification.

Table 3-3 Evolution of dissolved aqueous species in SNF feed and permeate

Process stream		SNF Feed	SNF Permeate	SNF Feed	SNF Permeate	SNF Feed	SNF Permeate
Hours in operation		158	158	203	203	297	297
TDS	$mg.l^{-1}$	11700	696	15150	750	16750	686
EC	$\mu S.cm^{-1}$	12300	940	15600	980	17600	980
Sodium	$mg.L^{-1}$	3400	186	4480	188	5530	194
Sulphate	$mg.L^{-1}$	9100	109	11200	152	13600	146
Chloride	$mg.L^{-1}$	23.5	45.2	13.8	34.5	12.4	33.6
Calcium	$mg.L^{-1}$	545	< 1	460	< 1	537	< 1
Magnesium	$mg.L^{-1}$	45.1	< 0.5	48.2	< 0.5	26.9	< 0.5
Silica	$mg.L^{-1}$	18.1	14.3	27.3	24.6	13.0	11.7
Strontium	$mg.L^{-1}$	28.0	0.1	20.0	0.9	18.0	0.2
Nitrate-N	$mg.L^{-1}$	34.8	52.9	35.7	71.4	35.7	66

The solids phase saturation ratios were calculated by PHREEQC using the same database (pitzer.dat) used in the process model. The saturation ratios (SR), defined as per PHREEQC definition of $SR_x = IAP_x/K_{sp,x}$, are shown in Table 3-4 at 158, 203 and 297 hours into operation. The gypsum SRs in the gypsum precipitation reactor increased with time. This is attributed to process conditions at the time of sampling rather than a relationship with increasing ionic strength. The geochemical calculations performed by PHREEQC takes the solubility elevation with increasing ionic strength into account

through the activity coefficient model. The gypsum SRs in the calcite reactor were indirectly lowered through the reduction of dissolved calcium because of calcite precipitation. This was the design intent of the calcite reactor. The lowering of the gypsum SR is the primary target for SNF feed preparation in an ICD-SNF process. The calcite SR in the calcite reactor is indicative of a precipitation extent that was substantially departed from an approach to equilibrium (SR ~ 1). Similar to the gypsum SR in the gypsum reactor, the calcite SR increasing with time is not attributed to increasing ionic strength with time but rather the performance of the precipitation reactor at the time of sampling.

Table 3-4 Saturation ratios of solids phases calculated from experimental data

Process stream	Gypsum precipitation reactor			Calcite precipitation reactor		
Hours in operation	158	203	297	158	203	297
Brucite SR	4.7	3.7	3.2	0.03	14.3	3.5
Calcite SR	95.5	142	220	135	250	265
Celestite SR	0.08	1.6	2.1	3.9	2.0	2.2
Gypsum SR	1.16	1.3	1.45	1.26	0.75	1.12

4 PROCESS MODEL DEVELOPMENT AND CALIBRATION

In this chapter the development of an equilibrium process model of the selected variation of the PRO-ICD-SNF process and the subsequent calibration to the results of the ICD-SNF experiment is presented in sections 4.1 and 0 respectively. The experimental work used for the calibration is presented in Chapter 3.

4.1 Equilibrium process model

The Pitzer specific-ion-interaction aqueous model incorporated in PHREEQC version 3 was accessed from Microsoft Visual Basic for Applications through the COM server module of PHREEQC. The aqueous speciation, equilibrium phase and batch reaction calculation capabilities of PHREEQC were integrated with an algorithm (Figure 4-1) that was designed to determine the steady state cycled up mass balance of the process depicted in Figure 3-1 for a set of experimentally achieved process parameters listed in Table 4-1 and Table 4-2. The aqueous chemical system, Na-K-Mg-Ca-Sr-H-Cl-SO_4-OH-HCO_3-CO_3-CO_2-H_2O together with equilibrium phase solids, brucite, calcite, celestite, gypsum, magnesite and portlandite were defined.

The mass balance of a simulation unit in the process can be described in terms (see Equation (4-1)) of (1) the sum of the water mass in each feed stream, (2) the sum of the solute mass in each feed stream, (3) the sum of solids phases associated with feed streams and solid phase reagents, (4) the sum of chemical reagents, (5) the sum of solids phases in the discharge stream and (6) the water and solute mass that reports to the discharge streams, sludge moisture and UF cross flow. The generation and consumption of solute components are calculated by PHREEQC and the results incorporated in the 5th and 6th terms of the mass balance equation:

$$\sum_{j}^{nF_0} L_{j0} + \sum_{j}^{nF_0}\sum_{i}^{nC} L_{j0}C_{ij0}M_i + \sum_{k}^{nP} S_{k0}M_k + \sum_{r}^{nR} N_r M_r - \sum_{k}^{nP} S_k M_k - \left(\frac{L}{1 - f_{SM} - f_{CF}}\right).\left(1 + \sum_{i}^{nC} C_i M_i\right) = 0 \quad (4\text{-}1)$$

Where

L_{j0}	Water mass flow rate of feed stream *j*
L	Water mass flow rate of output stream excluding sludge moisture or UF cross flow
C_{ij0}	Concentration of aqueous specie *i* in feed stream *j0*
M_i	Molecular weight of aqueous specie *i*
M_k	Molecular weight of solids phase *k*
M_r	Molecular weight of reagent *r*
nF_0	Number of feed streams
nC	Number of aqueous species components
N_r	Molar flow rate of reagent *r*
S_{k0}	Molar flow rate of feed solids phase *k*
S_k	Molar flow rate of output solids phase *k*
f_{CF}	Fraction of output liquid phase reporting to membrane waste (cross flow)
f_{SM}	Fraction of output liquid phase reporting to sludge moisture

The following process units were defined in the ICD-SNF

i. Calcite precipitation reactor: Feed streams included the gypsum reactor discharge, the PRO concentrate, the secondary UF (SUF) cross flow and backwash streams. Reagents included CO_2 and NaOH. Solids phase feeds included carryover from the gypsum reactor and the SUF crossflow. Solids phase output reported to the calcite clarifier sludge and carryover associated with the discharge water. A fraction of the discharge water was lost to calcite sludge moisture;

ii. SUF feed: The calcite clarifier overflow water and carryover solids phase reported to the SUF feed where H_2SO_4 was used in the first stage pH reduction;

iii. SUF discharge: H_2SO_4 was used in the second stage pH reduction. A fraction of the discharge water reported to the calcite reactor as SUF crossflow and backwash. The solids phase output reported to the UF crossflow fraction and back to the calcite precipitation reactor;

iv. SNF: The permeate and concentrate streams compositions were determined using Equations (4-4) and (4-5). The algorithm included a mechanism to adjust the permeate and concentrate pH targets to minimise the sodium error (sodium is manipulated to achieve ion balance in the permeate and concentrate streams). Solids phase calculations were inactive for the SNF unit;

v. Gypsum precipitation reactor: Feed streams included the SNF concentrate and lime slurry liquor. The lime slurry liquor also included the solids phase feed. Solids phase output reported to the gypsum sludge from the gypsum screw conveyor and carryover to the calcite precipitation reactor. A fraction of the discharge water was lost to gypsum sludge moisture.

The precipitation extent was estimated by evaluating IAP/K_{sp} of the analytical data. The corresponding experimental saturation indices of the solids phases were specified (PHREEQC equilibrium phases) for the calcite precipitation reactor, the gypsum precipitation reactor and the SUF feed (see Table 4-2).

The model is thus an equilibrium model in which the approach to equilibrium was specified through the analytically determined saturation ratios of the solids phases. The model input data included saturation ratios achieved in solid liquid separation stages, SNF rejection ratios calculated from analytical data, operating pH of different process units, the calcium concentration target in the calcite reactor, the solid liquid separation performance and SNF concentrate purge rate (see Table 4-2 and Table 4-3)

The model predicted the cycled-up concentrations of dissolved solids (see Table 4-4) for all the process streams:

$$TDS_j = \sum_{i}^{nC} C_{ij} M_i - C_{CO_{2(g)}} M_{CO_{2(g)}} \quad (4\text{-}2)$$

The gaseous and dissolved $CO_{2(g)}$ component is subtracted from the sum of aqueous species as it is included in the total carbonic species component in the PHREEQC output. The electrical conductivity (EC) of a solution is related to the TDS through a parameter as shown in Equation (4-3). A value in the range of 0.5 to 0.9 is typically used however

the relationship is non-linear and subject to the nuances of TDS determination and EC measurement (Walton 1989). It has been recommended that each water sample be characterised individually (Crittenden, Harza et al. 2012).

$$TDS_j = K_j \kappa_{25°C} \tag{4-3}$$

The SNF unit was modelled using experimental rejection ratios and manipulating the sodium concentration in the permeate and concentrate streams to maintain charge balance. A secondary adjustment of the permeate and concentrate stream pHs were done to minimise the magnitude of sodium adjustment. The solute rejection ratio, system recovery and solute concentration in the permeate and concentrate streams are related through Equations (4-4) and (4-5) (Crittenden, Harza et al. 2012):

$$C_{Ci} = C_{Fi}\left[\frac{1-(1-r_i)R}{1-\mathrm{R}}\right] \tag{4-4}$$

$$C_{Pi} = \frac{C_{Fi}-(1-\mathrm{R})C_{Ci}}{R} \tag{4-5}$$

The process model algorithm converged the overall mass balance to a set of specified target process parameter by adjusting the, (1) CO_2 gas feed rate to target calcite reactor calcium hardness setpoint, (2) NaOH dosing rate to target calcite reactor pH setpoint, (3) H_2SO_4 dosing rate to target UF feed pH setpoint, (4) H_2SO_4 dosing rate to target NF feed pH setpoint, (5) $Ca(OH)_2$ dosing rate to target gypsum reactor pH setpoint, (6) NF concentrate purge flow rate to target recirculation liquor TDS setpoint, and (7) substituting the recycle stream (gypsum reactor discharge) to cycle up the ionic strength.

An inner convergence loop ensured that the setpoints, (1) to (6), were achieved to within a set tolerance, Equation (4-6) before substituting the recycle stream. An outer convergence loop targeted both a mass balance tolerance, Equation (4-7), and a tolerance between the targeted and calculated TDS of the recirculation liquor (SNF Feed).

$$\varepsilon_1 = \sum_{j}^{nC} \frac{PV_j - SP_j}{SP_j} < 10^{-4} \tag{4-6}$$

$$\varepsilon_2 = \sum_{k}^{nF} \left(TDS_j^k - TDS_j^{k-1} \right) < 10^{-1} \tag{4-7}$$

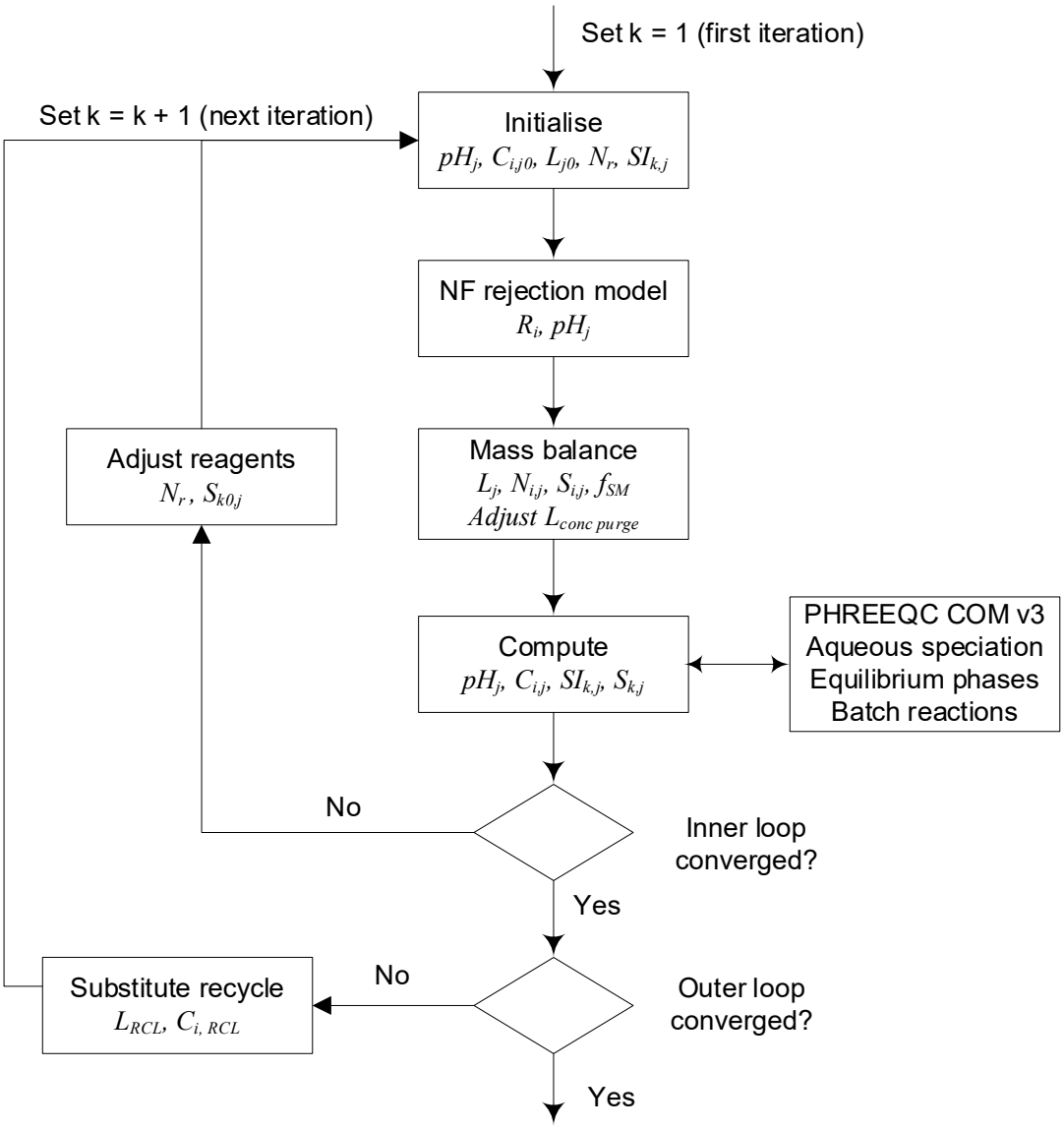

Figure 4-1 Simulation algorithm for process model with PHREEQC COM v3 interface and pitzer.dat

4.2 Process model calibration and results

The solver algorithm of the process model was setup to simulate the concentrate purge that would be necessary to sustain a cycled up concentration of the recirculation liquor for a specific set of operating parameters against a calibrated set of performance parameters. The set of operating and performance parameters used for the model calibration corresponds with the 297 hours in operation point and are listed in Table 4-1 and Table 4-2 respectively. Silica and nitrate are not included in the pitzer.dat database and were therefore not included the chemical system of the model (the latest version of pitzer.dat does in fact include Silica). It was assumed that the impact of nitrate was negligible for the higher ionic strength liquors within the ICD-SNF loop as the nitrate species did not cycle up due to a low to negative rejection of nitrate in the SNF. Silica did not cycle up either as it participated in the precipitation reactions and reported to the enstatite solids phase.

The flow diagram of the ICD-SNF experiment for the treatment of PRO concentrate is depicted in Figure 4-2. The PRO concentrate (0.98 m^3/h) reported to the calcite precipitation reactor where it was mixed with the output of the gypsum precipitation reactor and contacted with CO_2 gas. The output of the calcite precipitation reactor (2.47 m^3/h) was clarified and ultra-filtered before it was concentrated 2x in the SNF system, thus a 50% volumetric recovery. The SNF concentrate (1.01 m^3/h) was recycled to the gypsum precipitation reactor. SNF permeate (0.95 m^3/h) represents the product water recovered from PRO concentrate. Figure 4-2 also indicates the streams SRs and TDS values at the cycled-up state 297 hours into operation.

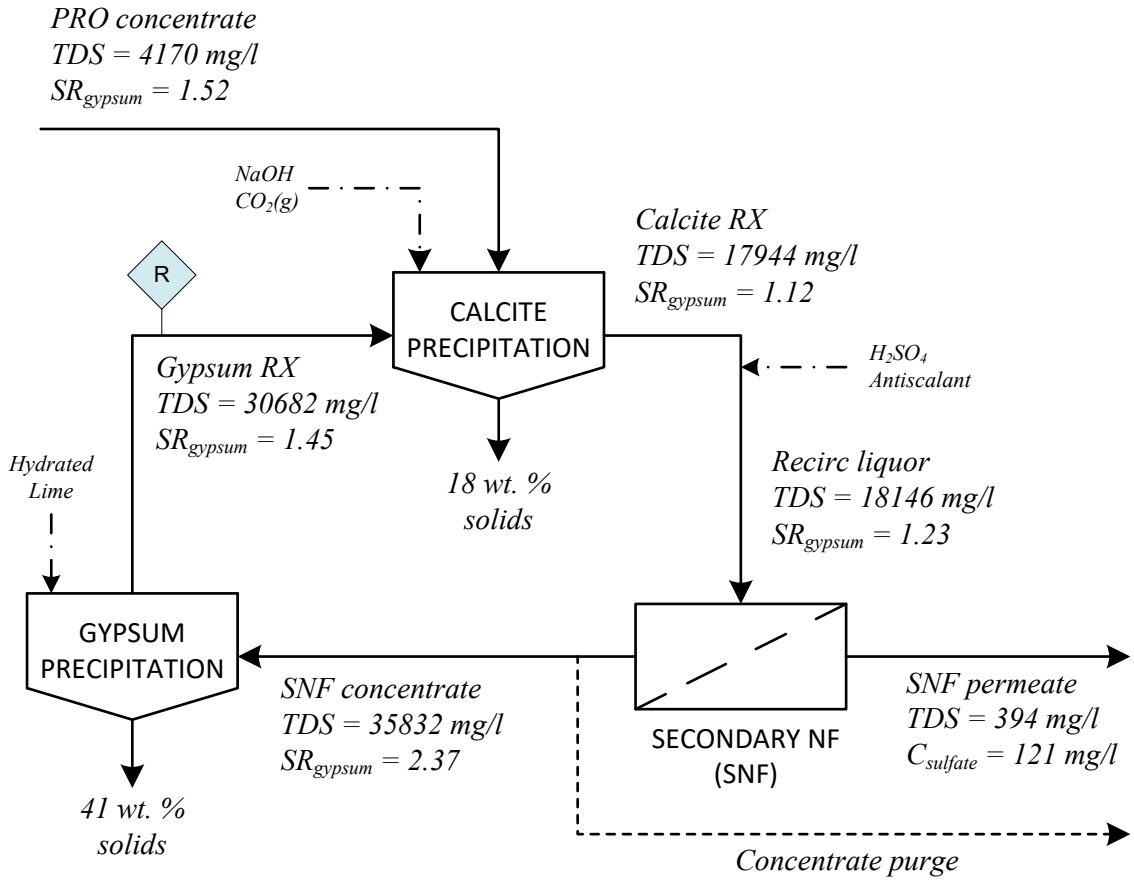

Figure 4-2 Pilot scale experimental setup of PRO concentrate feed to ICD-SNF with process model results calibrated at 297 hours in operation

Table 4-1 Operating parameters for model calibration

Operating parameters	Experimental / Analytical 297 hours	Process model input
Water temperature	29°C	29°C
Calcite reactor pH	10.7 / 11.3	10.7
Dissolved Ca in calcite reactor discharge	565	550
Calcite sludge dewatered solids content	18 wt. % average	18 wt. %
UF feed pH	7.0	7.0
UF volumetric recovery	82 %	82 %
TDS of the SNF feed	18148 (1) / 16750	18148

Operating parameters	Experimental / Analytical 297 hours	Process model input
SNF feed pH	4.8	5.5
Gypsum reactor pH	12.2 / 12.5	12.33
Carryover of gypsum reactor solids phase	1.1 – 12.4 wt. % (2)	10 wt. %
Gypsum sludge solids content	41 wt. % average	41 wt. %
(1) Converted from EC using average TDS / EC (2) Range of analytical TSS for gypsum reactor discharge		

The basis of the SNF feed TDS target was the EC value determined by the hand-held analyser at 297 hours and converted to TDS through the average TDS / EC value of 0.96.

Table 4-2 Performance parameters for model calibration

Performance parameters	Experimental & Analytical 297 hours	Process model input
Calcite reactor gypsum SR	1.12	1.12
Calcite reactor calcite SR	265	265
Gypsum reactor gypsum SR	1.45	1.45
Gypsum reactor calcite SR	220	220
SNF calcium rejection ratio	> 99.8	99.8
SNF chloride rejection ratio	~ 0	0.0
SNF Potassium rejection ratio	98.5	97.0
SNF Magnesium rejection ratio	> 98.1	99.0
SNF Sodium rejection ratio	96.5	96.9
SNF Sulphate rejection ratio	98.9	98.7
SNF Strontium rejection ratio	98.9	98.9

The process model and experimental results are compared at the cycled-up condition in Table 4-3 and Table 4-4. In Table 4-3, the chemical reagent consumption rates, SNF concentrate purge rate and volumetric recovery values are compared. In Table 4-4, the stream compositions of the process model and analytical analysis are compared.

Table 4-3 Comparison of experimental data and process model results

		Experimental & Analytical 297 hours	Process model output
SNF concentrate purge	%	0.0	1.18
Volumetric recovery of PRO concentrate	%	> 95	96.5
Hydrated lime consumption	kg/h	2.55	2.46
CO_2 (g) consumption	kg/h	0.83	0.90
15% NaOH consumption	kg/h	1.0	1.0

Table 4-4 Comparison of analytical results and model predictions at cycled up conditions

		Calcite reactor		Gypsum reactor		SNF feed		SNF concentrate		SNF permeate	
		Ana.	model	Ana.	model	Ana.	model	Ana.	model	Ana.	model
pH		11.4	10.7	12.5	12.3	4.8	5.5	4.6	4.95	5.3	6.5
TDS	$mg.L^{-1}$	17950	17944	29100	30682	16750	18146	32900	35832	686	394
Calcium	$mg.L^{-1}$	561	550	743	785	537	514	1050	1026	< 1	1.3
Magnesium	$mg.L^{-1}$	1.8	20.8	< 0.5	0.0	26.9	20.8	50.7	41.5	< 0.5	0.2
Sodium	$mg.L^{-1}$	5990	5037	10100	9467	5530	5037	9790	9956	194	154
Potassium	$mg.L^{-1}$	244	281	462	527	238	281	494	554	7.2	8.4
Chloride	$mg.L^{-1}$	12.1	31.2	< 0.1	31.2	12.4	31.2	< 0.1	31.2	33.6	31.2
Sulphate	$mg.L^{-1}$	15300	11656	22300	19539	13600	12100	24700	24079	146	121
Silica	$mg.L^{-1}$	1.1	N/A	7.7	N/A	13	N/A	14.0	N/A	11.7	N/A
Strontium	$mg.L^{-1}$	19	18.2	19	19.8	18	16.2	26.0	32.1	0.2	0.21
Nitrate-N	$mg.L^{-1}$	32.1	N/A	4.5	N/A	35.7	N/A	2.8	N/A	66.0	N/A

4.3 Discussion of process model calibration

The intent of the process model was to contextualise the observed experimental steady state in terms of the process parameters of Table 4-1 and the analytical results discussed in Chapter 4. The calibrated process model showed that a SNF concentrate purge of 1.2% would have been required to sustain the mass balance at the 297 hours in operation experimental point.

During the calibration of the process model, it was evident that the recirculation liquor EC was particularly sensitive to the target gypsum SR in the SNF feed. Lower gypsum SRs are achieved through greater reaction extent of the CO_2 induced calcite precipitation reaction. The speciation of CO_2 to carbonate (CO_3^{2-}) for calcite precipitation requires additional NaOH for pH control. The additional sodium input associates with sulphate and increases the dissolved species load in the recirculation liquor. This is due to the lower rejection of Na_2SO_4 in the SNF system.

The experimentally achieved gypsum SR, calculated by PHREEQC and pitzer.dat, in the SNF concentrate was 2.37 which is within the generally accepted scale formation suppression envelope for gypsum (< 2.5 – 4.0).

Greater dewatering and moisture recovery of the gypsum and calcite sludge streams will decrease the dissolved solids purge through the sludge moisture and thus increase the TDS of the recirculation liquor. Alternatively, the concentrate purge could be manipulated to control the recirculation liquor TDS at a setpoint target.

The TDS calculated by the process model in the SNF permeate was 394 $mg.L^{-1}$ with sodium and sulphate concentrations of 154 $mg.L^{-1}$ and 121 $mg.L^{-1}$, respectively. The TDS is lower than the analytically determined TDS as the omission of nitrate in the process model creates a substantial deviation in the SNF permeate.

The World Health Organisation (WHO) does not propose a health based guideline value for sulphate or sodium in drinking water, however, it states the lower taste threshold at 200 and 250 $mg.L^{-1}$ for sodium and sulphate, respectively (World Health Organization 2003, World Health Organization 2004). The analytical results and model prediction of the SNF permeate is within the taste threshold for sodium and sulphate as stated by the WHO. In this specific case, secondary treatment of the SNF permeate would have to

include denitrification through either ion exchange or biological means. Biological denitrification, although more difficult to implement and operate, should be preferred due to the completion between sulphate and nitrate in strong base anion exchangers.

The calibrated process model showed that 96.5% of the PRO concentrate volume was recovered as SNF permeate. The mass distributions of sulphate and sodium in the PRO concentrate, as calculated by the process model, reported to the different ICD-SNF discharge streams at weight percentages of the total as shown in Figure 4-3.

Sulphate reported to the sludge solids, sludge moisture, SNF permeate and SNF concentrate purge streams at 83.8, 6.5, 2.9 and 6.8 wt.% respectively. Similarly, the amounts of sodium were 0.0, 31.6, 38.7 and 29.7 wt.% respectively.

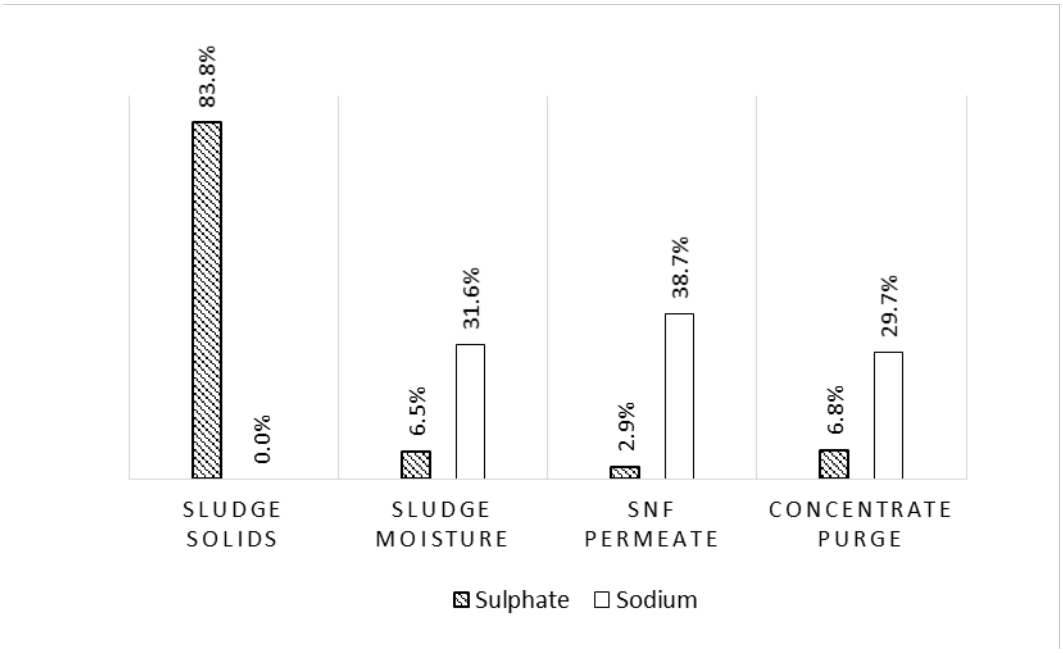

Figure 4-3 Sodium and sulphate discharge mass distribution as percentages

4.4 Conclusion

The process model developed in this study can report aqueous and solids phase concentrations as a function of operating parameters for corresponding performance parameters. The interpretation of experimental data, especially in complex ICD-SNF processes with recycle of SNF concentrate, requires such rigour for process design. For example, the experimental data indicated total recycle is possible whereas the process model showed that a substantial 1.2% SNF concentrate purge would be required to sustain the steady state that was achieved.

One limitation of the process model is the limited ability to predict performance as the ICD sub model is equilibrium based and calibrated to the experimentally achieved approach to equilibrium. A further limitation is the specification of experimental rejection ratios instead of a SNF transport model that can predict NF transport as a function of hydraulic and membrane properties It is recommended that a rate-based ICD model be developed to address the former limitation. A NF transport model was developed to address the latter limitation and is presented in Chapter 5.

5 ESTIMATION OF NF SOLUTE REJECTION IN RO CONCENTRATE TREATMENT

This chapter is a paper submitted to WISA 2018 and a condensed version was submitted to ICARD 2018. A copy of the version published by ICARD is available in Appendix D. The paper was presented at the WISA 2018 conference on the 25th of June 2018.

Franzsen, S., Bonner, R., Naidu, J., Sheridan, C., Simate, G.S. (2018). "Estimation of nanofiltration solute rejection in reverse osmosis concentrate treatment processes."

My contribution included the programming of the DSPM & DE with ENP model in Python, the sensitivity analysis and data generation as well as writing the narrative and submission to WISA 2018. Ricky Bonner and Jivesh Naidu were acknowledged as co-authors for contribution in technical discussions.

5.1 Abstract

A nanofiltration (NF) model was built in the programming language Python and interfaced with geochemical calculation software PHREEQC COM v3 for the prediction of NF rejection performance in the treatment of reverse osmosis (RO) concentrate. The fundamental differences between this work and other Extended Nernst Planck with Donnan steric pore model and dielectric exclusion (DSPM & DE) studies were the arrangement of the ions into cation-anion ion pairs with a representative dominant ion, the assignment of feed-membrane and membrane-permeate Donnan potentials, $\Delta\varphi_{D,m}$ and $\Delta\varphi_{D,p}$, as input values and the omission of the charge offset $-C_X$. The model was fitted to NF rejection performance data from MDS NF 4040T and MDS NF 8040 elements operating in a pilot scale high recovery recycle process and a full scale single pass process respectively, at a water treatment plant in Ghana. The results showed that the built NF model can match the rejection performance of the MDS elements in the two processes with resulting $\Delta\varphi_{D,m}$ and $\Delta\varphi_{D,p}$ values and membrane pore dielectric constant, ε_{pore}, that are within the expected ranges for Polyamide membrane active layers. The inclusion of the uncharged specie SiO_2 was done to regress pore-radii and active layer thickness in the absence of electrostatic effects. It was recommended that the NF model is fitted to additional operational data and the fitted parameters, $\Delta\varphi_{D,m}$, $\Delta\varphi_{D,p}$ and ε_{pore},

compared to fitted parameters of a conventional ENP with DSPM & DE model to better understand the limitations and advantages of the ion pairing with dominant ion feature of the built NF model. The built NF model was considered to have three industrial applications – (1) tracking in service element degradation in terms of increasing pore radius, decreasing effective active layer thickness and decreasing feed-membrane $\Delta\varphi_{D,m}$, (2) element selection in the design of RO concentrate treatment processes and (3) estimation of unknown solute permeability values by considering the likely ion-pairs and dominant ions that characterises a given aqueous solution.

Keywords: Mine water treatment, brine treatment, nanofiltration modelling

* Corresponding author. Tel: +27 11 656 3936; Fax: +27 11 656 3965

Email address: sebastianf@miwatek.co.za

5.2 Introduction

Reverse osmosis (RO) and nanofiltration (NF) account for 55% of the total worldwide water produced from desalination activities and 87% of water reclaimed from brackish water resources (Antony, Low et al. 2011). RO and NF concentrate disposal include surface water discharge, deep well injection, land application, and evaporation in ponds or thermal processes with subsequent solids disposal. However, concentrate disposal using the stated options is very costly. The minimisation of concentrate results in lower disposal costs and drives the development of higher recovery processes (Subramani and Jacangelo 2014, Randall and Nathoo 2015). Research studies have shown that intermediate chemical demineralisation (CD) of primary RO concentrate followed by secondary RO desalination can substantially improve the volumetric recovery of brackish feed waters (Gabelich, Williams et al. 2007, Rahardianto, Gao et al. 2007, Rahardianto, McCool et al. 2010, Greenlee, Testa et al. 2011, McCool, Rahardianto et al. 2013).

In mine water treatment, the application of ICD with primary and secondary RO or NF has an impact on the site wide water balance and quality. At a mine water treatment plant (MWTP) in Ghana (Name of corporation intentionally omitted), a high recovery RO-CD-NF with recycle to CD process (RO-CD-NF-RCY) was piloted and a full-scale RO-NF-CD process is currently in operation. In both cases, the NF functioned as a concentrator for Ca^{2+} and SO_4^{2-} for improved $CaSO_4.2H_2O$ precipitation kinetics and a passage for Cl^-

, NO_3^-, Na^+ and K^+ to secondary treatment and subsequent discharge from the site wide water balance. In the high recovery RO-CD-NF-RCY process, the SO_4 rejection in the NF dictated the operating pressure and the magnitude of the concentrate bleed.

Modelling of the NF, NF element selection and the process operating envelope of the NF are critical aspects of design to achieve the process intent. Different NF elements show substantial performance variation for systems with slight variation. Performance characterisation generally consists of pure water permeability and rejection measurements of charged and uncharged solutes (Artuğ 2007). In phenomenological models such as the Spiegler-Kedem variation of the solution diffusion model or the two parameter (A and B-values) simplified solution diffusion model, a linear relationship between driving force and flux near thermodynamic equilibrium is expressed as a phenomenological constant into which solute-membrane interactions are attributed (Artuğ 2007, Nir and Lahav 2013). Phenomenological models and the typical application of single salt (e.g. NaCl, Na_2SO_4, $CaSO_4$, $MgSO_4$ etc.) rejection data are considered inappropriate for NF modelling or NF element selection due to the inability to relate the membrane characteristics to the membrane-solution partitioning, electrostatic effects and convection transport observed in NF membranes. Studies in partitioning of the ions at the feed-membrane and membrane-permeate interface led to the development of the Donnan steric pore model & dielectric exclusion (DSPM&DE) model. The DSPM&DE model considers the membrane as having effective pore radius, effective active layer thickness, effective membrane charge density and membrane dielectric constant and is capable of describing the asymptotic concentration gradient at the membrane-solution interfaces (Artuğ 2007, Geraldes and Brites Alves 2008).

The Pitzer aqueous speciation model (pitzer.dat) supplied with PHREEQC can accurately predict thermodynamic properties at high ionic strength for solutions with compositions substantially different from that of seawater (Pitzer 1981, Harvie, Møller et al. 1984, Appelo 2015). The complete geochemical simulation capabilities of PHREEQC are accessible to different software environments (e.g. Python) through classes implemented in the IPhreeqc modules (Charlton and Parkhurst 2011)

The intent of this paper was to present an alternative DSPM & DE model in which (1) Pitzer activity and osmotic coefficients were determined by coupling PHREEQC COM

to the solver algorithm, (2) aqueous solutions were expressed as cation-anion ion pairs with a selected dominant ion for transport and partition modelling, (3) CO_2 and SiO_2 were included as aqueous components for carbonic speciation and an uncharged specie for regression in the absence of electrostatic effects respectively.

5.3 Methods

The aqueous system included H-Na-K-Ca-Mg-OH-HCO_3-Cl-SO_4-SiO_2-CO_2 and was arranged into Na_2SO_4, NaCl, $NaHCO_3$, NaOH, K_2SO_4, KCl, $KHCO_3$, KOH, $CaCl_2$, $CaSO_4$, $Ca(HCO_3)_2$, $Ca(OH)_2$, $MgCl_2$, $MgSO_4$, $Mg(HCO_3)_2$, $Mg(OH)_2$, HCl, H_2SO_4, CO_2 and SiO_2 ion pairs and molecules. The distribution of ions into ion pairs and the selection of a dominant ion represented an additional regression parameter.

The model domain comprised ten nodes j along the element string feed channel and three distinct regions of solute mass transport at each node presented in Figure 5-1. The solute transport path and mechanisms through the membrane included (1) development of a concentration polarisation boundary layer approaching the feed-membrane interface, (2) feed-membrane interface partitioning occured through steric, Donnan potential and dielectric exclusion, (3) active layer transport and (4) membrane-permeate interface partitioning occured through steric, Donnan potential and dielectric exclusion.

The active layer transport was reduced to the transport between the two inside membrane concentrations determined by the partitioning equations at the feed-membrane and membrane-permeate interfaces. The effective charge density term was omitted and the Donnan potential at the feed-membrane and membrane-permeate interfaces were made input parameters. It was assumed that the feed-membrane interface partitioning due to steric, Donnan and dielectric exclusion effects, dominated for the solutions studied and thus the approximation of the active layer as two points determined from feed-membrane and membrane-permeate partitioning was sufficiently accurate.

Concentration polarisation and hydraulic effects were considered as the model was setup to represent one element string of the actual array. For the full-scale RO-NF-CD process, a 4.3 Ml/d facility commissioned in September 2017, the NF system is an array of multiple 5x element strings of 8” MDS NF 8040 elements. For the high recovery RO-

CD-NF-RCY process, the model is the same as the actual element string that comprised of 8x MDS NF 4040T elements.

A sensitivity analysis was performed to illustrate the effects of Donnan partitioning, Born solvation, pore radii and active layer thickness at the respective hydraulic conditions that develop for a range of system recoveries and the solution chemistry in each case. The membrane dielectric constant was determined from fitting the NF model to the rejection data of the MDS NF 8040 and the same dielectric constant was used for the MDS NF 4040T models as it is considered a membrane specific parameter and the elements are of the same type.

The MDS NF 8040 element is a modified Desal DS-5 DK element which is a thin film membrane with an active layer of Polyamide and a support layer of Polysulfone material.

5.3.1 Solute mass transfer in the boundary layer

Equation (5-1) is the combination of the Mariñas and Urama mass transfer correlation and a correction factor ϵ for the suction effect generated by permeation through the membrane (Geraldes and Brites Alves 2008, Crittenden, Harza et al. 2012). The correlation includes a factor κ for the hydraulic impact of different feed spacers and channel heights and ranges from 0.4 to 0.54 for different elements (Crittenden, Harza et al. 2012). In this study the κ was set at 0.54. ϵ is described by semi empirical correlation shown in Equation (5-2) (Geraldes and Brites Alves 2008). The concentration layer forms due to the rejection of solutes by the membrane and impacts the process due to higher osmotic pressure gradient, lower solute rejection and saturation ratio of sparingly soluble minerals that can cause fouling (Crittenden, Harza et al. 2012).

$$k_{CPi,j} = k_{i,j}\epsilon_{i,j} = \kappa\frac{D_L}{d_H}\left(Re_j\right)^{0.5}\left(Sc_{i,j}\right)^{0.33}.\epsilon_{i,j} \quad (5\text{-}1)$$

$$\epsilon = \emptyset_i + \left(1 + 0.26{\emptyset_i}^{1.4}\right)^{-1.7} \text{ where } \emptyset_i = \frac{J_{w,j}}{k_{c,i}} \quad (5\text{-}2)$$

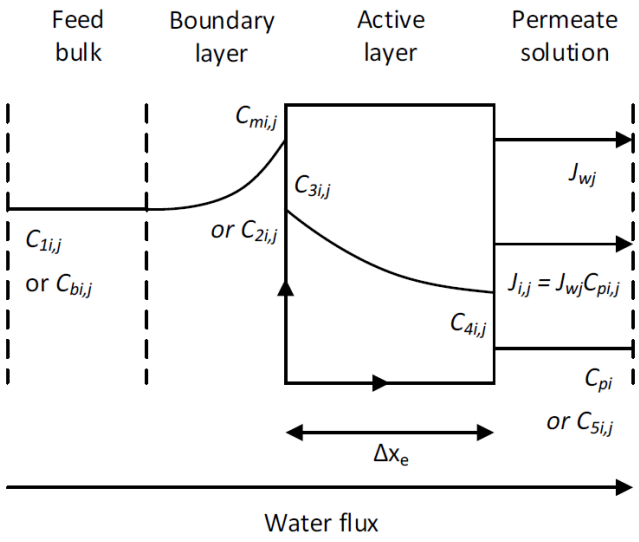

Figure 5-1: Schematic diagram of the solute concentration profile for each node j

5.3.2 Partitioning at feed-membrane and membrane-permeate interfaces

The partitioning at the feed-membrane and membrane-permeate interface is described in Equation (5-3) as a function of three transport resistances – (1) Steric partitioning, (2) Donnan potential effect and (3) dielectric exclusion (Artuğ 2007). This method is referred to in literature as the Donnan steric pore model and dielectric exclusion (DPSM & DE). Steric partitioning θ_i expressed in Equation (5-4), refers to the transport hindrance as a function of solute radii and pore-radii within well-defined cylindrical pores (Labban, Liu et al. 2017). Donnan potential develops at the feed-membrane interface and at the membrane permeate interface, $\Delta\varphi_{D,M}$ and $\Delta\varphi_{D,p}$ respectively, to maintain charge balance. The effect of the Donnan potential promotes the transport of counter-ions and hinders the transport of co-ions (Peeters, Boom et al. 1998). Dielectric exclusion refers to the reduction in solvation capacity of the pore fluid due to the hydraulics in the confined space of the pores. This barrier to ionic species entering the active layer is referred to as the Born solvation energy barrier ΔW_I and is shown in Equation (5-5) (Bowen and Welfoot 2002).

In this study, a dominant ion was attributed to the defined cation-anion ion pairs and was either the cation or the anion of a cation-anion pair. The steric hindrance, Donnan

potential and Born solvation electrostatic effects of the ion pair was determined from the properties of the dominant ion attributed to the ion pair.

The activity coefficients were determined using the Pitzer model included in PHREEQC. The membrane pore dielectric constant was regressed to 39.5 using the NF rejection data from the RO-NF-CD process. The same membrane dielectric constant was used for the RO-CD-NF-RCY process as the MDS NF 8040 and MDS NF 4040T elements are of the same type. The feed-membrane and membrane-permeate Donnan potentials were made input parameters.

$$\frac{\gamma_{3i}c_{3i}}{\gamma_{2i}c_{2i}} = \theta_i . \exp\left(-\frac{z_i F}{R_g T} . \Delta\varphi_D\right) . \exp\left(-\frac{\Delta W_{i,Born}}{k_B . T}\right) \quad (5\text{-}3)$$

$$\theta_i = \left(1 - \frac{r_{si}}{r_p}\right)^2 = (1 - \lambda_i)^2 \quad (5\text{-}4)$$

$$\Delta W_{i,Born} = \frac{z_i^2 . e^2}{8\pi\varepsilon_0 r_{si}} . \left(\frac{1}{\varepsilon_p} - \frac{1}{\varepsilon_b}\right) \quad (5\text{-}5)$$

5.3.3 Solute mass transfer in the active layer

Equation (5-6) represents the solute flux through the membrane using the ENP equation which includes terms for diffusion, electromigration and convection transport (Peeters, Boom et al. 1998, Artuğ 2007). Hindrance factors must be applied to the diffusion and convection terms for transport in the active layer. Correlations for the factors as a function of solute to pore radius that are appropriate for NF pore geometry are available (Artuğ 2007).

$$J_{i,j}^{ENP} = -K_{id} D_i \frac{dc_i}{dx} - \frac{z_i c_{i,j} D_{pi}}{R_g T} F \frac{d\varphi}{dx} + K_{ic} c_{i,j} V \quad (5\text{-}6)$$

In this study the active layer transport was reduced to the linear transport between the two inside membrane interfacial concentrations c3 and c4 – refer to Figure 5-1. To evaluate the $d\varphi/dx$ term, the cation-anion ion pairs were speciated out to individual ions using PHREEQC. Initial estimates of the concentration polarisation layer and permeate concentrations, c2 and c5 respectively, are determined through Equations (5-7) to (5-11).

5.3.4 Solution algorithm for NF model

The solution algorithm was programmed in Python and linked to the COM module of PHREEQC to automate the iteration through steps 1 to 4. The aqueous speciation and batch reaction capabilities of PHREEQC were used to determine the Pitzer activity coefficients, osmotic coefficients and to speciate the ion pairs into individual ions.

Step 1 was to separate the feed solution into cation-anion ion pairs, specify the element properties, model parameters, process inputs and regression parameters. The parameters specific to each of the ion pairs and the individual ions were calculated – stokes radius, stokes radius to membrane pore radius, convection hindrance factor, diffusion hindrance factor and Born solvation energy barrier.

Step 2 was to estimate the hydraulic parameters, water flux, solute flux and outside membrane concentrations (c_1, c_2 and c_5) to enable the evaluation of the ENP and partitioning equations (Equations (5-3) and (5-6) respectively). Equation (5-7) was the solute flux at each stage j expressed in terms of a phenomenological constant that was generalised for each of the cation-anion ion pairs. Equation (5-8) was the membrane water flux equation with the membrane specific water permeability constant A.

$$J_{i,j} = B_i\left(\beta_{i,j}c_{bi,j} - c_{pi,j}\right) \tag{5-7}$$

$$J_{w,j} = A\left[\left(P_{b,j} - P_p\right) - \left(\pi_{m,j} - \pi_{p,j}\right)\right] \tag{5-8}$$

The concentration polarisation at each node, expressed in terms of water flux, mass transfer coefficient and rejection and generalised for each specie, is shown in Equation (5-9) (Crittenden, Harza et al. 2012). Equation (5-10) is the definition of the solute flux generalised for each specie and the permeate concentration substituted with the equivalent in terms of solute rejection and feed bulk concentration (Crittenden, Harza et al. 2012).

$$\beta_{i,j} = e^{J_{w,j}/k_{cpi,j}}.\, r_{i,j} + \left(1 - r_{i,j}\right) \tag{5-9}$$

$$J_{i,j} = J_{w,j}c_{pi,j} = J_{w,j}(1 - r_i)c_{bi,j} \tag{5-10}$$

Setting Equation (5-10) equal to Equation (5-7) and substituting Equation (5-9) leads to an equation that relates the solute rejection, solute permeability constant, concentration polarisation mass transfer coefficient and the water flux – Equation (5-11):

$$r_{i,j} = \left[B_i e^{J_w/k_{cpi,j}} + J_{w,j}\right]^{-1} . J_{w,j} \quad (5\text{-}11)$$

The solver iterated through the nodes several times and utilises the Newton method from the Scipy.Optimize package to solve for the water flux at each node that satisfies the solute rejections from Equation (5-11) at the specified feed pressure. The iteration strategy was used to incorporate the Pitzer osmotic coefficients determined by PHREEQC for stage water flux determinations.

Step 3 was to evaluate the c_3 and c_4 using Equation (5-3). The $d\varphi/dx$ term must be determined to calculate the solute flux according to the ENP Equation (5-6). PHREEQC was used to speciate out the ion pair concentrations to individual ion concentrations at c_3 and c_4 to determine $d\varphi/dx$. The ratio of the solute flux determined by the ENP Equation (5-9) and the solute permeability constant in Equation (5-7) were used to adjust the solute permeability constant of each cation-anion ion pair. The solute permeability constant for the next solver iteration was determined by using Equation (5-12)

$$B_{i,j} = J_{i,j}^{ENP} . \left[\beta_{i,j} c_{bi,j} - c_{pi,j}\right]^{-1} \text{ and } B_i = \overline{B}_{i,j} \quad (5\text{-}12)$$

Step 4 checked the convergence criteria and returned the solver to step 2 until it was achieved. The final cation-anion ion pairs were speciated out in PHREEQC and the overall rejection of individual ions reported. In addition to minimising the error between the solute flux determined by the ENP equation and the phenomenological constant, the solver can also target a system volumetric recovery and determine the corresponding feed pressure.

The input parameters for the model calibration case are presented in Table 5-1 and the results of the parameter regression presented in Table 5-2.

Table 5-1 Model input parameters for calibration case

Model input parameters	Unit	RO-NF-CD	RO-CD-NF-RCY
Element		MDS NF 8040	MDS NF 4040T
Design volumetric recovery	%	50	50
Membrane surface area	m^2	33.1	7.3
Feed pressure	kPag	1065	1750
Operating temperature	°C	30	30
Feed flow rate	m^3/h	5.1	1.9
Elements per string		5	8
Nodes per element string		10	10
Feed spacer thickness	Mil	31	31

Table 5-2 Results of the parameter regression

Calibration case regression results	Unit	RO-NF-CD	RO-CD-NF w/ recycle
Element		MDS NF 8040	MDS NF 4040T
Pore radius	nm	0.57	0.535
Active layer thickness	μm	0.3	0.3
Membrane dielectric constant		39.5	39.5
Water permeability constant	$ms^{-1}bar^{-1}$	5.28E-07	7.5E-07
Feed-membrane potential	mV	- 30	- 4.5
Membrane-permeate potential	mV	+ 20	+ 0.5

The solution algorithm described in this section is graphically presented in Figure 5-2.

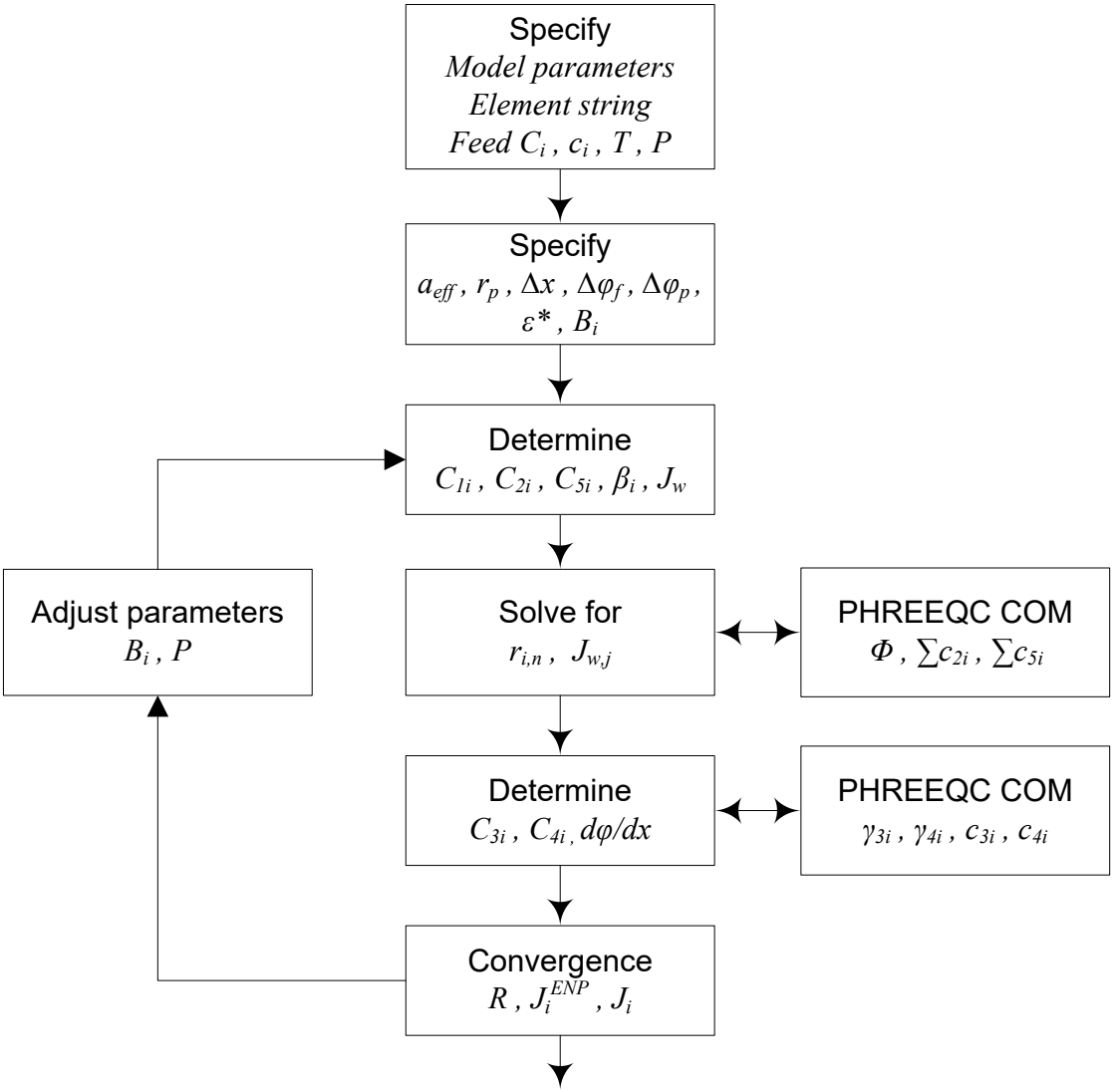

Figure 5-2 Simulation algorithm for alternative DSPM & DE NF model

5.4 Results and Discussion

The NF model was fitted to operational data from the RO-NF-CD full scale process and the RO-CD-NF-RCY pilot process to determine the installed element pore radius, effective active layer thickness, membrane-interface Donnan potentials and feed/permeate pH values. The results are shown in Table 5-3 and the comparison of rejection performance between the model and the analytical results are shown in Table 5-4. The regression of the pore radius and effective active layer thickness was constrained to yield close agreement with rejection of uncharged species SiO_2. This technique is

useful as the rejection of SiO_2 is not subject to the electrostatic effects at the system pH. The feed-membrane and membrane-permeate Donnan potentials were then regressed in the range 0 to -30 mV and 0 to +20 mV respectively to minimise the error between the model predicted and analytically determined rejection ratios.

Table 5-3 Results from fitting operational data from RO-NF-CD full scale process and RO-CD-NF-RCY pilot process

Process	Data	r_{pore}	Δx_e	$\Delta\phi_{D,m}$	$\Delta\phi_{D,p}$	ε_{pore}	Feed pH	Perm pH
		nm	µm	mV	mV		-	
RO-NF-CD FULL SCALE	Model	0.570	0.3	- 30	+ 20	39.5	7.7	7.6
	SGS						7.9	7.7
RO-CD-NF-RCY PILOT	Model	0.535	0.3	- 4.5	+ 0.5	39.5	5.9	5.7
	SGS						5.9	5.7

Table 5-4 Comparison of ion rejections determined by the model and the analytical results from SGS

Process	Data	Na	K	SO_4	Ca	Mg	HCO_3	Cl	SiO_2
		rej%	rej%	rej%	rej%	rej%	rej%	rej%	rej%
RO-NF-CD FULL SCALE	Model	25.1	25.1	99.4	82.7	94.1	26.0	3.1	6.1
	SGS	21.0	23.5	99.6	86.7	94.4		0.3	5.9
RO-CD-NF-RCY PILOT	Model	96.4	96.4	99.2	99.2	99.3	20.5	0.0	11.7
	SGS	96.4	96.8	99.1	99.6	99.1		< 0	13.5

The dominant ion that was assigned to each of the ion pairs followed a set of rules that are applicable to elements that are expected to develop a negative feed-membrane Donnan potential – (1) pairs with divalent anion had the anion as dominant as the repulsion from the feed-membrane interface appeared dominant, (2) pairs with monovalent anion and cation had the cation as dominant as the attraction to the feed-membrane interface appeared dominant, (3) pairs with divalent cation and monovalent anion had the divalent

cation as dominant as the attraction to the feed-membrane interface appeared dominant and (4) pairs with divalent cation and divalent anion had the divalent anion as dominant as the repulsion from the feed-membrane interface appeared dominant.

The fractional contribution of cation-anion ion pairs to the corresponding individual cations were also regressed. Eighteen cation-anion ion pairs (Na_2SO_4, NaCl, $NaHCO_3$, NaOH, K_2SO_4, KCl, $KHCO_3$, KOH, $CaCl_2$, $CaSO_4$, $Ca(HCO_3)_2$, $Ca(OH)_2$, $MgCl_2$, $MgSO_4$, $Mg(HCO_3)_2$, $Mg(OH)_2$, HCl, H_2SO_4) with a corresponding nine mole balances (H-Na-K-Ca-Mg-OH-HCO_3-Cl-SO_4) resulted in an under specified system with multiple solutions. The solutions were however $CaSO_4$ and Na_2SO_4 dominated for the RO-NF-CD and RO-CD-NF-RCY processes respectively and the resulting distribution followed a pattern that should be evaluated against additional operational data. The observed patterns are shown in Table 5-5.

Table 5-5 Cation-anion distributions for the $CaSO_4$ and Na_2SO_4 dominated solutions

	$CaSO_4$ dominated solution from RO-NF-CD Process				Na_2SO_4 dominated solution from RO-CD-NF-RCY Process			
	Na	K	Ca	Mg	Na	K	Ca	Mg
Na_2SO_4	25.3				97.1			
NaCl	66				2.6			
$NaHCO_3$	8.7				0.3			
NaOH	0				0			
K_2SO_4		25.3				97.1		
KCl		66				2.6		
$KHCO_3$		8.7				0.3		
KOH		0				0		
$CaCl_2$			2.6				0	
$CaSO_4$			79.9				97.1	
$Ca(HCO_3)_2$			17.4				2.9	
$Ca(OH)_2$			0				0	
$MgCl_2$				0				0
$MgSO_4$				82.6				97.1
$Mg(HCO_3)_2$				17.4				2.9
$Mg(OH)_2$				0				0

The effect of pore radius and effective active layer thickness on rejection performance of the MDS NF 8040 elements in the RO-NF-CD process is shown in Figure 5-3 and Figure 5-4. The corresponding data is tabulated in appendices C1-1 and C1-2 for the calibrated case, C2-1 and C2-2 for the smaller pore radius case, C3-1 and C3-2 for the larger pore radius case, C4-1 and C4-2 for the smaller active layer thickness case and C5-1 and C5-2 for the larger active layer thickness case. Appendices Cx-1 contains hydraulic and rejection data and appendices Cx-2 shows node flux, feed pressure and pressure drop data.

The water flux at the model fitted datapoint is 15.4 LMH. Figure 5-3 and Figure 5-4 also illustrates the effect of system volumetric recovery (10% to 60% in 10% intervals) expressed in terms of permeate flux rate in LMH. The rejection of all solutes increases with a decrease in pore radius and is attributed to the enhanced steric hindrance at the feed-membrane interface. SO_4 is not substantially affected as the feed-membrane Donnan potential dominates the steric hindrance effect however, the reduction in SO_4 rejection for the 0.2 μm effective active layer thickness at 15.4 LMH is interesting in terms of element selection for lower sulphate rejection in recycle based concentrate treatment processes. The cation is the dominant ion in ion pairs that contains HCO_3. For HCO_3, the steric hindrance effect is overwhelmed by the attraction of the feed-membrane Donnan potential as illustrated in Figure 5-4. The uncharged specie SiO_2 is the only specie that responds to the change in pore radius and effective active layer thickness in the absence of electrostatic effects.

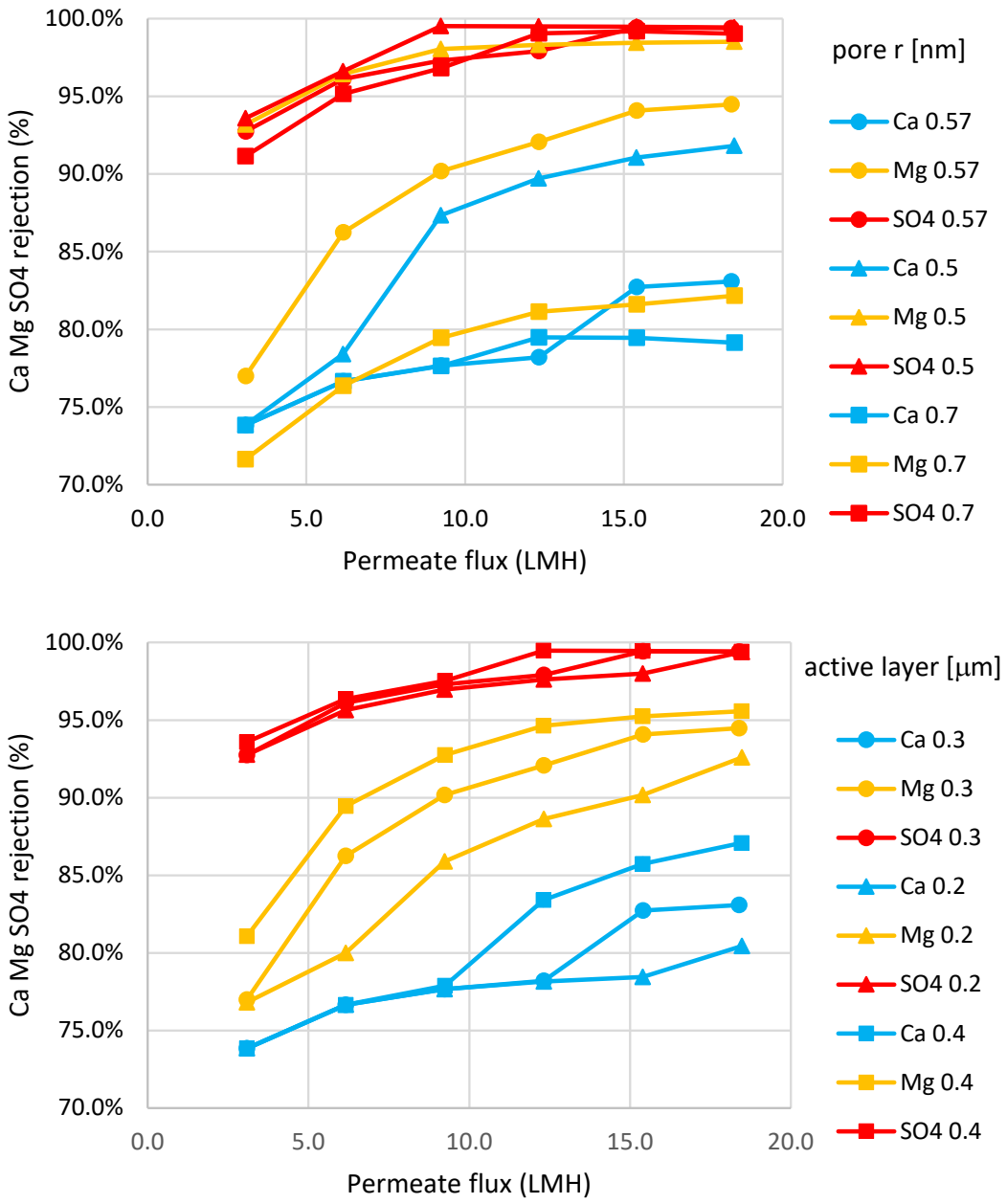

Figure 5-3 The effect of pore radius and effective active layer thickness on the Ca, Mg and SO_4 rejection performance of the MDS NF 8040 elements in the RO-NF-CD process

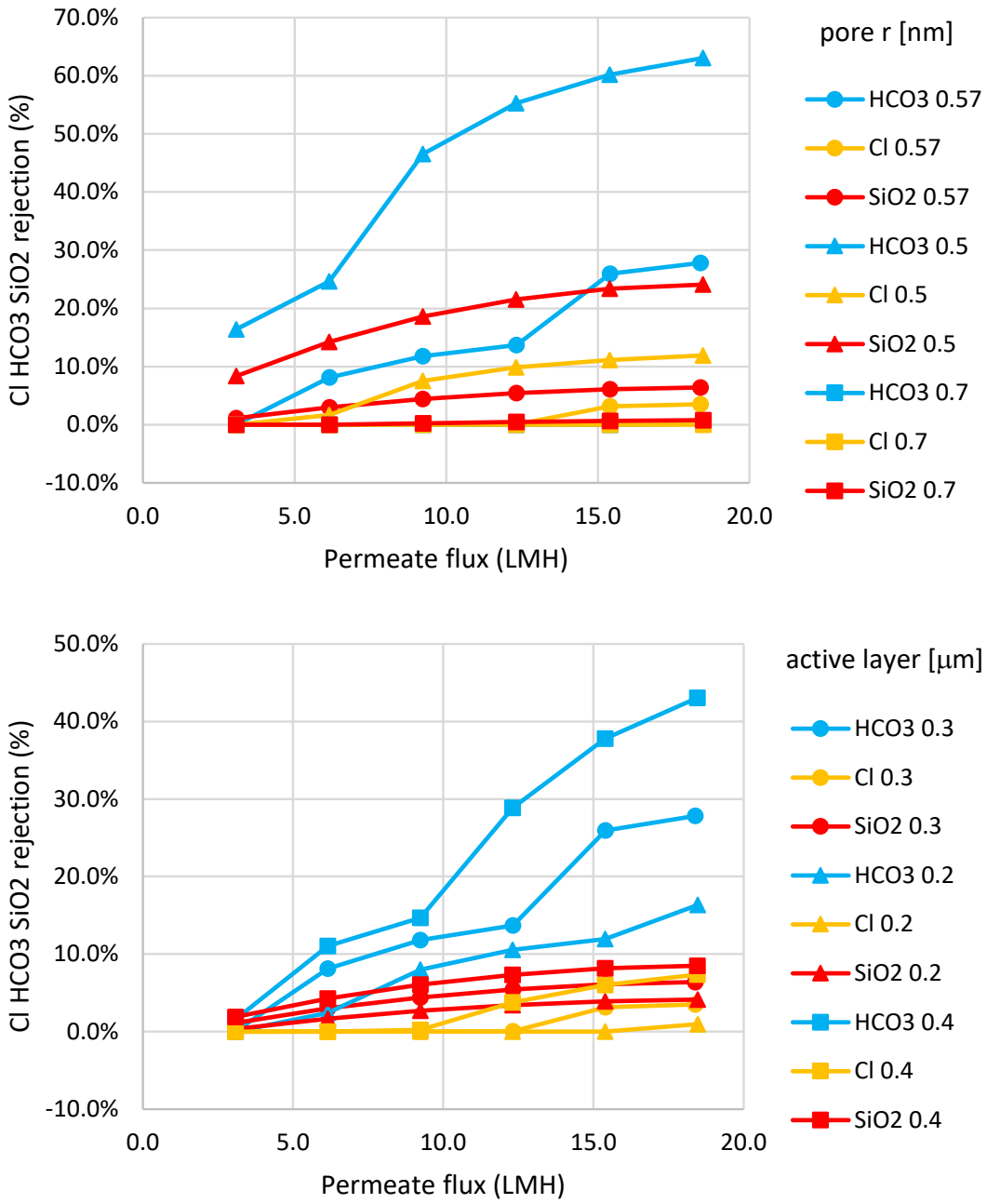

Figure 5-4 The effect of pore radius and effective active layer thickness on the HCO_3, Cl and SiO_2 rejection performance of the MDS NF 8040 elements in the RO-NF-CD process

The effect of membrane pore dielectric constant ε_{pore} and feed-membrane Donnan potentials $\Delta\varphi_{D,m}$ on rejection performance of the MDS NF 8040 elements in the RO-NF-CD process are shown in Figure 5-5 and Figure 5-6. The corresponding data is tabulated in appendices C1-1 and C1-2 for the calibrated case, C6-1 / C6-2 and C7-1 / C7-2 for the smaller and larger membrane pore dielectric constants, C8-1 / C8-2 and C9-1 / C9-2 for the decreasing negative feed-membrane Donnan potentials.

Reducing ε_{pore} increases the Born solvation energy barrier ΔW_I at the feed-membrane interface and hence the rejection performance of all charged species was improved. The uncharged specie SiO_2 was not affected by changes in $\Delta\varphi_{D,M}$ or ε_{pore}. Increasing the negative $\Delta\varphi_{D,M}$ increased the repulsion of co-ions and the attraction of counter-ions. For higher negative $\Delta\varphi_{D,M}$, SO_4 rejection increased due to co-ion repulsion, Ca and Mg rejection decreased due to counter-ion attraction, HCO_3 and Cl rejection decreased due to counter-ion attraction (dominant ions are cations for monovalent anions).

The lower solute rejections reported in Figure 5-3 to Figure 5-6 corresponds with higher pore radii, lower effective active layer thickness and lower negative feed-membrane $\Delta\varphi_{D,M}$ in the case of SO_4. It is thought that irreversible membrane damage caused by fouling, scaling and exposure to cleaning chemicals can be described by the deterioration in these properties. These observations have been made before by other researchers (Kosutic and Kunst 2002).

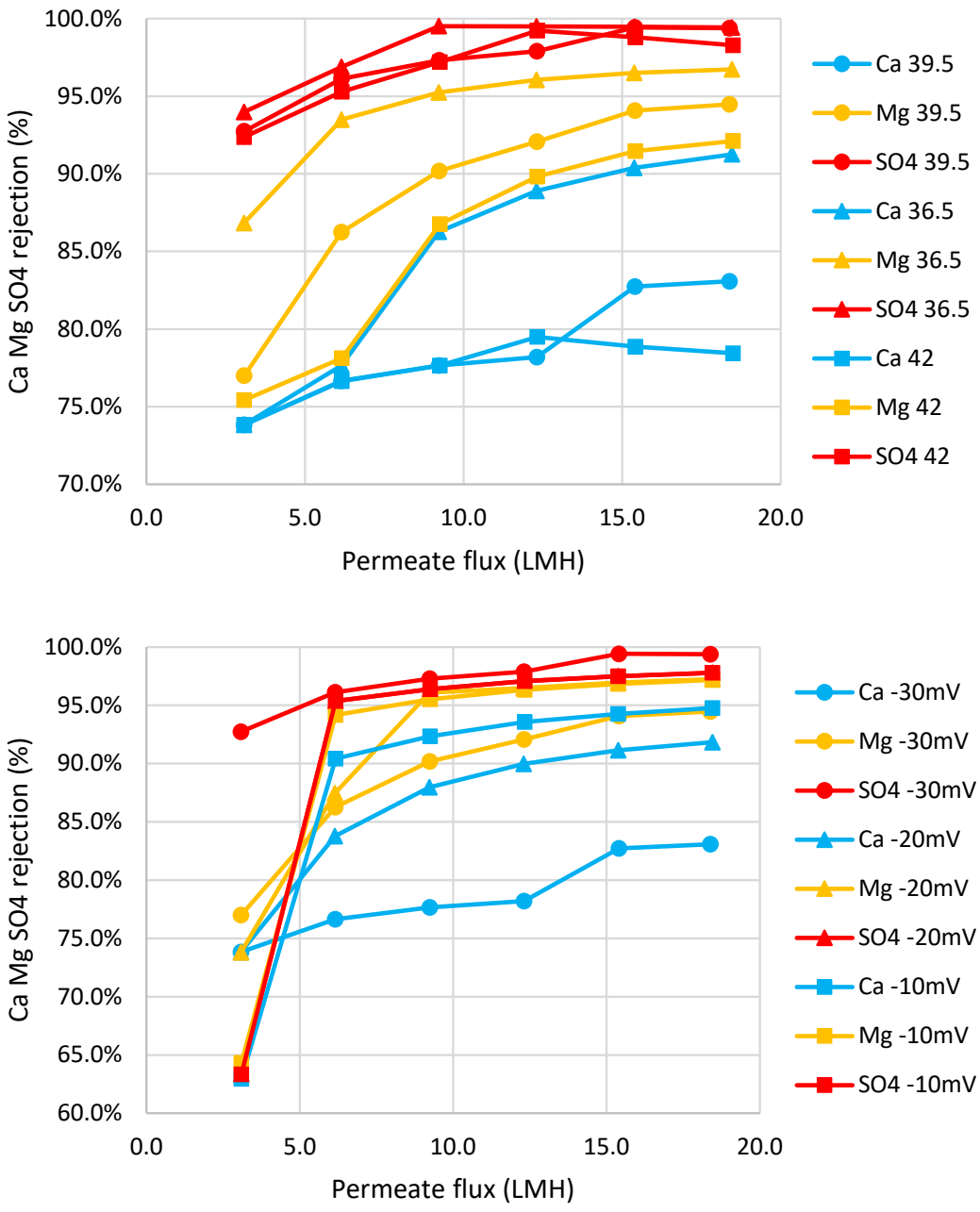

Figure 5-5 The effect of membrane pore dielectric constant and feed-membrane Donnan potentials on the Ca, Mg and SO_4 rejection performance of the MDS NF 8040 elements in the RO-NF-CD process

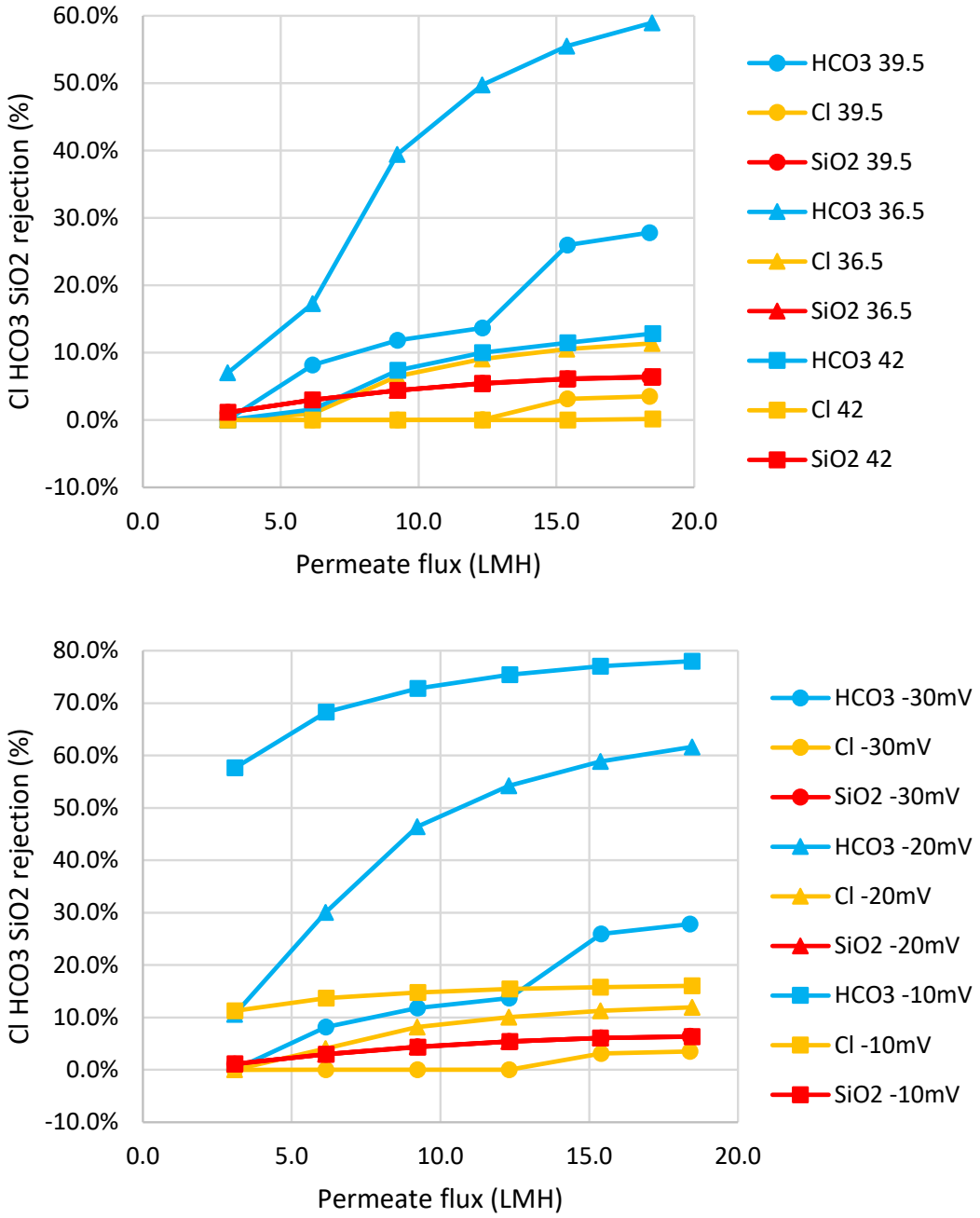

Figure 5-6 The effect of membrane pore dielectric constant and feed-membrane Donnan potentials on the Ca, Mg and SO_4 rejection performance of the MDS NF 8040 elements in the RO-NF-CD process

The comparison of the rejection performance of the MDS elements for $CaSO_4$ and Na_2SO_4 dominated solutions are shown in Figure 5-7. The ionic strength of the $CaSO_4$ and Na_2SO_4 dominated solutions were 0.083 and 0.32 in the feed respectively and 0.23 and 0.79 in the concentrate respectively. The same rejection of SO_4 was achieved however, the feed-membrane $\Delta\varphi_{D,M}$ of the $NaSO_4$ dominated solution was substantially lower at -4.5mV compared to the -30mV. The Ca and Mg rejections were lower for the $CaSO_4$ dominated solution and was attributed to the higher negative feed-membrane $\Delta\varphi_{D,M}$ resulting in attraction of cations at the feed-membrane interface. It was recommended that the impact of ionic strength and activity on the partitioning at the feed-membrane interface be studied further for application in high ionic strength RO concentrate treatment processes utilising NF.

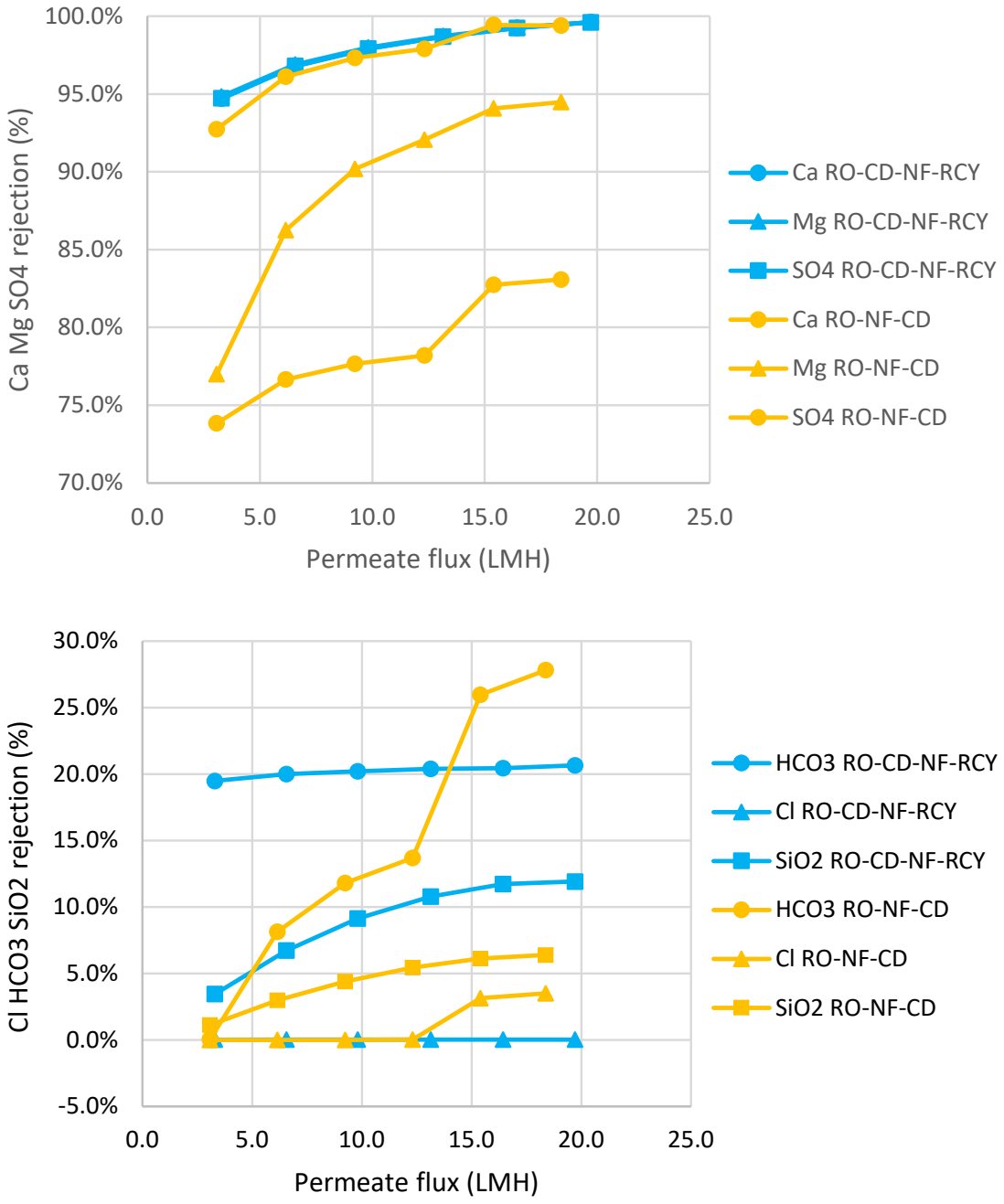

Figure 5-7 Comparison of rejection performance of the MDS NF 4040T (RO-CD-NF-RCY process) and MDS NF 8040 (RO-NF-CD process) elements for the Na_2SO_4 and $CaSO_4$ dominated solutions

5.5 Conclusions

The inclusion of the uncharged SiO_2 aqueous species (at the operating pH) and constraining the regression of rejection data to yield close agreement with the analytically determined SiO_2 rejections, yielded similar pore radii (0.535 and 0.57 nm respectively) and active layer thicknesses (0.3 μm for both) for the MDS NF 4040T and the MDS NF 8040 elements operating in the high ionic strength Na_2SO_4 dominated and $CaSO_4$ dominated feed liquors respectively. The inclusion of SiO_2 or another uncharged specie that responds similarly to steric partitioning, was recommended in DSPM & DE modelling of NF performance as it uncoupled the determination of pore-radii and effective active layer thickness from electrostatic effects.

The feed-membrane and membrane-permeate Donnan potentials, $\Delta\varphi_{D,m}$ and $\Delta\varphi_{D,p}$, to fit the rejection performance of the Na_2SO_4 and $CaSO_4$ dominated waters fed to the MDS NF 4040T and MDS NF 8040 elements were –4.5mV and +0.5mV and –30mV and +20mV respectively. The fundamental differences between this work and other ENP and DSPM & DE studies was (1) the arrangement of the ions into cation-anion ion pairs with a representative dominant ion, (2) the assignment of $\Delta\varphi_{D,m}$ and $\Delta\varphi_{D,p}$ as input values, and (3) the omission of the charge offset $-C_X$. The built NF model matched the rejection performance of the MDS elements in the RO-NF-CD and RO-CD-NF-RCY processes with resulting $\Delta\varphi_{D,m}$ and $\Delta\varphi_{D,p}$ values and membrane pore dielectric constant (39.5 for both NF elements) that were within the expected ranges for Polyamide membrane active layers. It was recommended that the NF model be fitted to additional operational data and the fitted parameters, $\Delta\varphi_{D,m}$, $\Delta\varphi_{D,p}$ and ε_{pore}, compared to fitted parameters of a conventional ENP and DSPM & DE model to better understand the limitations and advantages of the ion pairing with dominant ion feature of the built NF model.

The built NF model was considered to have three industrial applications – (1) tracking in service element degradation in terms of increasing pore radius, decreasing effective active layer thickness and decreasing feed-membrane $\Delta\varphi_{D,m}$, (2) element selection in the design of RO-NF-CD and RO-NF-CD-RCY processes and (3) estimation of unknown solute B values by considering the likely ion-pairs and dominant ions that it may form for a given solution type. The interface with the PHREEQC COM module for the calculation of

Pitzer activity and osmotic coefficients was considered an advantage for fitting of high ionic strength applications.

6 CONCLUSIONS AND RECOMMENDATIONS

6.1 Pilot objective

The *pilot objective* was to pilot the ICD-SNF variation with PRO concentrate feed and observe the cycling-up and subsequent steady state design philosophy. Data collection for the calibration of the process model developed in the process model objective was required.

A continuous pilot scale PRO-ICD-SNF experiment was conducted for over 350 hours to observe the evolution of TDS of the recirculated bulk liquor. The cycling up and subsequent approach to steady state of the recirculation liquor TDS were experimentally observed.

It was concluded that the pilot objective demonstrated the proof of concept of the selected ICD-SNF variation.

The following recommendations were made to improve the experimental procedure

i. The analytical work for precipitation reactor discharge liquors and SNF concentrate was less accurate due to the unstable nature of the samples. This should be addressed either through dilution of the sample or analytical procedure that can be performed shortly after sample grabbing; and

ii. The SNF element string (number of elements in series) was too long and not representative of the hydraulics of a full-scale membrane system. This further promoted scaling due to low cross flow velocities in the tail elements where, arguably, the retention time of the retentate was longer than the precipitation induction time. In the evaluation of ICD-SNF systems with large recycles, it is important to consider the mass transfer effects on the species rejection in the SNF system.

6.2 Process model objective

The *process model objective* was to integrate a solver algorithm and equipment sub models with PHREEQC version 3 to predict the cycled-up TDS of the recirculation liquor for the selected ICD-SNF variation.

The process model was programmed in MS VBA and successfully interfaced with PHREEQC COM v3. The model accurately estimated the cycled-up TDS of the selected ICD-SNF process for a large variety of process parameters including sludge solids and moisture content, secondary RO rejection characteristics, pH targets, gypsum and calcite precipitation performance and concentrate purge from SRO concentrate recycle.

The calibrated process model showed that a SNF concentrate purge of 1.2% would have been required to sustain the mass balance at the 297 hours in operation experimental point. This was an important finding as the pilot suggested that a higher overall volumetric recovery was attainable than what the process model predicted was sustainable. The results also showed that 96.5% of the PRO concentrate (TDS of 4170 $mg.L^{-1}$, gypsum SR 1.52) was recovered as a SNF permeate (TDS of 394 $mg.L^{-1}$) with sodium and sulphate concentrations below the taste threshold for drinking water.

The comparison of the process model and the pilot results showed agreement between the predicted and observed aqueous species concentrations and chemical consumption (Table 4-3 and Table 4-4) for the specified operating and performance parameters (Table 4-1 and Table 4-2).

The process model further indicated that sulphate reported to sludge solids, sludge moisture, SNF permeate and SNF concentrate purge streams at 83.8, 6.5, 2.9 and 6.8 wt. % respectively. Similarly, the amounts of sodium were found to be 0.0, 31.6, 38.7 and 29.7 wt. % respectively. Thus, sulphate reported predominantly to the sludge solids phase and sodium reported to the liquid phase of the waste streams.

The ICD-SNF design philosophy to confine gypsum precipitation to higher SRs for reaction driving force with subsequent reduction using CO_2 induced calcite precipitation, yielded a gypsum SR in the SNF concentrate that was within the generally accepted SR limit for effective scale suppression through antiscalant addition.

The applicability of the process model is limited by the equilibrium nature of the precipitation reactor sub model and the specification of SNF rejection ratios from piloting data. The applicability of the process model can be extended to different PRO-ICD-SNF or PCD-ICD-SNF systems if the SNF sub model can be predictive and the precipitation

reactor sub model can incorporate rate equations for at least the solids phases calcite and gypsum.

It was concluded that the process model is capable of predicting the cycled up TDS of the piloted ICD-SNF process variation as a function of sludge solids and moisture content, secondary RO rejection characteristics, pH targets, gypsum and calcite precipitation performance and concentrate purge from SRO concentrate recycle.

The following recommendations were made to improve the accuracy and rigour of the process model

i. Extend the applicability of the process model by incorporating rate-based precipitation estimates in the reactor sub model and predictive NF rejection sub model for SNF performance; and

ii. Evaluate different high ionic strength activity coefficient models. It is possible that pitzer.dat over estimates the solubility elevation of the sparingly soluble minerals and thus the operating point within the antiscalant performance envelope may be unsure or closer to the maximum.

6.3 Improved NF sub model objective

The *improved NF sub model objective* was to replace the calibrated NF rejection ratios with a predictive NF performance model.

A predictive NF sub model based on the Donnan steric pore model and dielectric exclusion (DSPM & DE) with extended Nernst Planck (ENP) active layer transport was developed. It addressed the rigour required to extend the applicability of the process model.

The fundamental differences between the predictive model developed in this research and other ENP with DSPM & DE studies were the arrangement of the ions into cation-anion ion pairs with a representative dominant ion, the assignment of feed-membrane and membrane-permeate Donnan potentials, $\Delta\varphi_{D,m}$ and $\Delta\varphi_{D,p}$, as input values and the omission of the charge offset $-C_X$. The model was fitted to NF rejection performance data from MDS NF 4040T and MDS NF 8040 elements operating in a pilot scale high

recovery recycle process and a full scale single pass process respectively, at a water treatment plant in Ghana. The results showed that the built NF model can predict the rejection performance of the MDS elements deployed in the RO-NF-CD and RO-CD-NF-RCY processes. The resulting $\Delta\varphi_{D,m}$ and $\Delta\varphi_{D,p}$ values and membrane pore dielectric constant, ε_{pore}, were within the expected ranges of Polyamide membrane active layers. The inclusion of the uncharged specie SiO_2 was done to regress pore-radii and active layer thickness of the NF membranes in the absence of electrostatic effects.

It was concluded that the predictive NF sub model is capable of predicting NF performance and that the inclusion of an uncharged aqueous specie such as SiO_2 substantially improves the accuracy and flexibility.

It is recommended that the NF model be fitted to additional operational data and the fitted parameters, $\Delta\varphi_{D,m}$, $\Delta\varphi_{D,p}$ and ε_{pore}, be compared to fitted parameters of a conventional ENP with DSPM & DE model to better understand the limitations and advantages of the ion pairing with dominant ion feature of the built NF model. The built NF model was considered to have three industrial applications – (1) tracking in service element degradation in terms of increasing pore radius, decreasing effective active layer thickness and decreasing feed-membrane $\Delta\varphi_{D,m}$, (2) element selection in the design of RO concentrate treatment processes and (3) estimation of unknown solute permeability values by considering the likely ion-pairs and dominant ions that characterises a given aqueous solution.

The inclusion of the predictive NF model into the process model will require the porting of the process model from MS VBA to Python.

It is further recommended that the equilibrium reactor with specified saturation ratios sub model be replaced with a rate-based reaction kinetics sub model for the major solids phases. The inclusion of such a rate-based reactor sub model, in combination with the predictive NF performance sub model, could substantially improve the predictive performance of the ICD-SNF model.

7 REFERENCES

Al-Obaidi, M. A., C. Kara-Zaitri and I. M. Mujtaba (2017). "Scope and limitations of the irreversible thermodynamics and the solution diffusion models for the separation of binary and multi-component systems in reverse osmosis process." Computers & Chemical Engineering **100**(Supplement C): 48-79.

Antony, A., J. H. Low, S. Gray, A. E. Childress, P. Le-Clech and G. Leslie (2011). "Scale formation and control in high pressure membrane water treatment systems: A review." Journal of Membrane Science **383**(1–2): 1-16.

Aoun, M., E. Plasari, R. David and J. Villermaux (1999). "A simultaneous determination of nucleation and growth rates from batch spontaneous precipitation." Chemical Engineering Science **54**(9): 1161-1180.

Appelo, C. A. J. (2015). "Principles, caveats and improvements in databases for calculating hydrogeochemical reactions in saline waters from 0 to 200°C and 1 to 1000atm." Applied Geochemistry **55**: 62-71.

Aquilano, D., F. Otálora, L. Pastero and J. M. García-Ruiz (2016). "Three study cases of growth morphology in minerals: Halite, calcite and gypsum." Progress in Crystal Growth and Characterization of Materials **62**(2): 227-251.

Artuğ, G. (2007). Modelling and Simulation of Nanofiltration Membranes, Cuvillier.

Bowen, W. R. and J. S. Welfoot (2002). "Modelling the performance of membrane nanofiltration—critical assessment and model development." Chemical Engineering Science **57**: 1121-1137.

Charlton, S. R. and D. L. Parkhurst (2011). "Modules based on the geochemical model PHREEQC for use in scripting and programming languages." Computers & Geosciences **37**(10): 1653-1663.

Charlton, S. R. and D. L. Parkhurst (2011). "Modules based on the geochemical model PHREEQC for use in scripting and programming languages." Computers & Geosciences **37**: 1653-1663.

Coulson, J. M., J. F. Richardson, J. R. Backhurst and J. H. Harker (1991). Chemical Engineering: Particle Technology and Separation Processes, Pergamon Press.

Crittenden, J. C., M. W. Harza, R. R. Trussell and D. W. Hand (2012). MWH's Water Treatment: Principles and Design, Wiley.

Degrémont SA. (2007). Water Treatment Handbook, Degrémont-Suez.

Doubra, P., A. Kamran-Pirzaman, A. H. Mohammadi and R. Hassanalizadeh (2017). "Thermodynamic modelling of scale (Calcite, Barite, Anhydrite and Gypsum) deposition from brine." Journal of Molecular Liquids **230**(Supplement C): 96-103.

Durand, J. F. (2012). "The impact of gold mining on the Witwatersrand on the rivers and karst system of Gauteng and North West Province, South Africa." Journal of African Earth Sciences **68**: 24-43.

Ferguson, R. J., B. R. Ferguson and R. F. Stancavage (2011). "Modeling Scale Formation and Optimizing Scale Inhibitor Dosages in Membrane Systems." AWWA Membrane Technology Conference.

Gabelich, C. J., M. D. Williams, A. Rahardianto, J. C. Franklin and Y. Cohen (2007). "High-recovery reverse osmosis desalination using intermediate chemical demineralization." Journal of Membrane Science **301**(1–2): 131-141.

Gabelich, C. J., M. D. Williams, A. Rahardianto, J. C. Franklin and Y. Cohen (2007). "High-recovery reverse osmosis desalination using intermediate chemical demineralization." Journal of Membrane Science **301**: 131-141.

Geraldes, V. and A. M. Brites Alves (2008). "Computer program for simulation of mass transport in nanofiltration membranes." Journal of Membrane Science **321**(2): 172-182.

Gledhill, D. K. and J. W. Morse (2006). "Calcite solubility in Na–Ca–Mg–Cl brines." Chemical Geology **233**(3–4): 249-256.

Greenlee, L. F., F. Testa, D. F. Lawler, B. D. Freeman and P. Moulin (2011). "Effect of antiscalant degradation on salt precipitation and solid/liquid separation of RO concentrate." Journal of Membrane Science **366**(1-2): 48-61.

Hamdona, S. K. and U. A. Al Hadad (2007). "Crystallization of calcium sulfate dihydrate in the presence of some metal ions." Journal of Crystal Growth **299**(1): 146-151.

Harvie, C. E., N. Moller and J. H. Weare (1984). "The prediction of mineral solubilities in natural waters: The Na-K-Mg_Ca-H-Cl-SO4-OH-HCO3-CO3-CO2-H2O system to high ionic strength at 25C." Geochimica et Cosmochimica Acta **48**: 723-751.

Harvie, C. E., N. Møller and J. H. Weare (1984). "The prediction of mineral solubilities in natural waters: The Na-K-Mg-Ca-H-Cl-SO4-OH-HCO3-CO3-CO2-H2O system to high ionic strengths at 25°C." Geochimica et Cosmochimica Acta **48**(4): 723-751.

Huminicki, D. M. C. and J. D. Rimstidt (2008). "Neutralization of sulfuric acid solutions by calcite dissolution and the application to anoxic limestone drain design." Applied Geochemistry **23**: 148-165.

INAP (2009) "Global Acid Rock Drainage Guide (GARD Guide)."

Johnson, D. B. and K. B. Hallberg (2005). "Acid mine drainage remediation options: a review." Total Environment **338**: 3-14.

Klepetsanis, P. G. and P. G. Koutsoukos (1991). "Spontaneous precipitation of calcium sulfate at conditions of sustained supersaturation." Journal of Colloid and Interface Science **143**(2): 299-308.

Klepetsanis, P. G. and P. G. Koutsoukos (1998). "Kinetics of calcium sulfate formation in aqueous media: effect of organophosphorus compounds." Journal of Crystal Growth **193**(1): 156-163.

Kosutic, K. and B. Kunst (2002). "RO and NF membrane fouling and cleaning and pore size distribution variations." Desalination **150**: 113-120.

Labban, O., C. Liu, T. H. Chong and J. H. Lienhard (2017). "Fundamentals of low-pressure nanofiltration: Membrane characterization, modeling, and understanding the multi-ionic interactions in water softening." Journal of Membrane Science **521**: 18-32.

Martin, A., D. Loomer, S. Fawcett, A. Rollo, A. Gault, H. Jamieson, S. Simpson and T. Al (2013). Characterization and Prediction of Trace Metal Bearing Phases in ARD Neutralization Sludges.

McCool, B. C., A. Rahardianto, J. I. Faria and Y. Cohen (2013). "Evaluation of chemically-enhanced seeded precipitation of RO concentrate for high recovery desalting of high salinity brackish water." Desalination **317**: 116-126.

mindat.org. "mindat.org." Retrieved 19-11-2017, from https://www.mindat.org/min-1784.html.

Nir, O. and O. Lahav (2013). "Coupling mass transport and chemical equilibrium models for improving the prediction of SWRO permeate boron concentrations." Desalination **310**: 87-92.

Nordstrom, D. K. (2011). "Hydrogeochemical processes governing the origin, transport and fate of major and trace elements from mine wastes and mineralised rock to surface waters." Applied Geochemistry **26**: 1777-1791.

Nordstrom, D. K., D. W. Blowes and C. J. Ptacek (2015). "Hydrogeochemistry and microbiology of mine drainage: An update." Applied Geochemistry **57**: 3-16.

Nordstrom, D. K., D. W. Blowes and C. J. Ptacek (2015). "Hydrogeochemistry and microbiology of mine drainage: An update." Applied Geochemistry: 3-16.

Parkhurst, D. L. and C. A. J. Apello (1999). User's guide to PHREEQC (Version 2) - A Computer program for speciation, batch-reaction, one-dimensional transport, and inverse geohemical calculations. Denver, Colorado, U.S. Geological Survey.

Peeters, J. M. M., J. P. Boom, M. H. V. Mulder and H. Strathmann (1998). "Retention measurements of nanofiltration membranes with electrolyte solutions." Journal of Membrane Science **145**(2): 199-209.

Pitzer, K. S. (1981). "Characteristics of very concentrated aqueous solutions." Physics and Chemistry of the Earth **13–14**: 249-272.

Plumlee, G. S. and S. A. Morman (2011). Mine Wastes and Human Health. Elements**:** 399 - 404.

Rahardianto, A., J. Gao, C. J. Gabelich, M. D. Williams and Y. Cohen (2007). "High recovery membrane desalting of low-salinity brackish water: Integration of accelerated precipitation softening with membrane RO." Journal of Membrane Science **289**: 123-137.

Rahardianto, A., J. Gao, C. J. Gabelich, M. D. Williams and Y. Cohen (2007). "High recovery membrane desalting of low-salinity brackish water: Integration of accelerated precipitation softening with membrane RO." Journal of Membrane Science **289**(1–2): 123-137.

Rahardianto, A., B. C. McCool and Y. Cohen (2010). "Accelerated desupersaturation of reverse osmosis concentrate by chemically-enhanced seeded precipitation." Desalination **264**(3): 256-267.

Randall, D. G. and J. Nathoo (2015). "A succinct review of the treatment of Reverse Osmosis brines using Freeze Crystallization." Journal of Water Process Engineering **8**: 186-194.

Stumm, W., L. Sigg and B. Sulzberger (1992). Chemistry of the Solid-Water Interface: Processes at the Mineral-Water and Particle-Water Interface in Natural Systems, Wiley.

Subramani, A. and J. G. Jacangelo (2014). "Treatment technologies for reverse osmosis concentrate volume minimization: A review." Separation and Purification Technology **122**: 472-489.

Uchymiak, M., E. Lyster, J. Glater and Y. Cohen (2008). "Kinetics of gypsum growth on a reverse osmosis membrane." Journal of Membrane Science **314**: 163-172.

United States Geological Survey. (1999). "Frequently Asked Questions for PHREEQC and PhreeqcI." Retrieved 01-10-2017, from https://wwwbrr.cr.usgs.gov/projects/GWC_coupled/phreeqc/faq.html.

Walton, N. R. G. (1989). "Electrical Conductivity and Total Dissolved Solids—What is Their Precise Relationship?" Desalination **72**(3): 275-292.

World Health Organization. (2003). "Sodium in drinking water." Retrieved 12 May 2016, from http://www.who.int/water_sanitation_health/dwq/chemicals/sodium.pdf.

World Health Organization. (2004). "Sulfate in drinking-water." Retrieved 12 May 2016, from http://www.who.int/water_sanitation_health/dwq/chemicals/sulfate.pdf

8 APPENDICES

Appendix A1: Analytical data – ICD-SNF Feed / Primary RO Concentrate

LABORATORY		SGS TEMA	SGS TEMA	SGS TEMA
HOURS IN OPERATION		158	203	297
SAMPLE	UNIT	AN004	AN004	AN004
pH		5.80	5.30	5.60
Conductivity	mS/m	414	406	411
Total Alkalinity as $CaCO_3$	mg/L	9	2	9
Total Dissolved Solids Dried at 180ºC	mg/L	4070	3630	4300
TDS / EC		0.98	0.89	1.05
Chloride	mg/L	31.7	31.0	30.9
Sulphate	mg/L	2240	2480	2830
Nitrate as NO_3	mg/L	272.0	274.0	304.0
Nitrate as N	mg/L	61.4	61.9	68.7
Silica	mg/L	136.0	116.0	112.0
Ammonia as N	mg/L	2.23	3.94	6.24
Fluoride by ISE	mg/L	1.20	1.00	1.30
Total Phosphorus	mg/L	0.09	0.50	<0.02
Total Cyanide	mg/L	<0.005	<0.005	<0.005
Arsenic dissolved	mg/L	0.17	0.25	0.17
Barium dissolved	mg/L	0.242	0.201	0.162
Chromium dissolved	mg/L	0.001	0.004	0.002
Copper dissolved	mg/L	0.004	0.004	0.013
Manganese dissolved	mg/L	0.003	0.002	0.003
Nickel dissolved	mg/L	0.019	0.028	0.050
Tin dissolved	mg/L	0.0009	0.0030	<0.0002
Strontium dissolved	mg/L	54.0	42.0	46.0
Uranium dissolved	mg/L	0.020	0.020	0.020
Calcium dissolved	mg/L	773.0	760.0	842.0
Magnesium dissolved	mg/L	149.0	149.0	156.0
Sodium dissolved	mg/L	146.0	160.0	168.0
Potassium dissolved	mg/L	19.2	23.5	23.3
Aluminium dissolved	mg/L	<0.03	<0.03	<0.03
Iron dissolved	mg/L	<0.1	<0.1	<0.1

Appendix A2: Analytical data – SNF Feed / Recirculation Liquor

LABORATORY		SGS TEMA	SGS TEMA	SGS TEMA
HOURS IN OPERATION		158	203	297
SAMPLE	UNIT	AN008	AN008	AN008
pH		4.60	4.80	4.80
Conductivity	mS/m	1560	1540	1760
Total Alkalinity as $CaCO_3$	mg/L	<2	<2	<2
Total Dissolved Solids Dried at 180ºC	mg/L	15150	13900	16750
TDS / EC		0.97	0.90	0.95
Chloride	mg/L	13.8	14.1	12.4
Sulphate	mg/L	11200	10700	13600
Nitrate as NO_3	mg/L	158.0	152.0	158.0
Nitrate as N	mg/L	35.7	34.3	35.7
Silica	mg/L	27.3	16.2	13.0
Ammonia as N	mg/L	13.00	11.40	23.70
Fluoride by ISE	mg/L	0.20	0.20	0.10
Total Phosphorus	mg/L	0.70	0.08	<0.02
Total Cyanide	mg/L	<0.005	<0.005	<0.005
Arsenic dissolved	mg/L	0.018	0.018	0.013
Barium dissolved	mg/L	0.031	0.018	0.018
Chromium dissolved	mg/L	0.023	0.002	0.002
Copper dissolved	mg/L	0.003	0.003	0.004
Manganese dissolved	mg/L	<0.002	<0.002	<0.002
Nickel dissolved	mg/L	0.003	0.002	0.009
Tin dissolved	mg/L	0.0010	0.0004	<0.0002
Strontium dissolved	mg/L	20.0	14.0	18.0
Uranium dissolved	mg/L	0.001	0.000	0.0003
Calcium dissolved	mg/L	460.0	327.0	537.0
Magnesium dissolved	mg/L	48.2	35.3	26.9
Sodium dissolved	mg/L	4480	4360	5530
Potassium dissolved	mg/L	192.0	162.0	238.0
Aluminium dissolved	mg/L	<0.03	<0.03	<0.03
Iron dissolved	mg/L	<0.1	<0.1	<0.1

Appendix A3: Analytical data – SNF Concentrate

LABORATORY		SGS TEMA	SGS TEMA	SGS TEMA
HOURS IN OPERATION		158	203	297
SAMPLE	UNIT	AN009	AN009	AN009
pH		4.50	4.70	4.60
Conductivity	mS/m	4490	3790	4780
Total Alkalinity as $CaCO_3$	mg/L	<2	<2	<2
Total Dissolved Solids Dried at 180ºC	mg/L	27800	28000	32900
TDS / EC		0.62	0.74	0.69
Chloride	mg/L	<0.1	<0.1	<0.1
Sulphate	mg/L	26400	20600	24700
Nitrate as NO_3	mg/L	14.4	14.4	12.2
Nitrate as N	mg/L	3.3	3.3	2.8
Silica	mg/L	29.7	16.8	14.0
Ammonia as N	mg/L	25.20	24.50	46.20
Fluoride by ISE	mg/L	<0.1	<0.1	<0.1
Total Phosphorus	mg/L	2.21	2.80	<0.02
Total Cyanide	mg/L	<0.005	<0.005	<0.005
Arsenic dissolved	mg/L	0.022	0.019	0.015
Barium dissolved	mg/L	0.050	0.032	0.027
Chromium dissolved	mg/L	0.004	0.002	0.002
Copper dissolved	mg/L	0.003	0.003	0.004
Manganese dissolved	mg/L	<0.002	<0.002	<0.002
Nickel dissolved	mg/L	0.003	0.002	0.010
Tin dissolved	mg/L	0.0007	0.0005	<0.0002
Strontium dissolved	mg/L	30.0	20.0	26.0
Uranium dissolved	mg/L	0.001	0.000	0.0004
Calcium dissolved	mg/L	868.0	664.0	1050.0
Magnesium dissolved	mg/L	94.4	70.1	50.7
Sodium dissolved	mg/L	8340	8450	9790
Potassium dissolved	mg/L	350.0	312.0	494.0
Aluminium dissolved	mg/L	<0.03	<0.03	<0.03
Iron dissolved	mg/L	0.10	<0.1	0.10

Appendix A4: Analytical data – SNF Permeate

LABORATORY		SGS TEMA	SGS TEMA	SGS TEMA
HOURS IN OPERATION		158	203	297
SAMPLE	UNIT	AN010	AN010	AN010
pH		5.20	5.10	5.30
Conductivity	mS/m	98	95	98
Total Alkalinity as $CaCO_3$	mg/L	<2	<2	3
Total Dissolved Solids Dried at 180ºC	mg/L	750	666	686
TDS / EC		0.77	0.70	0.70
Chloride	mg/L	34.5	33.9	33.6
Sulphate	mg/L	152	140	146
Nitrate as NO_3	mg/L	316.0	274.0	292.0
Nitrate as N	mg/L	71.4	61.9	66.0
Silica	mg/L	24.6	15.1	11.7
Ammonia as N	mg/L	0.53	0.42	0.65
Fluoride by ISE	mg/L	0.50	0.40	0.40
Total Phosphorus	mg/L	0.28	0.22	<0.02
Total Cyanide	mg/L	<0.005	<0.005	<0.005
Arsenic dissolved	mg/L	0.02	0.03	0.01
Barium dissolved	mg/L	0.002	<0.001	<0.001
Chromium dissolved	mg/L	0.008	<0.001	0.001
Copper dissolved	mg/L	0.005	0.007	0.003
Manganese dissolved	mg/L	<0.002	<0.002	<0.002
Nickel dissolved	mg/L	<0.001	<0.001	<0.001
Tin dissolved	mg/L	0.0007	<0.0002	0.0005
Strontium dissolved	mg/L	0.9	0.8	0.2
Uranium dissolved	mg/L	0.000	<0.0001	0.0002
Calcium dissolved	mg/L	<1	<1	<1
Magnesium dissolved	mg/L	<0.5	<0.5	<0.5
Sodium dissolved	mg/L	188.0	182.0	194.0
Potassium dissolved	mg/L	6.5	6.0	7.2
Aluminium dissolved	mg/L	<0.03	<0.03	<0.03
Iron dissolved	mg/L	<0.1	<0.1	<0.1

Appendix A5: Analytical data – Gypsum reactor discharge

LABORATORY		SGS TEMA	SGS TEMA	SGS TEMA
HOURS IN OPERATION		158	203	297
SAMPLE	UNIT	AN006	AN006	AN006
pH		12.60	12.50	12.50
Conductivity	mS/m	4600	3930	4800
Total Alkalinity as $CaCO_3$	mg/L	2360	2500	1930
Total Dissolved Solids Dried at 180ºC	mg/L	25950	25450	29100
TDS / EC		0.56	0.65	0.61
Chloride	mg/L	<0.1	<0.1	<0.1
Sulphate	mg/L	16600	18400	22300
Nitrate as NO_3	mg/L	23.5	27.7	20.1
Nitrate as N	mg/L	5.3	6.3	4.5
Silica	mg/L	5.7	6.9	7.7
Ammonia as N	mg/L	14.40	5.38	3.24
Fluoride by ISE	mg/L	6.30	7.10	7.80
Total Phosphorus	mg/L	0.66	0.47	<0.02
Total Cyanide	mg/L	<0.005	<0.005	<0.005
Arsenic dissolved	mg/L	0.017	0.017	0.018
Barium dissolved	mg/L	0.034	0.017	0.024
Chromium dissolved	mg/L	0.002	0.002	0.003
Copper dissolved	mg/L	0.003	0.004	0.005
Manganese dissolved	mg/L	<0.002	<0.002	<0.002
Nickel dissolved	mg/L	0.003	0.003	0.011
Tin dissolved	mg/L	0.0020	0.0030	0.0003
Strontium dissolved	mg/L	14.0	11.0	19.0
Uranium dissolved	mg/L	0.002	0.001	0.001
Calcium dissolved	mg/L	635.0	682.0	743.0
Magnesium dissolved	mg/L	<0.5	<0.5	<0.5
Sodium dissolved	mg/L	9070	8310	10100
Potassium dissolved	mg/L	380.0	308.0	462.0
Aluminium dissolved	mg/L	<0.03	<0.03	<0.03
Iron dissolved	mg/L	<0.1	<0.1	<0.1

Appendix A6: Analytical data – Calcite reactor discharge

LABORATORY		SGS TEMA	SGS TEMA	SGS TEMA
HOURS IN OPERATION		158	203	297
SAMPLE	UNIT	AN007	AN007	AN007
pH		11.30	10.40	11.40
Conductivity	mS/m	1530	1510	1760
Total Alkalinity as $CaCO_3$	mg/L	2410	1460	1750
Total Dissolved Solids Dried at 180ºC	mg/L	13900	14450	17950
TDS / EC		0.91	0.96	1.02
Chloride	mg/L	13.8	13.9	12.1
Sulphate	mg/L	10900	10800	15300
Nitrate as NO_3	mg/L	156.0	154.0	142.0
Nitrate as N	mg/L	35.2	34.8	32.1
Silica	mg/L	2.4	2.1	1.1
Ammonia as N	mg/L	6.06	12.80	7.43
Fluoride by ISE	mg/L	0.50	0.40	0.30
Total Phosphorus	mg/L	0.22	0.08	<0.02
Total Cyanide	mg/L	<0.005	<0.005	<0.005
Arsenic dissolved	mg/L	0.016	0.016	0.013
Barium dissolved	mg/L	0.022	0.016	0.019
Chromium dissolved	mg/L	0.002	0.002	0.002
Copper dissolved	mg/L	0.003	0.003	0.004
Manganese dissolved	mg/L	<0.002	<0.002	<0.002
Nickel dissolved	mg/L	0.002	0.003	0.014
Tin dissolved	mg/L	0.0007	0.0007	0.0002
Strontium dissolved	mg/L	17.0	14.0	19.0
Uranium dissolved	mg/L	0.001	0.001	0.000
Calcium dissolved	mg/L	394.0	384.0	561.0
Magnesium dissolved	mg/L	4.2	40.6	1.8
Sodium dissolved	mg/L	5010	4430	5990
Potassium dissolved	mg/L	194.0	166.0	244.0
Aluminium dissolved	mg/L	<0.03	<0.03	<0.03
Iron dissolved	mg/L	<0.1	<0.1	<0.1

Appendix A7: Analytical data – Feed water to RO plant (Mine impacted water)

LABORATORY		SGS TEMA	SGS TEMA	SGS TEMA
HOURS IN OPERATION		158	203	297
SAMPLE	UNIT	AN001	AN001	AN001
pH		7.90	7.90	8.00
Conductivity	mS/m	115	103	117
Total Alkalinity as $CaCO_3$	mg/L	91	78	93
Total Dissolved Solids Dried at 180ºC	mg/L	846	742	886
TDS / EC		0.74	0.72	0.76
Chloride	mg/L	6.9	7.1	7.8
Sulphate	mg/L	513	421	496
Nitrate as NO_3	mg/L	74.0	70.3	77.9
Nitrate as N	mg/L	16.7	15.9	17.6
Silica	mg/L	27.6	23.1	23.4
Ammonia as N	mg/L	0.74	1.07	1.63
Fluoride by ISE	mg/L	0.40	0.40	0.40
Total Phosphorus	mg/L	<0.02	<0.02	<0.02
Dissolved Oxygen	mg/L			7.60
Chemical Oxygen Demand	mg/L		<25	48.0
Biochemical Oxygen Demand (BOD5)	mg/L			<5
Total Cyanide	mg/L	<0.005	<0.005	<0.005
Arsenic dissolved	mg/L	0.003	0.07	0.06
Barium dissolved	mg/L	<0.001	0.038	0.047
Chromium dissolved	mg/L	<0.001	0.002	0.001
Copper dissolved	mg/L	0.001	0.001	0.065
Manganese dissolved	mg/L	<0.002	<0.002	<0.002
Nickel dissolved	mg/L	<0.001	0.007	0.025
Tin dissolved	mg/L	<0.0002	0.0010	<0.0002
Strontium dissolved	mg/L	0.3	8.9	11.0
Uranium dissolved	mg/L	<0.0001	0.010	0.009
Calcium dissolved	mg/L	162.0	144.0	159.0
Magnesium dissolved	mg/L	35.0	32.2	34.1
Sodium dissolved	mg/L	32.6	30.9	33.2
Potassium dissolved	mg/L	4.7	4.9	5.0
Aluminium dissolved	mg/L	<0.03	<0.03	<0.03
Iron dissolved	mg/L	<0.1	<0.1	<0.1

Appendix B1: PRO concentrate EC, SNF feed EC and SNF recovery logsheet

Stage	Hours in operation	Primary RO concentrate electrical conductivity	Recirculation liquor electrical conductivity	SNF volumetric recovery	ΔEC / Δdt
		µS/cm	µS/cm	%	
Establish recirculation	1	3125	3930	57.1	
Establish recirculation	2	3094	3786	58.1	
Establish recirculation	3	3118	3786	58.1	
Establish recirculation	4	3099	3689	61.3	
Establish recirculation	5	3106	3698	60.0	
Establish recirculation	6	3534.5	3686	60.0	
Establish recirculation	7	3534.5	3723	58.1	
Establish recirculation	8	3963	3723	60.0	
Establish recirculation	9	3122	4360	60.0	
Establish recirculation	10	3120	4370	60.0	
Establish recirculation	11	3095	4370	60.0	
Establish recirculation	12	3081	4630	60.0	
Establish recirculation	13	3067	4960	60.0	
Establish recirculation	14	3048	5140	60.0	
Establish recirculation	15	3062	5180	60.0	
Establish recirculation	16	3032	5260	60.0	
Establish recirculation	17	3064	5210	60.0	
Establish recirculation	18	3031	5866	60.0	
Establish recirculation	19	3037	5738	60.0	
Establish recirculation	20	3042	5836	60.0	
Establish recirculation	21	3011	5826	60.0	
Establish recirculation	22	3041	5780	60.0	
Establish recirculation	23	3019	5880	60.0	
Establish recirculation	24	3009	5746	60.0	79.0
Establish recirculation	25	3009	5717	60.0	84.0
Establish recirculation	26	3019	5770	60.0	86.3
Establish recirculation	27	3007	5932	60.0	97.5
Establish recirculation	28	3055	5914	60.0	96.3
Establish recirculation	29	3650	5704	60.0	87.7
Establish recirculation	30	3050	5779	60.0	89.4
Establish recirculation	31	3045	5960	60.0	97.3
Establish recirculation	32	3109	6010	60.0	71.7
Establish recirculation	33	3128	6340	60.0	85.7
Establish recirculation	34	3111	6290	60.0	83.5
Establish recirculation	35	3114	6112	60.0	64.4
Establish recirculation	36	3123	6010	60.0	45.7
Establish recirculation	37	3030	5630	60.0	21.3
Establish recirculation	38	3071	5930	60.0	32.6

Stage	Hours in operation	Primary RO concentrate electrical conductivity	Recirculation liquor electrical conductivity	SNF volumetric recovery	ΔEC / Δdt
Establish recirculation	39	3102	6030	60.0	33.5
Establish recirculation	40	3120	5890	60.0	29.6
Establish recirculation	41	3107	6060	60.0	8.4
Establish recirculation	42	3135	6050	60.0	13.6
Establish recirculation	43	3144	6060	60.0	9.8
Establish recirculation	44	3139	6080	60.0	11.0
Establish recirculation	45	3125	6170	60.0	17.0
Establish recirculation	46	3117	6170	60.0	12.6
Establish recirculation	47	3141	6140	60.0	17.1
Establish recirculation	48	3130	6180	60.0	20.1
Establish recirculation	49	3116	6260	60.0	21.3
Establish recirculation	50	3120	6460	60.0	23.0
Establish recirculation	51	3137	6540	58.6	27.2
Establish recirculation	52	3097	6650	58.6	41.1
Establish recirculation	53	3096	6660	60.7	38.3
Establish recirculation	54	3064	6700	60.7	32.2
Establish recirculation	55	3088	6650	60.7	27.8
Establish recirculation	56	3062	6630	60.7	12.6
Establish recirculation	57	3089	6470	62.1	7.8
Establish recirculation	58	3074	6500	60.7	16.9
Establish recirculation	59	3086	6450	60.7	19.1
Establish recirculation	60	3061	6490	60.7	37.4
Establish recirculation	61	3074	6450	60.7	22.6
Establish recirculation	62	3087	6480	60.7	19.6
Establish recirculation	63	3097	6600	60.7	30.9
Establish recirculation	64	3089	6550	60.7	21.3
Establish recirculation	65	3055	6660	60.7	26.5
Establish recirculation	66	3107	6460	60.7	17.4
Establish recirculation	67	3077	6350	58.6	11.7
Establish recirculation	68	3088	6400	58.6	10.0
Establish recirculation	69	3011	6400	58.6	10.0
Establish recirculation	70	3102	6500	58.6	15.7
Establish recirculation	71	3097	6600	58.6	18.3
Establish recirculation	72	3087	6700	58.6	19.1
Establish recirculation	73	3054	6700	58.6	10.4
Establish recirculation	74	3075	6700	58.6	7.0
Establish recirculation	75	3062	6800	58.6	6.5
Accelerated cycling up	76	3938	6740	60.0	3.5
Accelerated cycling up	77	4000	6800	60.7	4.3
Accelerated cycling up	78	3937	6900	60.7	10.9
Accelerated cycling up	79	3995	6810	60.7	7.8

Stage	Hours in operation	Primary RO concentrate electrical conductivity	Recirculation liquor electrical conductivity	SNF volumetric recovery	ΔEC / Δdt
Accelerated cycling up	80	3976	6940	60.7	20.4
Accelerated cycling up	81	3977	6910	60.7	17.8
Accelerated cycling up	82	3938	6900	60.7	19.6
Accelerated cycling up	83	4006	6900	60.7	17.8
Accelerated cycling up	84	3982	7000	60.7	23.9
Accelerated cycling up	85	3979	7050	60.7	24.8
Accelerated cycling up	86	3938	7150	58.6	23.9
Accelerated cycling up	87	3885	7150	58.6	26.1
Accelerated cycling up	88	3882	7190	58.6	23.0
Accelerated cycling up	89	3861	7270	58.6	35.2
Accelerated cycling up	90	3873	7320	58.6	42.2
Accelerated cycling up	91	3902	7400	58.6	43.5
Accelerated cycling up	92	3913	7400	58.6	43.5
Accelerated cycling up	93	3911	7500	58.6	43.5
Accelerated cycling up	94	3910	7600	58.6	43.5
Accelerated cycling up	95	3902	7600	58.6	39.1
Accelerated cycling up	96	3910	7600	58.6	39.1
Accelerated cycling up	97	3939	7700	58.6	43.5
Accelerated cycling up	98	3937	7600	58.6	34.8
Accelerated cycling up	99	3913	7660	58.6	40.0
Accelerated cycling up	100	3884	7840	58.6	45.2
Accelerated cycling up	101	3930	7890	58.6	43.0
Accelerated cycling up	102	3919	7890	58.6	47.0
Accelerated cycling up	103	3955	7900	58.6	41.7
Accelerated cycling up	104	3941	7890	58.6	42.6
Accelerated cycling up	105	3948	8110	58.6	52.6
Accelerated cycling up	106	3537	8920	58.6	87.8
Accelerated cycling up	107	3919	8110	58.6	48.3
Accelerated cycling up	108	3631	8780	58.6	75.2
Accelerated cycling up	109	3956	8190	58.6	45.2
Accelerated cycling up	110	3841	8190	58.6	45.2
Accelerated cycling up	111	3885	8200	58.6	43.9
Accelerated cycling up	112	3879	8640	58.6	59.6
Steady cycling up	113	3822	8550	51.5	53.5
Steady cycling up	114	3955	8600	50.0	52.2
Steady cycling up	115	4006	8480	50.0	47.0
Steady cycling up	116	3995	8640	50.0	49.6
Steady cycling up	117	4002	9360	48.3	76.5
Steady cycling up	118	3962	9140	48.4	67.0
Steady cycling up	119	4031	9140	50.0	67.0
Steady cycling up	120	3949	9730	50.0	88.3

Stage	Hours in operation	Primary RO concentrate electrical conductivity	Recirculation liquor electrical conductivity	SNF volumetric recovery	ΔEC / Δdt
Steady cycling up	121	3952	9630	50.0	88.3
Steady cycling up	122	3963	9520	50.0	80.9
Steady cycling up	123	3967	9580	50.0	75.7
Steady cycling up	124	3942	10090	50.0	95.7
Steady cycling up	125	3965	10140	50.0	97.8
Steady cycling up	126	3984	10800	50.0	126.1
Steady cycling up	127	4035	11100	50.0	139.6
Steady cycling up	128	4027	11560	50.0	150.0
Steady cycling up	129	3995	11400	50.0	107.8
Steady cycling up	130	3949	11370	50.0	141.7
Steady cycling up	131	3982	12410	50.0	157.8
Steady cycling up	132	3967	12570	50.0	190.4
Steady cycling up	133	3974	12520	50.0	188.3
Steady cycling up	134	3894	12840	50.0	201.7
Steady cycling up	135	3835	12850	50.0	183.0
Steady cycling up	136	3902	12900	48.4	189.1
Steady cycling up	137	3910	12800	50.0	182.6
Steady cycling up	138	3897	12430	50.0	171.7
Steady cycling up	139	3957	12510	50.0	168.3
Steady cycling up	140	3998	13270	50.0	170.0
Steady cycling up	141	3951	13500	50.0	189.6
Steady cycling up	142	3999	13610	50.0	194.3
Steady cycling up	143	3971	13520	50.0	164.8
Steady cycling up	144	3955	13510	50.0	168.7
Steady cycling up	145	3946	13870	50.0	189.1
Steady cycling up	146	3991.8	13800	50.0	183.5
Steady cycling up	147	3999.6	14040	50.0	171.7
Steady cycling up	148	3979	14200	50.0	176.5
Steady cycling up	149	3988	14510	50.0	161.3
Steady cycling up	150	3688	14470	50.0	146.5
Steady cycling up	151	3655	14770	50.0	139.6
Steady cycling up	152	3680	14910	50.0	152.6
Steady cycling up	153	3692	14930	50.0	154.8
Steady cycling up	154	3694	14880	50.0	107.4
Steady cycling up	155	3693	15140	50.0	111.7
Steady cycling up	156	3728	15140	50.0	113.9
Steady cycling up	157	3616	15150	48.4	100.4
Steady cycling up	158	3620	15180	48.4	101.3
Steady cycling up	159	3566	15490	50.0	112.6
Steady cycling up	160	3611	15600	50.0	121.7
Steady cycling up	161	3587	15390	50.0	128.7

Stage	Hours in operation	Primary RO concentrate electrical conductivity	Recirculation liquor electrical conductivity	SNF volumetric recovery	ΔEC / Δdt
Steady cycling up	162	3519	15890	50.0	147.0
Steady cycling up	163	3562	15910	50.0	114.8
Steady cycling up	164	3576	15730	50.0	97.0
Steady cycling up	165	3558	15820	50.0	96.1
Steady cycling up	166	3532	15930	50.0	104.8
Steady cycling up	167	3539	15860	50.0	102.2
Steady cycling up	168	3544	16130	50.0	98.3
Steady cycling up	169	3481	16090	50.0	99.6
Steady cycling up	170	3548	16110	50.0	90.0
Steady cycling up	171	3487	16050	50.0	80.4
Steady cycling up	172	3474	16280	50.0	77.0
Steady cycling up	173	3598	16300	50.0	79.6
Steady cycling up	174	3509	15920	50.0	50.0
Steady cycling up	175	3549	16400	50.0	64.8
Steady cycling up	176	3517	15830	50.0	39.1
Steady cycling up	177	3531	15870	50.0	43.0
Steady cycling up	178	3576	16480	50.0	58.3
Steady cycling up	179	3521	16970	50.0	79.6
Steady cycling up	180	3590	16850	50.0	73.9
Steady cycling up	181	3620	16930	50.0	76.1
Steady cycling up	182	3539	16430	50.0	40.9
Steady cycling up	183	3597	16560	50.0	41.7
Steady cycling up	184	3637	16490	50.0	47.8
Steady cycling up	185	3548	16800	50.0	39.6
Steady cycling up	186	3659	16580	50.0	29.1
Steady cycling up	187	3707	16730	50.0	43.5
Steady cycling up	188	3328	16740	50.0	40.0
Steady cycling up	189	3474	16770	50.0	36.5
Steady cycling up	190	3651	16600	50.0	32.2
Steady cycling up	191	3664	16930	50.0	34.8
Steady cycling up	192	3678	16840	50.0	32.6
Steady cycling up	193	3558	16870	50.0	33.0
Steady cycling up	194	3665	16950	50.0	39.1
Steady cycling up	195	3612	16940	50.0	28.7
Steady cycling up	196	3752	16800	50.0	21.7
Steady cycling up	197	3711	16980	50.0	46.1
Steady cycling up	198	3710	16920	50.0	22.6
Steady cycling up	199	3684	16670	50.0	36.5
Steady cycling up	200	3743	16560	50.0	30.0
Steady cycling up	201	3714	16820	50.0	14.8
Steady cycling up	202	3761	16720	50.0	-10.9

Stage	Hours in operation	Primary RO concentrate electrical conductivity	Recirculation liquor electrical conductivity	SNF volumetric recovery	ΔEC / Δdt
Steady cycling up	203	3796	16510	50.0	-14.8
Steady cycling up	204	3747	16740	50.0	-8.3
Steady cycling up	205	3752	16600	50.0	7.4
Steady cycling up	206	3752	16860	50.0	13.0
Steady cycling up	207	3724	16660	50.0	7.4
Steady cycling up	208	3713	16910	50.0	4.8
Steady cycling up	209	3705	16930	50.0	15.2
Steady cycling up	210	3763	17020	50.0	12.6
Steady cycling up	211	3727	16960	50.0	9.6
Steady cycling up	212	3654	16800	50.0	1.3
Steady cycling up	213	3711	16880	50.0	12.2
Steady cycling up	214	3642	16880	50.0	-2.2
Steady cycling up	215	3714	16800	50.0	-1.7
Steady cycling up	216	3783	16890	50.0	0.9
Steady cycling up	217	3661	16950	50.0	0.0
Steady cycling up	218	3697	16900	50.0	-1.7
Steady cycling up	219	3678	16990	50.0	8.3
Steady cycling up	220	3670	17280	50.0	13.0
Cyclic operation	221	3866	17240	50.0	13.9
Cyclic operation	222	3879	18400	50.0	75.2
Cyclic operation	223	3714	17800	50.0	53.9
Cyclic operation	224	3879	17080	50.0	11.3
Cyclic operation	225	3892	16920	50.0	8.7
Cyclic operation	226	3939	17230	50.0	31.3
Cyclic operation	227	3919	17120	50.0	16.5
Cyclic operation	228	3902	17140	50.0	23.5
Cyclic operation	229	3932	17310	50.0	19.6
Cyclic operation	230	3957	17330	50.0	29.1
Cyclic operation	231	3959	17300	50.0	17.0
Cyclic operation	232	3987	17540	50.0	26.5
Cyclic operation	233	3878	17500	50.0	20.9
Cyclic operation	234	4076	17640	50.0	29.6
Cyclic operation	235	4019	18000	50.0	52.2
Cyclic operation	236	4012	18070	50.0	51.7
Cyclic operation	237	3905	18110	50.0	53.5
Cyclic operation	238	3845	18250	50.0	63.0
Cyclic operation	239	3949	18160	50.0	55.2
Cyclic operation	240	3943	18660	50.0	74.3
Cyclic operation	241	3962	18170	50.0	55.2
Cyclic operation	242	3996	18290	50.0	56.5
Cyclic operation	243	3972	18210	50.0	40.4

Stage	Hours in operation	Primary RO concentrate electrical conductivity	Recirculation liquor electrical conductivity	SNF volumetric recovery	ΔEC / Δdt
Cyclic operation	244	3873	18130	50.0	38.7
Cyclic operation	245	3947	18190	50.0	-9.1
Cyclic operation	246	3962	18620	50.0	35.7
Cyclic operation	247	3949	18260	50.0	51.3
Cyclic operation	248	3945	18250	50.0	57.8
Cyclic operation	249	3990	18160	50.0	40.4
Cyclic operation	250	3980	18400	50.0	55.7
Cyclic operation	251	3894	18100	50.0	41.7
Cyclic operation	252	3896	18050	50.0	32.2
Cyclic operation	253	3943	17960	50.0	27.4
Cyclic operation	254	3940	17860	50.0	24.3
Cyclic operation	255	3892	18190	50.0	28.3
Cyclic operation	256	3854	18200	50.0	30.4
Cyclic operation	257	3887	18220	50.0	25.2
Cyclic operation	258	3758	18190	50.0	8.3
Cyclic operation	259	3762	17910	50.0	-7.0
Cyclic operation	260	3924	17870	50.0	-10.4
Cyclic operation	261	3816	18000	50.0	-10.9
Cyclic operation	262	3784	17900	50.0	-11.3
Cyclic operation	263	3879	17860	50.0	-34.8
Cyclic operation	264	3880	17970	50.0	-8.7
Cyclic operation	265	3886	17870	50.0	-18.3
Cyclic operation	266	3968	17910	50.0	-13.0
Cyclic operation	267	3901	17810	50.0	-13.9
Cyclic operation	268	3894	17640	50.0	-23.9
Cyclic operation	269	3945	17360	50.0	-54.8
Cyclic operation	270	3944	17710	50.0	-23.9
Cyclic operation	271	3886	17970	50.0	-12.2
Cyclic operation	272	3982	17990	50.0	-7.4
Cyclic operation	273	3867	18600	50.0	8.7
Cyclic operation	274	3861	17800	50.0	-13.0
Cyclic operation	275	3893	17950	50.0	-4.3
Cyclic operation	276	3821	17580	50.0	-16.5
Cyclic operation	277	3892	17520	50.0	-14.8
Cyclic operation	278	3870	17590	50.0	-26.1
Cyclic operation	279	3923	17480	50.0	-31.3
Cyclic operation	280	3889	17490	50.0	-31.7
Cyclic operation	281	3855	17300	50.0	-38.7
Cyclic operation	282	3875	17300	50.0	-26.5
Cyclic operation	283	3846	17600	50.0	-11.7
Cyclic operation	284	3874	17900	50.0	-4.3

Stage	Hours in operation	Primary RO concentrate electrical conductivity	Recirculation liquor electrical conductivity	SNF volumetric recovery	ΔEC / Δdt
Cyclic operation	285	3885	17190	50.0	-30.9
Cyclic operation	286	3885	17870	50.0	0.4
Cyclic operation	287	3887	18140	50.0	7.4
Cyclic operation	288	3885	18800	50.0	40.4
Cyclic operation	289	3872	18640	50.0	31.7
Cyclic operation	290	3579	18820	50.0	43.9
Cyclic operation	291	3902	18830	50.0	51.7
Cyclic operation	292	3829	19360	50.0	87.0
Cyclic operation	293	3831	18730	50.0	44.3
Cyclic operation	294	3892	18600	50.0	27.4
Cyclic operation	295	3878	18650	50.0	28.7
Cyclic operation	296	3876	19700	50.0	47.8
Cyclic operation	297	3797	18970	50.0	50.9
Cyclic operation	298	3821	19360	50.0	61.3
Cyclic operation	299	3802	18840	50.0	54.8
Cyclic operation	300	3868	18550	50.0	44.8
Cyclic operation	301	3844	18960	50.0	59.6
Cyclic operation	302	3829	18960	50.0	64.3
Cyclic operation	303	3817	19270	50.0	77.4
Cyclic operation	304	3824	19410	50.0	91.7
Cyclic operation	305	3874	19380	50.0	90.4
Cyclic operation	306	3909	19360	50.0	76.5
Cyclic operation	307	3844	18840	50.0	40.9
Cyclic operation	308	3844	18550	50.0	59.1
Cyclic operation	309	3861	18960	50.0	47.4
Cyclic operation	310	3877	18900	50.0	33.0
Cyclic operation	311	3866	18900	50.0	4.3
Cyclic operation	312	3874	18900	50.0	11.3
Cyclic operation	313	3925	18900	50.0	3.5
Cyclic operation	314	3832	18760	50.0	-3.0
Cyclic operation	315	3836	18740	50.0	-27.0
Cyclic operation	316	3852	18480	50.0	-10.9
Cyclic operation	317	3857	18230	50.0	-16.1
Cyclic operation	318	3890	17820	50.0	-36.1
Cyclic operation	319	3891	17780	50.0	-83.5
Cyclic operation	320	3808	17680	50.0	-56.1
Cyclic operation	321	3808	17900	50.0	-63.5
Cyclic operation	322	3781	17890	50.0	-41.3
Cyclic operation	323	3792	17430	50.0	-48.7
Cyclic operation	324	3844	17860	50.0	-47.8
Cyclic operation	325	3718	17890	50.0	-46.5

Stage	Hours in operation	Primary RO concentrate electrical conductivity	Recirculation liquor electrical conductivity	SNF volumetric recovery	ΔEC / Δdt
Cyclic operation	326	3922	17970	50.0	-56.5
Cyclic operation	327	3844	18720	50.0	-30.0
Cyclic operation	328	3843	18570	50.0	-35.2
Cyclic operation	329	3784	18670	50.0	-30.0
Cyclic operation	330	3869	18920	50.0	3.5
Cyclic operation	331	3868	18980	50.0	18.7
Cyclic operation	332	3918	18610	50.0	-15.2
Cyclic operation	333	3890	19060	50.0	7.0
Cyclic operation	334	3813	18570	50.0	-14.3
Cyclic operation	335	3851	18160	50.0	-32.2
Cyclic operation	336	3863	18630	50.0	-11.7
Cyclic operation	337	3868	18740	50.0	-0.9
Cyclic operation	338	3822	18270	50.0	-20.4
Cyclic operation	339	3880	17780	50.0	-30.4
Cyclic operation	340	3895	18640	50.0	17.8
Cyclic operation	341	3877	18470	50.0	28.3
Cyclic operation	342	3840	18840	50.0	46.1
Cyclic operation	343	3821	18520	50.0	36.5
Cyclic operation	344	3772	18580	50.0	29.6
Cyclic operation	345	3844	18440	50.0	23.9
Cyclic operation	346	3871	18240	50.0	35.2
Cyclic operation	347	3893	18210	50.0	15.2
Cyclic operation	348	3799	18800	50.0	39.6
Cyclic operation	349	3803	18450	50.0	20.9
Cyclic operation	350	3753	18300	50.0	-18.3
Cyclic operation	351	3738	18440	50.0	-5.7
Cyclic operation	352	3800	18330	50.0	-14.8
Cyclic operation	353	3808	18070	50.0	-37.0
Cyclic operation	354	3865	18050	50.0	-40.4
Cyclic operation	355	3935	18070	50.0	-23.5
Cyclic operation	356	3788	18090	50.0	-42.2
Cyclic operation	357	3838	18110	50.0	-20.0

Appendix C1-1: SNF Model (DSPM & DE) parameters – Sensitivity analysis Case 1

		CASE 1-1	CASE 1-2	CASE 1-3	CASE 1-4	CASE BASE	CASE 1-5
		10%	20%	30%	40%	50% SGS	60%
delta xe	µm	0.3	0.3	0.3	0.3	0.3	0.3
r_por	nm	0.57	0.57	0.57	0.57	0.57	0.57
donnan m	mV	-0.03	-0.03	-0.03	-0.03	-0.03	-0.03
donnan p	mV	0.02	0.02	0.02	0.02	0.02	0.02
A val	m/s.bar	5.28E-07	5.28E-07	5.28E-07	5.28E-07	5.28E-07	5.28E-07
B val	$m.h^{-1}$	2.50E-04	2.50E-04	2.50E-04	2.50E-04	2.50E-04	2.50E-04
mdes		39.5	39.5	39.5	39.5	39.5	39.5
rec		0.1	0.2	0.3	0.4	0.5	0.6
m1	kg/h	5100	5100	5100	5100	5100	5100
elements	#	5	5	5	5	5	5
area	m^2	33.1	33.1	33.1	33.1	33.1	33.1
node_area	m^2	16.55	16.55	16.55	16.55	16.55	16.55
feed	kg/h	5099.6	5099.6	5099.6	5099.6	5099.6	5099.6
perm	kg/h	509.2	1015.7	1524.1	2032.3	2541.5	3033.8
conc	kg/h	4590.4	4083.9	3575.5	3067.3	2558.1	2065.8
flux	LMH	3.1	6.2	9.2	12.3	15.4	18.4
Avg node flux	$m.s^{-1}$	8.58E-07	1.71E-06	2.57E-06	3.42E-06	4.28E-06	5.11E-06

Rejections		CASE 1-1	CASE 1-2	CASE 1-3	CASE 1-4	CASE BASE	CASE 1-5
H		24.9%	23.1%	22.0%	21.4%	13.3%	11.7%
Na		24.5%	24.9%	25.0%	25.1%	25.1%	25.1%
K		24.3%	24.8%	25.0%	25.1%	25.1%	25.1%
Ca		73.8%	76.7%	77.7%	78.2%	82.7%	83.1%
Mg		77.0%	86.3%	90.2%	92.1%	94.1%	94.5%
OH		-0.3%	4.5%	6.9%	8.1%	19.0%	20.7%
Cl		0.0%	0.0%	0.0%	0.0%	3.1%	3.5%
HCO_3		0.1%	8.1%	11.8%	13.7%	26.0%	27.8%
SO_4		92.7%	96.1%	97.3%	97.9%	99.4%	99.4%
CO_2		7.0%	10.5%	12.0%	12.7%	15.9%	16.4%
Si		1.1%	3.0%	4.4%	5.4%	6.1%	6.4%

Appendix C1-2: SNF Model (DSPM & DE) parameters – Sensitivity analysis Case 1

jw node		CASE 1-1	CASE 1-2	CASE 1-3	CASE 1-4	CASE BASE	CASE 1-5
0	m^3/m^2s	1.32E-06	2.17E-06	3.03E-06	3.91E-06	4.80E-06	5.67E-06
1	m^3/m^2s	1.21E-06	2.05E-06	2.91E-06	3.78E-06	4.66E-06	5.53E-06
2	m^3/m^2s	1.10E-06	1.94E-06	2.80E-06	3.66E-06	4.54E-06	5.40E-06
3	m^3/m^2s	9.96E-07	1.84E-06	2.69E-06	3.55E-06	4.43E-06	5.28E-06
4	m^3/m^2s	8.96E-07	1.74E-06	2.59E-06	3.45E-06	4.32E-06	5.16E-06
5	m^3/m^2s	7.98E-07	1.65E-06	2.50E-06	3.35E-06	4.21E-06	5.05E-06
6	m^3/m^2s	7.03E-07	1.56E-06	2.41E-06	3.26E-06	4.11E-06	4.93E-06
7	m^3/m^2s	6.11E-07	1.47E-06	2.32E-06	3.17E-06	4.01E-06	4.82E-06
8	m^3/m^2s	5.20E-07	1.38E-06	2.24E-06	3.09E-06	3.91E-06	4.69E-06
9	m^3/m^2s	4.31E-07	1.30E-06	2.16E-06	3.01E-06	3.81E-06	4.56E-06

Element string pressures		CASE 1-1	CASE 1-2	CASE 1-3	CASE 1-4	CASE BASE	CASE 1-5
Pressure in	kPag	379.8	547.2	714.8	883.8	1064.7	1234.5
Pressure out	kPag	217.2	397.4	577.3	757.7	949.3	1128.9
ΔP	kPa	162.6	149.7	137.6	126.1	115.3	105.6

Appendix C2-1: SNF Model (DSPM & DE) parameters – Sensitivity analysis Case 2

		CASE 2-1	CASE 2-2	CASE 2-3	CASE 2-4	CASE 2-5	CASE 2-6
		10%	20%	30%	40%	50%	60%
delta xe	μm	0.3	0.3	0.3	0.3	0.3	0.3
r_por	nm	0.5	0.5	0.5	0.5	0.5	0.5
donnan m	mV	-0.03	-0.03	-0.03	-0.03	-0.03	-0.03
donnan p	mV	0.02	0.02	0.02	0.02	0.02	0.02
A val	m/s.bar	5.28E-07	5.28E-07	5.28E-07	5.28E-07	5.28E-07	5.28E-07
B val	$m.h^{-1}$	2.50E-04	2.50E-04	2.50E-04	2.50E-04	2.50E-04	2.50E-04
mdes		39.5	39.5	39.5	39.5	39.5	39.5
rec		0.1	0.2	0.3	0.4	0.5	0.6
m1	kg/h	5100	5100	5100	5100	5100	5100
elements	#	5	5	5	5	5	5
area	m^2	33.1	33.1	33.1	33.1	33.1	33.1
node_area	m^2	16.55	16.55	16.55	16.55	16.55	16.55
feed	kg/h	5099.6	5099.6	5099.6	5099.6	5099.6	5099.6
perm	kg/h	508.5	1014.0	1522.9	2031.4	2539.7	3047.9
conc	kg/h	4591.1	4085.6	3576.7	3068.2	2559.9	2051.7
flux	LMH	3.1	6.1	9.2	12.3	15.4	18.5
Avg node flux	$m.s^{-1}$	8.56E-07	1.71E-06	2.57E-06	3.42E-06	4.28E-06	5.14E-06

Rejections		CASE 2-1	CASE 2-2	CASE 2-3	CASE 2-4	CASE 2-5	CASE 2-6
H		18.1%	13.7%	-11.2%	-29.9%	-44.5%	-54.9%
Na		25.0%	25.1%	25.1%	25.1%	25.1%	25.1%
K		24.3%	24.8%	25.2%	25.2%	25.1%	25.1%
Ca		73.8%	78.4%	87.3%	89.7%	91.0%	91.8%
Mg		93.2%	96.4%	98.1%	98.3%	98.5%	98.5%
OH		9.8%	16.9%	39.2%	48.8%	54.4%	57.8%
Cl		0.0%	1.7%	7.5%	9.8%	11.1%	11.9%
HCO_3		16.4%	24.6%	46.5%	55.3%	60.2%	63.1%
SO_4		93.6%	96.6%	99.5%	99.5%	99.5%	99.4%
CO_2		13.5%	16.1%	20.8%	22.3%	23.1%	23.5%
Si		8.4%	14.3%	18.6%	21.6%	23.4%	24.1%

Appendix C2-2: SNF Model (DSPM & DE) parameters – Sensitivity analysis Case 2

jw node		CASE 2-1	CASE 2-2	CASE 2-3	CASE 2-4	CASE 2-5	CASE 2-6
0	m^3/m^2s	1.32E-06	2.17E-06	3.04E-06	3.92E-06	4.82E-06	5.74E-06
1	m^3/m^2s	1.20E-06	2.05E-06	2.92E-06	3.79E-06	4.68E-06	5.59E-06
2	m^3/m^2s	1.10E-06	1.94E-06	2.80E-06	3.67E-06	4.55E-06	5.45E-06
3	m^3/m^2s	9.95E-07	1.84E-06	2.70E-06	3.56E-06	4.43E-06	5.32E-06
4	m^3/m^2s	8.94E-07	1.74E-06	2.59E-06	3.45E-06	4.32E-06	5.20E-06
5	m^3/m^2s	7.97E-07	1.64E-06	2.50E-06	3.35E-06	4.21E-06	5.07E-06
6	m^3/m^2s	7.02E-07	1.55E-06	2.41E-06	3.25E-06	4.10E-06	4.95E-06
7	m^3/m^2s	6.09E-07	1.47E-06	2.32E-06	3.16E-06	4.00E-06	4.82E-06
8	m^3/m^2s	5.19E-07	1.38E-06	2.23E-06	3.07E-06	3.89E-06	4.68E-06
9	m^3/m^2s	4.30E-07	1.30E-06	2.15E-06	2.99E-06	3.78E-06	4.53E-06

Element string pressures		CASE 2-1	CASE 2-2	CASE 2-3	CASE 2-4	CASE 2-5	CASE 2-6
Pressure in	kPag	387.7	555.6	737.3	912	1088.6	1269
Pressure out	kPag	225.2	405.8	599.8	786	973.4	1163.9
ΔP	kPa	162.6	149.8	137.5	126	115.2	105.1

Appendix C3-1: SNF Model (DSPM & DE) parameters – Sensitivity analysis Case 3

		CASE 3-1	CASE 3-2	CASE 3-3	CASE 3-4	CASE 3-5	CASE 3-6
		10%	20%	30%	40%	50%	60%
delta xe	µm	0.3	0.3	0.3	0.3	0.3	0.3
r_por	nm	0.7	0.7	0.7	0.7	0.7	0.7
donnan m	mV	-0.03	-0.03	-0.03	-0.03	-0.03	-0.03
donnan p	mV	0.02	0.02	0.02	0.02	0.02	0.02
A val	m/s.bar	5.28E-07	5.28E-07	5.28E-07	5.28E-07	5.28E-07	5.28E-07
B val	$m.h^{-1}$	2.50E-04	2.50E-04	2.50E-04	2.50E-04	2.50E-04	2.50E-04
mdes		39.5	39.5	39.5	39.5	39.5	39.5
rec		0.1	0.2	0.3	0.4	0.5	0.6
m1	kg/h	5100	5100	5100	5100	5100	5100
elements	#	5	5	5	5	5	5
area	m^2	33.1	33.1	33.1	33.1	33.1	33.1
node_area	m^2	16.55	16.55	16.55	16.55	16.55	16.55
feed	kg/h	5099.6	5099.6	5099.6	5099.6	5099.6	5099.6
perm	kg/h	508.9	1016.4	1524.6	2032.8	2541.0	3049.6
conc	kg/h	4590.7	4083.2	3575.0	3066.8	2558.6	2050.0
flux	LMH	3.1	6.2	9.2	12.3	15.4	18.5
Avg node flux	$m.s^{-1}$	8.57E-07	1.71E-06	2.57E-06	3.42E-06	4.28E-06	5.14E-06

Rejections		CASE 3-1	CASE 3-2	CASE 3-3	CASE 3-4	CASE 3-5	CASE 3-6
H		23.8%	25.5%	26.5%	27.4%	27.5%	27.5%
Na		23.7%	24.4%	23.7%	24.3%	24.6%	24.8%
K		24.3%	24.8%	25.1%	24.4%	24.3%	24.3%
Ca		73.8%	76.7%	77.6%	79.5%	79.5%	79.1%
Mg		71.6%	76.4%	79.5%	81.1%	81.6%	82.2%
OH		0.6%	0.2%	-0.2%	-0.3%	-0.4%	-0.4%
Cl		0.0%	0.0%	0.0%	0.0%	0.0%	0.0%
HCO_3		0.0%	0.0%	0.0%	0.0%	0.0%	0.2%
SO_4		91.1%	95.1%	96.8%	99.0%	99.2%	99.0%
CO_2		6.2%	6.8%	7.2%	7.5%	7.5%	7.7%
Si		0.0%	0.0%	0.2%	0.5%	0.7%	0.8%

Appendix C3-2: SNF Model (DSPM & DE) parameters – Sensitivity analysis Case 3

jw node		CASE 3-1	CASE 3-2	CASE 3-3	CASE 3-4	CASE 3-5	CASE 3-6
0	m^3/m^2s	1.32E-06	2.17E-06	3.03E-06	3.91E-06	4.79E-06	5.69E-06
1	m^3/m^2s	1.20E-06	2.05E-06	2.91E-06	3.78E-06	4.66E-06	5.55E-06
2	m^3/m^2s	1.10E-06	1.95E-06	2.80E-06	3.66E-06	4.54E-06	5.42E-06
3	m^3/m^2s	9.95E-07	1.84E-06	2.69E-06	3.55E-06	4.42E-06	5.30E-06
4	m^3/m^2s	8.95E-07	1.74E-06	2.59E-06	3.45E-06	4.31E-06	5.18E-06
5	m^3/m^2s	7.98E-07	1.65E-06	2.50E-06	3.35E-06	4.21E-06	5.07E-06
6	m^3/m^2s	7.03E-07	1.56E-06	2.41E-06	3.26E-06	4.11E-06	4.96E-06
7	m^3/m^2s	6.11E-07	1.47E-06	2.32E-06	3.17E-06	4.01E-06	4.85E-06
8	m^3/m^2s	5.20E-07	1.39E-06	2.24E-06	3.09E-06	3.92E-06	4.73E-06
9	m^3/m^2s	4.31E-07	1.30E-06	2.17E-06	3.00E-06	3.82E-06	4.60E-06

Element string pressures		CASE 3-1	CASE 3-2	CASE 3-3	CASE 3-4	CASE 3-5	CASE 3-6
Pressure in	kPag	378.4	542.7	708.5	878.4	1047	1218.3
Pressure out	kPag	215.9	393	571	752.3	931.7	1112.9
ΔP	kPa	162.6	149.7	137.6	126.1	115.4	105.4

Appendix C4-1: SNF Model (DSPM & DE) parameters – Sensitivity analysis Case 4

		CASE 4-1	CASE 4-2	CASE 4-3	CASE 4-4	CASE 4-5	CASE 4-6
		10%	20%	30%	40%	0.5	60%
delta xe	μm	0.2	0.2	0.2	0.2	0.2	0.2
r_por	nm	0.57	0.57	0.57	0.57	0.57	0.57
donnan m	mV	-0.03	-0.03	-0.03	-0.03	-0.03	-0.03
donnan p	mV	0.02	0.02	0.02	0.02	0.02	0.02
A val	m/s.bar	5.28E-07	5.28E-07	5.28E-07	5.28E-07	5.28E-07	5.28E-07
B val	$m.h^{-1}$	2.50E-04	2.50E-04	2.50E-04	2.50E-04	2.50E-04	2.50E-04
mdes		39.5	39.5	39.5	39.5	39.5	39.5
rec		0.1	0.2	0.3	0.4	0.5	0.6
m1	kg/h	5100	5100	5100	5100	5100	5100
elements	#	5	5	5	5	5	5
area	m^2	33.1	33.1	33.1	33.1	33.1	33.1
node_area	m^2	16.55	16.55	16.55	16.55	16.55	16.55
feed	kg/h	5099.6	5099.6	5099.6	5099.6	5099.6	5099.6
perm	kg/h	509.3	1015.9	1523.5	2031.8	2539.9	3048.9
conc	kg/h	4590.3	4083.7	3576.1	3067.8	2559.7	2050.7
flux	LMH	3.1	6.2	9.2	12.3	15.4	18.5
Avg node flux	$m.s^{-1}$	8.58E-07	1.71E-06	2.57E-06	3.42E-06	4.28E-06	5.14E-06

Rejections		CASE 4-1	CASE 4-2	CASE 4-3	CASE 4-4	CASE 4-5	CASE 4-6
H		24.9%	25.1%	23.4%	22.6%	22.2%	20.3%
Na		24.9%	24.7%	24.9%	25.0%	25.0%	25.1%
K		24.3%	24.8%	25.0%	25.0%	25.1%	24.6%
Ca		73.8%	76.7%	77.7%	78.1%	78.4%	80.4%
Mg		76.8%	80.0%	85.9%	88.6%	90.2%	92.6%
OH		-0.2%	1.3%	4.6%	6.2%	7.1%	10.6%
Cl		0.0%	0.0%	0.0%	0.0%	0.0%	1.0%
HCO_3		0.0%	2.4%	8.0%	10.5%	12.0%	16.3%
SO_4		92.8%	95.6%	97.0%	97.6%	98.0%	99.4%
CO_2		6.9%	8.1%	10.4%	11.4%	12.0%	13.4%
Si		0.3%	1.7%	2.7%	3.4%	3.9%	4.1%

Appendix C4-2: SNF Model (DSPM & DE) parameters – Sensitivity analysis Case 4

jw node		CASE 4-1	CASE 4-2	CASE 4-3	CASE 4-4	CASE 4-5	CASE 4-6
0	m^3/m^2s	1.32E-06	2.17E-06	3.03E-06	3.90E-06	4.79E-06	5.69E-06
1	m^3/m^2s	1.21E-06	2.05E-06	2.91E-06	3.78E-06	4.65E-06	5.55E-06
2	m^3/m^2s	1.10E-06	1.94E-06	2.80E-06	3.66E-06	4.53E-06	5.43E-06
3	m^3/m^2s	9.96E-07	1.84E-06	2.69E-06	3.55E-06	4.42E-06	5.30E-06
4	m^3/m^2s	8.96E-07	1.74E-06	2.59E-06	3.45E-06	4.31E-06	5.19E-06
5	m^3/m^2s	7.98E-07	1.65E-06	2.50E-06	3.35E-06	4.21E-06	5.07E-06
6	m^3/m^2s	7.03E-07	1.56E-06	2.41E-06	3.26E-06	4.11E-06	4.96E-06
7	m^3/m^2s	6.10E-07	1.47E-06	2.32E-06	3.17E-06	4.01E-06	4.84E-06
8	m^3/m^2s	5.20E-07	1.38E-06	2.24E-06	3.09E-06	3.92E-06	4.72E-06
9	m^3/m^2s	4.31E-07	1.30E-06	2.16E-06	3.01E-06	3.82E-06	4.59E-06

Element string pressures		CASE 4-1	CASE 4-2	CASE 4-3	CASE 4-4	CASE 4-5	CASE 4-6
Pressure in	kPag	379.8	544.2	712.3	881.4	1052.5	1230.6
Pressure out	kPag	217.2	394.5	574.8	755.3	937	1125.2
ΔP	kPa	162.6	149.7	137.6	126.1	115.4	105.3

Appendix C5-1: SNF Model (DSPM & DE) parameters – Sensitivity analysis Case 5

		CASE 5-1	CASE 5-2	CASE 5-3	CASE 5-4	CASE 5-5	CASE 5-6
		10%	20%	30%	40%	0.5	60%
delta xe	μm	0.4	0.4	0.4	0.4	0.4	0.4
r_por	nm	0.57	0.57	0.57	0.57	0.57	0.57
donnan m	mV	-0.03	-0.03	-0.03	-0.03	-0.03	-0.03
donnan p	mV	0.02	0.02	0.02	0.02	0.02	0.02
A val	m/s.bar	5.28E-07	5.28E-07	5.28E-07	5.28E-07	5.28E-07	5.28E-07
B val	$m.h^{-1}$	2.50E-04	2.50E-04	2.50E-04	2.50E-04	2.50E-04	2.50E-04
mdes		39.5	39.5	39.5	39.5	39.5	39.5
rec		0.1	0.2	0.3	0.4	0.5	0.6
m1	kg/h	5100	5100	5100	5100	5100	5100
elements	#	5	5	5	5	5	5
area	m^2	33.1	33.1	33.1	33.1	33.1	33.1
node_area	m^2	16.55	16.55	16.55	16.55	16.55	16.55
feed	kg/h	5099.6	5099.6	5099.6	5099.6	5099.6	5099.6
perm	kg/h	509.3	1016.0	1524.7	2030.8	2539.9	3046.4
conc	kg/h	4590.3	4083.6	3574.9	3068.8	2559.7	2053.2
flux	LMH	3.1	6.2	9.2	12.3	15.4	18.5
Avg node flux	$m.s^{-1}$	8.58E-07	1.71E-06	2.57E-06	3.42E-06	4.28E-06	5.13E-06

Rejections		CASE 5-1	CASE 5-2	CASE 5-3	CASE 5-4	CASE 5-5	CASE 5-6
H		25.0%	22.0%	20.7%	10.8%	1.1%	-6.2%
Na		24.9%	25.0%	24.8%	25.1%	25.1%	25.1%
K		24.3%	24.8%	25.1%	25.1%	25.1%	25.1%
Ca		73.8%	76.7%	77.9%	83.4%	85.7%	87.1%
Mg		81.1%	89.4%	92.8%	94.6%	95.2%	95.6%
OH		0.1%	6.3%	8.8%	21.7%	30.5%	35.9%
Cl		0.0%	0.0%	0.2%	3.8%	6.0%	7.4%
HCO_3		1.6%	11.0%	14.7%	28.9%	37.8%	43.1%
SO_4		93.6%	96.4%	97.5%	99.5%	99.4%	99.4%
CO_2		7.9%	11.7%	13.1%	16.7%	18.6%	19.7%
Si		1.9%	4.3%	6.0%	7.3%	8.2%	8.5%

Appendix C5-2: SNF Model (DSPM & DE) parameters – Sensitivity analysis Case 5

jw node		CASE 5-1	CASE 5-2	CASE 5-3	CASE 5-4	CASE 5-5	CASE 5-6
0	m^3/m^2s	1.32E-06	2.17E-06	3.04E-06	3.91E-06	4.80E-06	5.71E-06
1	m^3/m^2s	1.21E-06	2.05E-06	2.91E-06	3.78E-06	4.67E-06	5.56E-06
2	m^3/m^2s	1.10E-06	1.95E-06	2.80E-06	3.66E-06	4.54E-06	5.43E-06
3	m^3/m^2s	9.96E-07	1.84E-06	2.70E-06	3.55E-06	4.43E-06	5.31E-06
4	m^3/m^2s	8.96E-07	1.74E-06	2.59E-06	3.45E-06	4.31E-06	5.19E-06
5	m^3/m^2s	7.98E-07	1.65E-06	2.50E-06	3.35E-06	4.21E-06	5.07E-06
6	m^3/m^2s	7.04E-07	1.56E-06	2.41E-06	3.26E-06	4.11E-06	4.95E-06
7	m^3/m^2s	6.11E-07	1.47E-06	2.32E-06	3.17E-06	4.01E-06	4.83E-06
8	m^3/m^2s	5.21E-07	1.38E-06	2.24E-06	3.08E-06	3.91E-06	4.70E-06
9	m^3/m^2s	4.32E-07	1.30E-06	2.16E-06	3.00E-06	3.81E-06	4.56E-06

Element string pressures		CASE 5-1	CASE 5-2	CASE 5-3	CASE 5-4	CASE 5-5	CASE 5-6
Pressure in	kPag	381.1	548.8	716.8	895.3	1072.4	1251.4
Pressure out	kPag	218.6	399.1	579.2	769.2	957	1146.1
ΔP	kPa	162.6	149.7	137.5	126.1	115.3	105.3

Appendix C6-1: SNF Model (DSPM & DE) parameters – Sensitivity analysis Case 6

		CASE 6-1	CASE 6-2	CASE 6-3	CASE 6-4	CASE 6-5	CASE 6-6
		10%	20%	30%	40%	0.5	60%
delta xe	µm	0.3	0.3	0.3	0.3	0.3	0.3
r_por	nm	0.57	0.57	0.57	0.57	0.57	0.57
donnan m	mV	-0.03	-0.03	-0.03	-0.03	-0.03	-0.03
donnan p	mV	0.02	0.02	0.02	0.02	0.02	0.02
A val	m/s.bar	5.28E-07	5.28E-07	5.28E-07	5.28E-07	5.28E-07	5.28E-07
B val	$m.h^{-1}$	2.50E-04	2.50E-04	2.50E-04	2.50E-04	2.50E-04	2.50E-04
mdes		36.5	36.5	36.5	36.5	36.5	36.5
rec		0.1	0.2	0.3	0.4	0.5	0.6
m1	kg/h	5100	5100	5100	5100	5100	5100
elements	#	5	5	5	5	5	5
area	m^2	33.1	33.1	33.1	33.1	33.1	33.1
node_area	m^2	16.55	16.55	16.55	16.55	16.55	16.55
feed	kg/h	5099.6	5099.6	5099.6	5099.6	5099.6	5099.6
perm	kg/h	508.0	1015.8	1522.4	2030.8	2537.8	3047.5
conc	kg/h	4591.6	4083.8	3577.2	3068.8	2561.8	2052.1
flux	LMH	3.1	6.2	9.2	12.3	15.4	18.5
Avg node flux	$m.s^{-1}$	8.56E-07	1.71E-06	2.56E-06	3.42E-06	4.28E-06	5.13E-06

Rejections		CASE 6-1	CASE 6-2	CASE 6-3	CASE 6-4	CASE 6-5	CASE 6-6
H		23.1%	18.7%	-1.1%	-18.0%	-31.4%	-41.4%
Na		25.1%	25.1%	25.1%	25.1%	25.1%	25.1%
K		24.3%	25.2%	25.2%	25.2%	25.1%	25.1%
Ca		73.8%	77.7%	86.3%	88.9%	90.4%	91.3%
Mg		86.8%	93.5%	95.2%	96.1%	96.5%	96.7%
OH		3.3%	11.1%	32.3%	43.1%	49.5%	53.4%
Cl		0.0%	1.0%	6.5%	9.1%	10.5%	11.4%
HCO_3		7.0%	17.3%	39.4%	49.7%	55.5%	59.0%
SO_4		94.0%	96.9%	99.5%	99.5%	99.5%	99.4%
CO_2		10.1%	13.7%	18.8%	20.9%	21.9%	22.5%
Si		1.1%	3.0%	4.4%	5.4%	6.1%	6.4%

Appendix C6-2: SNF Model (DSPM & DE) parameters – Sensitivity analysis Case 6

jw node		CASE 6-1	CASE 6-2	CASE 6-3	CASE 6-4	CASE 6-5	CASE 6-6
0	m^3/m^2s	1.31E-06	2.17E-06	3.04E-06	3.92E-06	4.81E-06	5.73E-06
1	m^3/m^2s	1.20E-06	2.05E-06	2.91E-06	3.79E-06	4.67E-06	5.58E-06
2	m^3/m^2s	1.10E-06	1.95E-06	2.80E-06	3.67E-06	4.55E-06	5.45E-06
3	m^3/m^2s	9.93E-07	1.84E-06	2.69E-06	3.56E-06	4.43E-06	5.32E-06
4	m^3/m^2s	8.94E-07	1.74E-06	2.59E-06	3.45E-06	4.31E-06	5.19E-06
5	m^3/m^2s	7.96E-07	1.65E-06	2.50E-06	3.35E-06	4.21E-06	5.07E-06
6	m^3/m^2s	7.02E-07	1.56E-06	2.41E-06	3.25E-06	4.10E-06	4.95E-06
7	m^3/m^2s	6.09E-07	1.47E-06	2.32E-06	3.16E-06	4.00E-06	4.82E-06
8	m^3/m^2s	5.19E-07	1.38E-06	2.24E-06	3.08E-06	3.89E-06	4.69E-06
9	m^3/m^2s	4.30E-07	1.30E-06	2.16E-06	2.99E-06	3.79E-06	4.54E-06

Element string pressures		CASE 6-1	CASE 6-2	CASE 6-3	CASE 6-4	CASE 6-5	CASE 6-6
Pressure in	kPag	383.5	552.4	732.5	907.4	1083.6	1264.4
Pressure out	kPag	220.9	402.7	594.9	781.3	968.3	1159.2
ΔP	kPa	162.6	149.7	137.6	126.1	115.3	105.1

Appendix C7-1: SNF Model (DSPM & DE) parameters – Sensitivity analysis Case 7

		CASE 7-1	CASE 7-2	CASE 7-3	CASE 7-4	CASE 7-5	CASE 7-6
		10%	20%	30%	40%	0.5	60%
delta xe	μm	0.3	0.3	0.3	0.3	0.3	0.3
r_por	nm	0.57	0.57	0.57	0.57	0.57	0.57
donnan m	mV	-0.03	-0.03	-0.03	-0.03	-0.03	-0.03
donnan p	mV	0.02	0.02	0.02	0.02	0.02	0.02
A val	m/s.bar	5.28E-07	5.28E-07	5.28E-07	5.28E-07	5.28E-07	5.28E-07
B val	$m.h^{-1}$	2.50E-04	2.50E-04	2.50E-04	2.50E-04	2.50E-04	2.50E-04
mdes		42	42	42	42	42	42
rec		0.1	0.2	0.3	0.4	0.5	0.6
m1	kg/h	5100	5100	5100	5100	5100	5100
elements	#	5	5	5	5	5	5
area	m^2	33.1	33.1	33.1	33.1	33.1	33.1
node_area	m^2	16.55	16.55	16.55	16.55	16.55	16.55
feed	kg/h	5099.6	5099.6	5099.6	5099.6	5099.6	5099.6
perm	kg/h	509.3	1016.2	1526.3	2034.1	2543.3	3052.8
conc	kg/h	4590.3	4083.4	3573.3	3065.4	2556.3	2046.8
flux	LMH	3.1	6.2	9.3	12.3	15.4	18.5
Avg node flux	$m.s^{-1}$	8.58E-07	1.71E-06	2.57E-06	3.43E-06	4.28E-06	5.14E-06

Rejections		CASE 7-1	CASE 7-2	CASE 7-3	CASE 7-4	CASE 7-5	CASE 7-6
H		24.6%	25.2%	24.1%	23.8%	23.0%	22.1%
Na		24.9%	24.5%	24.0%	24.6%	24.8%	24.9%
K		24.3%	24.8%	24.5%	24.2%	24.2%	24.3%
Ca		73.8%	76.7%	77.7%	79.5%	78.9%	78.4%
Mg		75.4%	78.1%	86.8%	89.8%	91.5%	92.1%
OH		-0.1%	0.9%	3.9%	5.6%	6.4%	7.4%
Cl		0.0%	0.0%	0.0%	0.0%	0.0%	0.2%
HCO_3		0.0%	1.6%	7.4%	10.0%	11.5%	12.8%
SO_4		92.4%	95.3%	97.2%	99.2%	98.8%	98.3%
CO_2		6.7%	7.6%	10.4%	11.6%	12.2%	12.6%
Si		1.1%	3.0%	4.4%	5.5%	6.1%	6.4%

Appendix C7-2: SNF Model (DSPM & DE) parameters – Sensitivity analysis Case 7

jw node		CASE 7-1	CASE 7-2	CASE 7-3	CASE 7-4	CASE 7-5	CASE 7-6
0	m^3/m^2s	1.32E-06	2.17E-06	3.04E-06	3.91E-06	4.80E-06	5.70E-06
1	m^3/m^2s	1.21E-06	2.05E-06	2.91E-06	3.79E-06	4.66E-06	5.56E-06
2	m^3/m^2s	1.10E-06	1.94E-06	2.80E-06	3.67E-06	4.54E-06	5.43E-06
3	m^3/m^2s	9.96E-07	1.84E-06	2.70E-06	3.56E-06	4.43E-06	5.31E-06
4	m^3/m^2s	8.96E-07	1.74E-06	2.60E-06	3.45E-06	4.32E-06	5.19E-06
5	m^3/m^2s	7.98E-07	1.65E-06	2.50E-06	3.36E-06	4.21E-06	5.08E-06
6	m^3/m^2s	7.03E-07	1.56E-06	2.41E-06	3.26E-06	4.11E-06	4.97E-06
7	m^3/m^2s	6.11E-07	1.47E-06	2.33E-06	3.17E-06	4.02E-06	4.85E-06
8	m^3/m^2s	5.20E-07	1.39E-06	2.25E-06	3.09E-06	3.92E-06	4.73E-06
9	m^3/m^2s	4.31E-07	1.31E-06	2.17E-06	3.00E-06	3.82E-06	4.60E-06

Element string pressures		CASE 7-1	CASE 7-2	CASE 7-3	CASE 7-4	CASE 7-5	CASE 7-6
Pressure in	kPag	379.6	543.6	713.3	884.7	1054.5	1228.6
Pressure out	kPag	217	393.9	575.8	758.6	939.1	1123.3
ΔP	kPa	162.6	149.7	137.5	126	115.3	105.3

Appendix C8-1: SNF Model (DSPM & DE) parameters – Sensitivity analysis Case 8

		CASE 8-1	CASE 8-2	CASE 8-3	CASE 8-4	CASE 8-5	CASE 8-6
		10%	20%	30%	40%	0.5	60%
delta xe	µm	0.3	0.3	0.3	0.3	0.3	0.3
r_por	nm	0.57	0.57	0.57	0.57	0.57	0.57
donnan m	mV	-0.02	-0.02	-0.02	-0.02	-0.02	-0.02
donnan p	mV	0.01	0.01	0.01	0.01	0.01	0.01
A val	m/s.bar	5.28E-07	5.28E-07	5.28E-07	5.28E-07	5.28E-07	5.28E-07
B val	$m.h^{-1}$	2.50E-04	2.50E-04	2.50E-04	2.50E-04	2.50E-04	2.50E-04
mdes		39.5	39.5	39.5	39.5	39.5	39.5
rec		0.1	0.2	0.3	0.4	0.5	0.6
m1	kg/h	5100	5100	5100	5100	5100	5100
elements	#	5	5	5	5	5	5
area	m^2	33.1	33.1	33.1	33.1	33.1	33.1
node_area	m^2	16.55	16.55	16.55	16.55	16.55	16.55
feed	kg/h	5099.6	5099.6	5099.6	5099.6	5099.6	5099.6
perm	kg/h	508.4	1014.0	1522.2	2030.3	2538.8	3046.2
conc	kg/h	4591.2	4085.6	3577.4	3069.3	2560.8	2053.4
flux	LMH	3.1	6.1	9.2	12.3	15.4	18.5
Avg node flux	$m.s^{-1}$	8.56E-07	1.71E-06	2.56E-06	3.42E-06	4.28E-06	5.13E-06

Rejections		CASE 8-1	CASE 8-2	CASE 8-3	CASE 8-4	CASE 8-5	CASE 8-6
H		17.8%	7.4%	-11.8%	-28.2%	-41.1%	-50.4%
Na		20.4%	21.9%	25.1%	25.1%	25.1%	25.1%
K		22.6%	22.4%	25.2%	25.2%	25.1%	25.1%
Ca		73.8%	83.8%	88.0%	90.0%	91.1%	91.8%
Mg		73.8%	87.5%	96.1%	96.5%	97.0%	97.2%
OH		7.9%	23.8%	39.5%	48.0%	53.2%	56.4%
Cl		0.0%	4.1%	8.1%	10.1%	11.2%	11.9%
HCO_3		10.6%	30.1%	46.4%	54.2%	58.9%	61.6%
SO_4		88.9%	97.0%	99.5%	99.4%	99.4%	99.4%
CO_2		9.7%	16.1%	20.2%	21.7%	22.4%	22.9%
Si		1.1%	3.0%	4.4%	5.4%	6.1%	6.4%

Appendix C8-2: SNF Model (DSPM & DE) parameters – Sensitivity analysis Case 8

jw node		CASE 8-1	CASE 8-2	CASE 8-3	CASE 8-4	CASE 8-5	CASE 8-6
0	m^3/m^2s	1.31E-06	2.16E-06	3.04E-06	3.92E-06	4.81E-06	5.73E-06
1	m^3/m^2s	1.20E-06	2.05E-06	2.92E-06	3.79E-06	4.68E-06	5.59E-06
2	m^3/m^2s	1.10E-06	1.94E-06	2.80E-06	3.67E-06	4.55E-06	5.45E-06
3	m^3/m^2s	9.93E-07	1.84E-06	2.69E-06	3.56E-06	4.43E-06	5.32E-06
4	m^3/m^2s	8.94E-07	1.74E-06	2.59E-06	3.45E-06	4.32E-06	5.19E-06
5	m^3/m^2s	7.97E-07	1.64E-06	2.50E-06	3.35E-06	4.21E-06	5.07E-06
6	m^3/m^2s	7.03E-07	1.55E-06	2.40E-06	3.25E-06	4.10E-06	4.95E-06
7	m^3/m^2s	6.12E-07	1.47E-06	2.32E-06	3.16E-06	4.00E-06	4.82E-06
8	m^3/m^2s	5.22E-07	1.38E-06	2.23E-06	3.07E-06	3.89E-06	4.68E-06
9	m^3/m^2s	4.34E-07	1.30E-06	2.15E-06	2.99E-06	3.79E-06	4.53E-06

Element string pressures		CASE 8-1	CASE 8-2	CASE 8-3	CASE 8-4	CASE 8-5	CASE 8-6
Pressure in	kPag	381.1	557.9	736	909.5	1085.9	1265.9
Pressure out	kPag	218.5	408.1	598.5	783.4	970.6	1160.7
ΔP	kPa	162.6	149.8	137.6	126.1	115.3	105.1

Appendix C9-1: SNF Model (DSPM & DE) parameters – Sensitivity analysis Case 9

		CASE 9-1	CASE 9-2	CASE 9-3	CASE 9-4	CASE 9-5	CASE 9-6
		10%	20%	30%	40%	0.5	60%
delta xe	μm	0.3	0.3	0.3	0.3	0.3	0.3
r_por	nm	0.57	0.57	0.57	0.57	0.57	0.57
donnan m	mV	-0.01	-0.01	-0.01	-0.01	-0.01	-0.01
donnan p	mV	0	0	0	0	0	0
A val	m/s.bar	5.28E-07	5.28E-07	5.28E-07	5.28E-07	5.28E-07	5.28E-07
B val	$m.h^{-1}$	2.50E-04	2.50E-04	2.50E-04	2.50E-04	2.50E-04	2.50E-04
mdes		39.5	39.5	39.5	39.5	39.5	39.5
rec		0.1	0.2	0.3	0.4	0.5	0.6
m1	kg/h	5100	5100	5100	5100	5100	5100
elements	#	5	5	5	5	5	5
area	m^2	33.1	33.1	33.1	33.1	33.1	33.1
node_area	m^2	16.55	16.55	16.55	16.55	16.55	16.55
feed	kg/h	5099.6	5099.6	5099.6	5099.6	5099.6	5099.6
perm	kg/h	510.9	1018.3	1526.4	2035.5	2538.0	3046.1
conc	kg/h	4588.7	4081.3	3573.2	3064.1	2561.6	2053.5
flux	LMH	3.1	6.2	9.3	12.3	15.4	18.5
Avg node flux	$m.s^{-1}$	8.61E-07	1.72E-06	2.57E-06	3.43E-06	4.28E-06	5.13E-06

Rejections		CASE 9-1	CASE 9-2	CASE 9-3	CASE 9-4	CASE 9-5	CASE 9-6
H		-65.1%	-87.3%	-116.4%	-139.2%	-155.6%	-166.7%
Na		15.3%	24.1%	24.4%	24.5%	24.6%	24.7%
K		15.7%	24.1%	24.4%	24.5%	25.1%	24.7%
Ca		63.0%	90.4%	92.3%	93.6%	94.3%	94.8%
Mg		64.3%	94.2%	95.5%	96.3%	96.8%	97.2%
OH		51.2%	64.2%	69.6%	72.8%	74.8%	75.9%
Cl		11.3%	13.7%	14.8%	15.4%	15.8%	16.0%
HCO_3		57.6%	68.3%	72.8%	75.5%	77.0%	78.0%
SO_4		63.3%	95.4%	96.4%	97.1%	97.5%	97.8%
CO_2		21.0%	23.7%	24.3%	24.7%	24.9%	25.0%
Si		1.1%	3.0%	4.4%	5.4%	6.1%	6.3%

Appendix C9-2: SNF Model (DSPM & DE) parameters – Sensitivity analysis Case 9

jw node		CASE 9-1	CASE 9-2	CASE 9-3	CASE 9-4	CASE 9-5	CASE 9-6
0	m^3/m^2s	1.30E-06	2.18E-06	3.05E-06	3.94E-06	4.83E-06	5.75E-06
1	m^3/m^2s	1.19E-06	2.06E-06	2.93E-06	3.81E-06	4.69E-06	5.60E-06
2	m^3/m^2s	1.09E-06	1.95E-06	2.81E-06	3.68E-06	4.56E-06	5.46E-06
3	m^3/m^2s	9.92E-07	1.85E-06	2.70E-06	3.57E-06	4.44E-06	5.33E-06
4	m^3/m^2s	8.97E-07	1.75E-06	2.60E-06	3.46E-06	4.32E-06	5.20E-06
5	m^3/m^2s	8.04E-07	1.65E-06	2.50E-06	3.36E-06	4.21E-06	5.07E-06
6	m^3/m^2s	7.14E-07	1.56E-06	2.41E-06	3.26E-06	4.10E-06	4.94E-06
7	m^3/m^2s	6.26E-07	1.47E-06	2.32E-06	3.16E-06	3.99E-06	4.80E-06
8	m^3/m^2s	5.40E-07	1.39E-06	2.24E-06	3.07E-06	3.88E-06	4.66E-06
9	m^3/m^2s	4.55E-07	1.31E-06	2.16E-06	2.99E-06	3.77E-06	4.50E-06

Element string pressures		CASE 9-1	CASE 9-2	CASE 9-3	CASE 9-4	CASE 9-5	CASE 9-6
Pressure in	kPag	384.6	576.4	746.4	919.9	1094.5	1275.6
Pressure out	kPag	221.9	426.7	609	794	979.3	1170.6
ΔP	kPa	162.7	149.6	137.4	125.9	115.2	105

Appendix D: ICARD 2018 conference proceedings - Estimation of NF Solute Rejection in RO concentrate treatment processes

Estimation of nanofiltration solute rejection in reverse osmosis concentrate treatment processes

Sebastian Franzsen[1], Ricky Bonner[1], Jivesh Naidu[1]
Craig Sheridan[2], Geoffrey S. Simate[2]

[1]*Miwatek, P/Bag X29, Gallo Manor, 2052, Johannesburg, South Africa, sebastianf@miwatek.co.za*
[2]*School of Chemical and Mechanical Engineering, University of Witwatersrand, Johannesburg, P/Bag 3,*

Abstract

A nanofiltration (NF) model was built in the programming language Python and interfaced with geochemical calculation software PHREEQC COM v3 for the prediction of NF rejection performance in the treatment of reverse osmosis (RO) concentrate. The built NF model is considered to have three industrial applications – (1) tracking in service element degradation in terms of increasing pore radius, decreasing effective active layer thickness and decreasing feed-membrane $\Delta\varphi_{D,m}$, (2) element selection in the design of RO concentrate treatment processes and (3) estimation of unknown solute permeability values by considering the likely ion-pairs and dominant ions that characterises a given aqueous solution.

Keywords: Mine water treatment, brine treatment, nanofiltration modelling

Introduction

Research studies have shown that intermediate chemical demineralisation (CD) of primary reverse osmosis (RO) concentrate followed by secondary RO desalination can substantially improve the volumetric recovery of brackish feed waters (Gabelich et al. 2007, Rahardianto et al. 2007, McCool et al. 2013, Rahardianto et al. 2010, Greenlee et al. 2011).

Different NF elements show substantial performance variation for systems with only slight variation (Artuğ 2007). Phenomenological models and the typical application of single salt (e.g. NaCl, Na_2SO_4, $CaSO_4$, $MgSO_4$ etc.) rejection data are considered inappropriate for NF modelling or NF element selection due to the complexity of the solute transport mechanism.

The DSPM&DE model considers the membrane as having effective pore radius, effective active layer thickness, effective membrane charge density and membrane dielectric constant and is capable of describing the asymptotic concentration gradient at the membrane-solution interfaces (Artuğ 2007, Geraldes and Brites Alves 2008).

The Pitzer aqueous speciation model (pitzer.dat) supplied with PHREEQC can accurately predict thermodynamic properties at high ionic strength for solutions with compositions substantially different from that of seawater (Appelo 2015, Harvie et al. 1984, Pitzer 1981).

The intent of this paper is to present an alternative DSPM & DE model in which (1) the Pitzer activity and osmotic coefficients are determined by incorporating the PHREEQC COM module in the solution algorithm, (2) the aqueous solution is expressed as cation-anion ion pairs with a selected dominant ion for transport and partitioning modelling, and (3) the inclusion of the uncharged specie SiO2 provides regression in the absence of electrostatic effects. The model was fitted to data from a pilot scale high recovery RO-CD-NF with recycle to CD process (RO-CD-NF-RCY) and a full-scale RO-NF-CD process. The former process was piloted and the later currently in operation at the Newmont Ahafo mine water treatment plant in Ghana.

Methods

The model domain comprises ten nodes *j* along the element string feed channel and three distinct regions of solute mass transport at each node presented in Figure 1. The solute transport path and mechanisms through

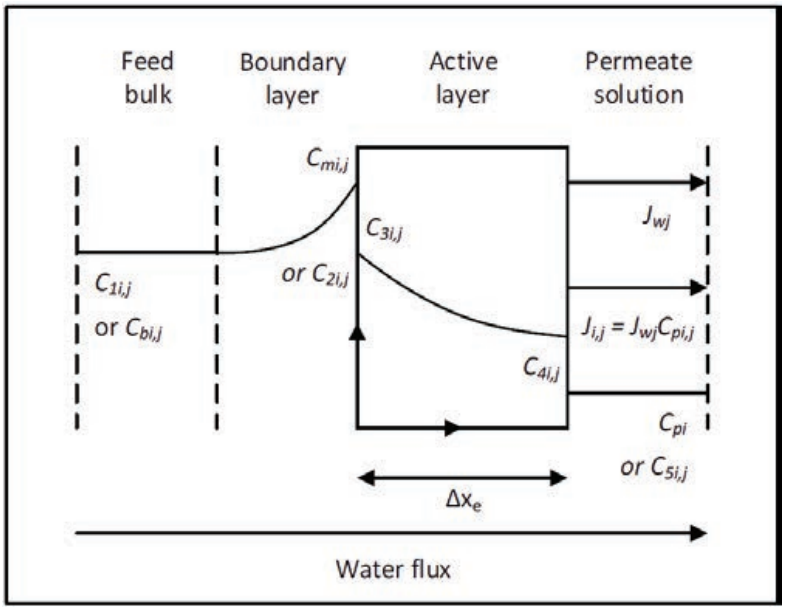

Figure 1 *Schematic diagram of the solute concentration profile for each node j*

the membrane includes (1) development of a concentration polarisation boundary layer approaching the feed-membrane interface, (2) feed-membrane interface partitioning occurs through steric, Donnan potential and dielectric exclusion, (3) active layer transport and (4) membrane-permeate interface partitioning occurs through steric, Donnan potential and dielectric exclusion.

The aqueous system included H-Na-K-Ca-Mg-OH-HCO_3-Cl-SO_4-SiO_2-CO_2 and was arranged into Na_2SO_4, NaCl, $NaHCO_3$, NaOH, K_2SO_4, KCl, $KHCO_3$, KOH, $CaCl_2$, $CaSO_4$, $Ca(HCO_3)_2$, $Ca(OH)_2$, $MgCl_2$, $MgSO_4$, $Mg(HCO_3)_2$, $Mg(OH)_2$, HCl, H_2SO_4, CO_2 and SiO_2 ion pairs and molecules.

Equation 1 is the combination of the Mariñas and Urama mass transfer correlation and a correction factor ∈ for the suction effect generated by permeation through the membrane (Geraldes and Brites Alves 2008, Crittenden et al. 2012). ∈ is described by semi empirical correlation shown in Equation 2 (Geraldes and Brites Alves 2008).

$$k_{cpi,j} = k_{i,j}\epsilon_{i,j} = \kappa\frac{D_L}{d_H}\left(Re_j\right)^{0.5}\left(Sc_{i,j}\right)^{0.33}.\epsilon_{i,j} \qquad \text{Equation 1}$$

$$\epsilon = \emptyset_i + \left(1 + 0.26\emptyset_i^{1.4}\right)^{-1.7} \text{ where } \emptyset_i = \frac{J_{w,j}}{k_{c,i}} \qquad \text{Equation 2}$$

The partitioning at the feed-membrane and membrane-permeate interface is described in Equation 3 as a function of three transport resistances – (1) Steric partitioning, (2) Donnan potential effect and (3) dielectric exclusion (Artuğ 2007). Steric partitioning θi expressed in Equation 4, refers to the transport hindrance as a function of solute radii and pore-radii within well-defined cylindrical pores (Labban et al. 2017). The effect of the Donnan potential promotes the transport of counter-ions and hinders the transport of co-ions (Peeters et al. 1998). Dielectric exclusion refers to the reduction in solvation capacity of the pore fluid due to the hydraulics in the confined space of the pores. This barrier to ionic species entering the active layer is referred to as the Born solvation energy barrier ΔW_i and is shown in Equation 5 (Bowen and Welfoot 2002).

$$\frac{\gamma_{3i}c_{3i}}{\gamma_{2i}c_{2i}} = \theta_i.\exp\left(-\frac{z_iF}{R_gT}.\Delta\varphi_D\right).\exp\left(-\frac{\Delta W_{i,Born}}{k_B.T}\right) \qquad \text{Equation 3}$$

$$\theta_i = \left(1 - \frac{r_{si}}{r_p}\right)^2 = (1 - \lambda_i)^2 \qquad \text{Equation 4}$$

$$\Delta W_{i,Born} = \frac{z_i^2.e^2}{8\pi\varepsilon_0 r_{si}}.\left(\frac{1}{\varepsilon_p} - \frac{1}{\varepsilon_b}\right) \qquad \text{Equation 5}$$

Equation 6 represents the solute flux through the membrane using the ENP equation which includes terms for diffusion, electromigration and convection transport (Artuğ 2007, Peeters et al. 1998). Hindrance factors K_{id} and K_{ic} must be applied to the diffusion and convection terms respectively for transport in the active layer (Artuğ 2007).

$$J_{i,j}^{ENP} = -K_{id}D_i\frac{dc_i}{dx} - \frac{z_ic_{i,j}D_{pi}}{R_gT}F\frac{d\varphi}{dx} + K_{ic}c_{i,j}V \qquad \text{Equation 6}$$



In this study the active layer transport is reduced to the linear transport between the two inside membrane interfacial concentrations c3 and c4 – refer to Figure 1. To evaluate the dφ/dx term, the cation-anion ion pairs were speciated out to individual ions using PHREEQC. Initial estimates of the concentration polarisation layer and permeate concentrations, c2 and c5 respectively, are determined through Equations 7 to 11.

Solution algorithm for NF model

Step 1 is to separate the feed solution into cation-anion ion pairs, specify the element properties, model parameters, process inputs and regression parameters. The parameters specific to each of the ion pairs and the individual ions are calculated – stokes radius, stokes radius to membrane pore radius, convection hindrance factor, diffusion hindrance factor and Born solvation energy barrier. Table 1 lists the input parameters for the calibration cases of the RO-NF-CD and RO-CD-NF-RCY processes.

Step 2 is to estimate the hydraulic parameters, water flux, solute flux and outside membrane concentrations (c_1, c_2 and c_5) to enable the evaluation of the ENP and partitioning equations (Equations 3 and 6 respectively). Equation 7 is the solute flux as each stage j expressed in terms of a phenomenological constant that is generalised for each of the cation-anion ion pairs. Equation 8 is the membrane water flux equation with the membrane specific water permeability constant A.

$$J_{i,j} = B_i\left(\beta_{i,j}c_{bi,j} - c_{pi,j}\right) \quad \text{Equation 7}$$

$$J_{w,j} = A\left[\left(P_{b,j} - P_p\right) - \left(\pi_{m,j} - \pi_{p,j}\right)\right] \quad \text{Equation 8}$$

The concentration polarisation at each node, expressed in terms of water flux, mass transfer coefficient and rejection and generalised for each specie, is shown in Equation 9 (Crittenden et al. 2012). Equation 10 is the definition of the solute flux generalised for each specie and the permeate concentration substituted with the equivalent in terms of solute rejection and feed bulk concentration (Crittenden et al. 2012).

$$\beta_{i,j} = e^{J_{w,j}/k_{cpi,j}}.r_{i,j} + \left(1 - r_{i,j}\right) \quad \text{Equation 9}$$

$$J_{i,j} = J_{w,j}c_{pi,j} = J_{w,j}(1 - r_i)c_{bi,j} \quad \text{Equation 10}$$

Setting Equation 10 equal to Equation 7 and substituting Equation 9 leads to an equation that relates the solute rejection, solute permeability constant, concentration polarisation mass transfer coefficient and the water flux – Equation 11:

$$r_{i,j} = \left[B_i e^{J_w/k_{cpi,j}} + J_{w,j}\right]^{-1}.J_{w,j} \quad \text{Equation 11}$$

The solver iterates through the nodes several times and utilises the Newton method from the *Scipy.Optimize* package to solve for the water flux at each node that satisfies the solute rejections from Equation 11 at the

Table 1. *Model input parameters for calibration case*

Model input parameters	Unit	RO-NF-CD	RO-CD-NF-RCY
Element		MDS NF 8040	MDS NF 4040T
Design volumetric recovery	%	50	50
Membrane surface area	m^2	33.1	7.3
Feed pressure	kPag	1065	1750
Operating temperature	°C	30	30
Feed flow rate	m^3/h	5.1	1.9
Elements per string		5	8
Nodes per element string		10	10
Feed spacer thickness	Mil	31	31

specified feed pressure. This iterative strategy, as opposed to a simultaneous solution algorithm, was used to incorporate the PHREEQC COM module.

Step 3 is to evaluate the c3 and c4 using Equation 3. The $d\varphi/dx$ term must be determined to calculate the solute flux according to the ENP Equation 6. The ratio of the solute flux determined by the ENP Equation 9 and the solute permeability constant in Equation 7 are used to adjust the solute permeability constant of each cation-anion ion pair. The solute permeability constant for the next solver iteration is determined by using Equation 12

Step 4 checks the convergence criteria and returns the solver to step 2 until convergence is achieved. The final cation-anion ion pairs are speciated out in PHREEQC and the overall rejection of individual ions reported.

Results and Discussion

The results of the regression of key parameters to operational data are shown in Table 2 and the comparison of rejection performance between the model and the analytical results are shown in Table 3. The regression of the pore radius and effective active layer thickness was constrained to yield close agreement with rejection of uncharged species SiO_2. This technique is useful as the rejection of SiO_2 is not subject to the electrostatic effects at the system pH.

The dominant ions were assigned for a negative feed-membrane Donnan potential, since (1) ion pairs with divalent anion has the anion as dominant as the repulsion from the feed-membrane interface appeared dominant, (2) ion pairs with monovalent anion and cation has the cation as dominant as the attraction to the feed-membrane interface appeared dominant, (3) pairs with divalent cation and monovalent anion had the divalent cation as dominant as the attraction to the feed-membrane interface appeared dominant and (4) pairs with divalent cation and divalent anion had the divalent anion as dominant as the repulsion from the feed-membrane interface appeared dominant.

$$B_{i,j} = J_{i,j}^{ENP}.\left[\beta_{i,j}c_{bi,j} - c_{pi,j}\right]^{-1} \text{ and } B_i = \overline{B}_{i,j} \qquad \text{Equation 12}$$

The effect of membrane pore dielectric constant ε_{pore} and feed-membrane Donnan potentials $\Delta\varphi_{D,m}$ on rejection performance of the MDS NF 8040 elements in the RO-NF-CD process are shown in Figures 2 and 3. Reducing ε_pore increases the Born solvation energy barrier ΔW_i at the feed-membrane interface and hence the rejection performance of all charged species is improved.

The uncharged specie SiO_2 is not affected by changes in $\Delta\varphi_{D,M}$ or ε_{pore}. Increasing the negative $\Delta\varphi_{D,M}$ increases the repulsion of co-ions and the attraction of counter-ions. For higher negative $\Delta\varphi_{D,M}$, SO_4 rejection increases due to co-ion repulsion, Ca and Mg rejection decreases due to counter-ion attraction, HCO_3 and Cl rejection decreases due to counter-ion attraction (dominant ions are cations for monovalent anions).

Table 2. *Regression results for RO-NF-CD full scale and RO-CD-NF-RCY pilot processes*

Calibration case regression results		Unit	RO-NF-CD FULL SCALE	RO-CD-NF w/ recycle PILOT
Element	r_{pore}		MDS NF 8040	MDS NF 4040T
Pore radius	Δx_e	nm	0.57	0.535
Active layer thickness	ε_{pore}	µm	0.3	0.3
Membrane dielectric constant	A		39.5	39.5
Water permeability constant	$\Delta\phi_{D,m}$	$ms^{-1}bar\text{-}1$	5.28E-07	7.5E-07
Feed-membrane potential	$\Delta\phi_{D,p}$	mV	- 30	- 4.5
Membrane-permeate potential		mV	+ 20	+ 0.5
Permeate pH [model / (analytical)]			7.6 / (7.7)	5.7 / (5.7)
Feed pH [model / (analytical)]			7.7 / (7.9)	5.9 / (5.9)



Table 3. Comparison of ion rejections determined by the model and the analytical results from SGS

Date	Data	Na rej %	K rej %	SO_4 rej %	Ca rej %	Mg rej %	HCO_3 rej %	Cl rej %	SiO_2 rej %
RO-NF-CD	Model	25.1	25.1	99.4	82.7	94.1	26.0	3.1	6.1
FULL SCALE	SGS	21.0	23.5	99.6	86.7	94.4		0.3	5.9
RO-CD-NF-RCY	Model	96.4	96.4	99.2	99.2	99.3	20.5	0.0	11.7
PILOT	SGS	96.4	96.8	99.1	99.6	99.1		< 0	13.5

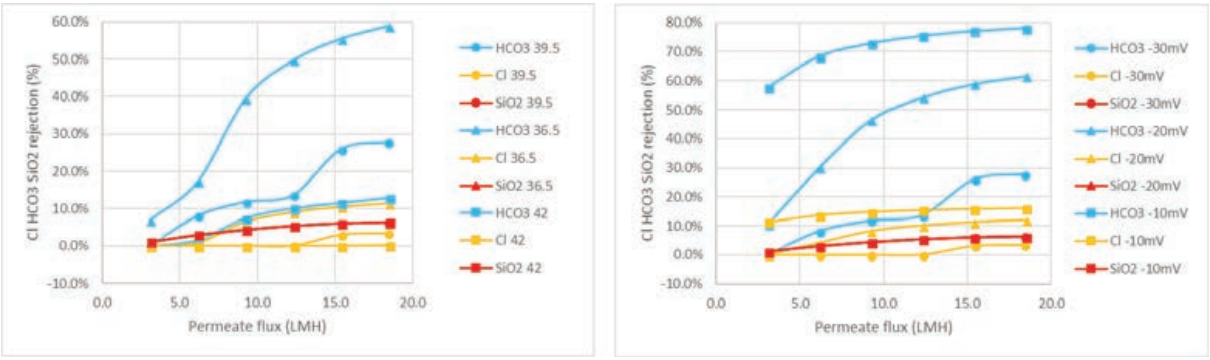

Figure 2 The effect of membrane pore dielectric constant and feed-membrane Donnan potentials on the HCO3, Cl and SiO2 rejection performance of the MDS NF 8040 elements in the RO-NF-CD process

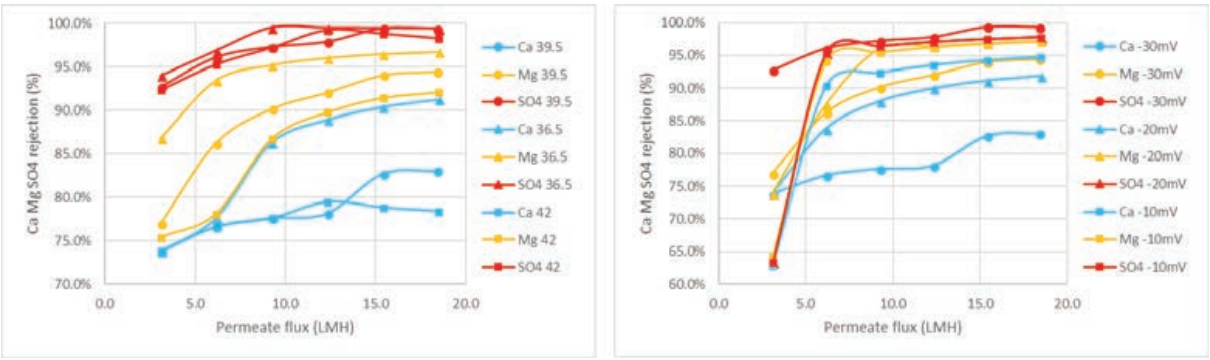

Figure 3 The effect of membrane pore dielectric constant and feed-membrane Donnan potentials on the Ca, Mg and SO4 rejection performance of the MDS NF 8040 elements in the RO-NF-CD process

Conclusions

The fundamental differences between this work and other ENP and DSPM & DE studies are (1) the arrangement of the ions into cation-anion ion pairs with a representative dominant ion, (2) the assignment of $\Delta\varphi_{D,m}$ and $\Delta\varphi_{D,p}$ as input values, and (3) the omission of the charge offset $-C_X$. The built NF model can match the rejection performance of the MDS elements in the RO-NF-CD and RO-CD-NF-RCY processes with resulting $\Delta\varphi_{D,m}$ and $\Delta\varphi_{D,p}$ values and membrane pore dielectric constant (39.5 for both NF elements) that are within the expected ranges for Polyamide membrane active layers. It is recommended that the NF model is fitted to additional operational data and the fitted parameters, $\Delta\varphi_{D,m}$, $\Delta\varphi_{D,p}$ and ε_{pore}, compared to fitted parameters of a conventional ENP and DSPM & DE model to better understand the limitations and advantages of the ion pairing with dominant ion feature of the built NF model.

The built NF model is considered to have three industrial applications – (1) tracking in service element degradation in terms of increasing pore radius, decreasing effective active layer thickness and decreasing feed-membrane $\Delta\varphi_{D,m}$, (2) element selection in the design of RO-NF-CD and RO-NF-CD-RCY processes and (3) estimation of unknown solute B values by considering the likely ion-

pairs and dominant ions that it may form for a given solution type. The interface with the PHREEQC COM module for the calculation of Pitzer activity and osmotic coefficients is considered an advantage for fitting of high ionic strength applications.

Acknowledgements

The authors gratefully acknowledge Miwatek for their financial support and project opportunity through which this work was made possible. Further, the authors gratefully acknowledge the Water Research Commission of South Africa for their financial and scientific support for the continuation of this work into a public demonstration scale project (contract no. K5/2483//3).

References

Gabelich, C.J., Williams, M.D., Rahardianto, A., Franklin, J.C. and Cohen, Y. (2007) High-recovery reverse osmosis desalination using intermediate chemical demineralization. Journal of Membrane Science 301(1–2), 131-141.

Rahardianto, A., Gao, J., Gabelich, C.J., Williams, M.D. and Cohen, Y. (2007) High recovery membrane desalting of low-salinity brackish water: Integration of accelerated precipitation softening with membrane RO. Journal of Membrane Science 289(1–2), 123-137.

McCool, B.C., Rahardianto, A., Faria, J.I. and Cohen, Y. (2013) Evaluation of chemically-enhanced seeded precipitation of RO concentrate for high recovery desalting of high salinity brackish water. Desalination 317, 116-126.

Rahardianto, A., McCool, B.C. and Cohen, Y. (2010) Accelerated desupersaturation of reverse osmosis concentrate by chemically-enhanced seeded precipitation. Desalination 264(3), 256-267.

Greenlee, L.F., Testa, F., Lawler, D.F., Freeman, B.D. and Moulin, P. (2011) Effect of antiscalant degradation on salt precipitation and solid/liquid separation of RO concentrate. Journal of Membrane Science 366(1-2), 48-61.

Artuğ, G. (2007) Modelling and Simulation of Nanofiltration Membranes, Cuvillier.

Geraldes, V. and Brites Alves, A.M. (2008) Computer program for simulation of mass transport in nanofiltration membranes. Journal of Membrane Science 321(2), 172-182.

Appelo, C.A.J. (2015) Principles, caveats and improvements in databases for calculating hydrogeochemical reactions in saline waters from 0 to 200°C and 1 to 1000atm. Applied Geochemistry 55, 62-71.

Harvie, C.E., Møller, N. and Weare, J.H. (1984) The prediction of mineral solubilities in natural waters: The Na-K-Mg-Ca-H-Cl-SO4-OH-HCO3-CO3-CO2-H2O system to high ionic strengths at 25°C. Geochimica et Cosmochimica Acta 48(4), 723-751.

Pitzer, K.S. (1981) Characteristics of very concentrated aqueous solutions. Physics and Chemistry of the Earth 13–14, 249-272.

Crittenden, J.C., Harza, M.W., Trussell, R.R. and Hand, D.W. (2012) MWH's Water Treatment: Principles and Design, Wiley.

Labban, O., Liu, C., Chong, T.H. and Lienhard, J.H. (2017) Fundamentals of low-pressure nanofiltration: Membrane characterization, modeling, and understanding the multi-ionic interactions in water softening. Journal of Membrane Science 521, 18-32.

Peeters, J.M.M., Boom, J.P., Mulder, M.H.V. and Strathmann, H. (1998) Retention measurements of nanofiltration membranes with electrolyte solutions. Journal of Membrane Science 145(2), 199-209.

Bowen, W.R. and Welfoot, J.S. (2002) Modelling the performance of membrane nanofiltration—critical assessment and model development. Chemical Engineering Science 57, 1121-1137.

